Sensing and Actuation from Biology to Electronics

Thesis by

Alex Hao-Yu Pai

In Partial Fulfillment of the Requirements

for the Degree of

Doctor of Philosophy

California Institute of Technology

Pasadena, California

2015

(Defended May 29, 2015)

For my mom, dad, brother, and grandparents who would give anything for me.

Acknowledgements

I would first and foremost like to thank my advisor and mentor, Ali Hajimiri. Deciding to work with him was one of the best choices I have ever made. In addition to his mastery of a vast number of subject matters, he understands people. This is particularly useful in obtaining feedback regarding personality, work ethic, and lifestyle. He knows me better than I know myself. When I have doubted myself, his confidence in my capabilities has been a constant source of comfort. Aside from his technical teachings, he has had the resolve to improve me and my colleagues despite what is easy. He constantly takes time away from his family to help us. I am able to better appreciate his help because of my realization that critical advice is difficult to give because it is difficult to receive. He is a true Renaissance man and has engaged me in deep thoughts and discussions on all aspects of life ranging from science, literature, politics, history, psychology, and entrepreneurship. I am forever indebted to my faculty mentors, Azita Emami, Sandy Weinreb, Dave Rutledge, Changhuei Yang, and Hyuck Choo, who have been ever vigilant in lending a hammer, an ear, a hand, or a shoulder.

I am forever grateful for my girlfriend, Betty Wong. I feel like the luckiest guy in the world for being able to meet you years after I first stared at you, frozen, on the 51 bus at UC Berkeley. We are a team, and you are a persisting support to me. You have renewed my purpose in life. I hope that I can repay you even a small fraction of the joy you bring to me.

I have had the opportunity to experience and learn from the exceptional personalities of many of my colleagues. These experiences have deeply enriched my capabilities. Stephen Chapman has been an ever upbeat friend. His patience and lightheartedness have been a comfort in tumultuous times. He has had a large influence on my understanding of chemistry, biology, and life skills. Additionally, his lessons in lab safety have likely saved me from serious injury. Brian Hong is a highly theoretical, indefatigable, and thoughtful individual. From him, I learned that kindness does not come at a trade-off of personal ambition. He has the ability to completely separate emotions from logic. He has always been willing to lend two helping hands. I have had the honor of working with Torkom Pailevanian, a personified engineering pit bull. He is relentless, aggressive, and never takes 'no' for an answer. His unique skill set makes him a master tinkerer. I constantly worry that he is not getting enough sleep. Aroutin Khachaturian has the ability to persevere through difficult obstacles and hardship. I learned how nothing is ever an excuse for lack of success. He has

always been generous with his time and possessions. I am grateful to Florian Bohn, who is the pillar of ethics and morality. He embodies how a good citizen should behave. He has been a fantastic research advisor throughout my entire graduate career. Behrooz Abiri is an individual that breathes excellence in all aspects of his life. He is gifted with a brilliant mind (he is a walking encyclopedia and multiphysics simulator) and maintains an impeccable work ethic. These have allowed him to excel in all aspects of life, physical, mental, and relational. I cannot wait to see the great things he will accomplish. My experience with Kaushik Sengupta has shown me the amazing benefits of critical analysis. He is able to analyze situations and draw accurate conclusions that no one else does. He has been a cherished officemate and I dearly miss having his company. Kaushik Dasgupta is the undisputed king of debugging. One of the two seemingly impossible feats during my doctorate career was accomplished with him. His ability to fix broken research is due to his patience and joviality. I am thankful to Amirreza Safaripour. He is blessed with humility and a caring heart. His loyalty to his (countless) friends is unmatched. Constantine Sideris has the unmatched stamina and drive to barrel towards any goal. Seeing him in action is truly a sight to behold. Steven Bowers showed me the power of advocacy, mediation, and leadership. Matan Gal-Katziri is one of the rare individuals who will help you to the best of his ability even before you ask. I would also like to thank other lab members who have helped me along my journey: Edward Kheer, Mikko Varonen, Joseph Bardin, Juhwan Yoo, Firooz Aflatouni, Aydin Babakhani, Arthur Chang, Hua Wang, and Reza Fatemi. Other colleagues have also been helpful to my success: Manuel Monge, Saman Saeedi, Matt Loh, and Abhinav Agarwal, Mayank Raj, and Meisam Nazari. I have had the benefit to mentor and learn from many talented and unique undergrads: Torkom Pailevanian the bruiser, the softhearted Alexander Hu, Aroutin Khachaturian the optimist, Jeff Sherman the smiler, and the spunky Michelle Wang. I am also grateful to Michelle Chen, Tanya Owen, Carol Sosnowski, Christine Garske, and Anne Sullivan for being the lubricant which keeps our operations running smoothly. It has been an absolute pleasure working with our collaborators at the City of Hope: Behnam Badie, Jacob Belin, Ethan White, Darya Alizadeh, and Pengpeng Cao.

This research was generously supported by the Caltech CI^2 and City of Hope grants. I would like to thank Brian Armstrong for assisting with microscopy; Stephanie Johnson and Rob Phillips for their help in aiding DNA attachment chemistry; Habib Ahmad, Alex Sutherland and James Heath for guidance and tools in developing surface chemistry; and Derek Rinderknecht and Morteza Gharib for providing high power microscopes.

Abstract

We introduce an *in vitro* diagnostic magnetic biosensing platform for immunoassay and nucleic acid detection. The platform has key characteristics for a point-of-use (POU) diagnostic: portability, low-power consumption, low cost, and multiplexing capability. As a demonstration of capabilities, we use this platform for the room temperature, amplification-free detection of a 31 bp DNA oligomer and interferon-γ (a protein relevant for tuberculosis diagnosis). Reliable assay measurements down to 100 pM for the DNA and 1 pM for the protein are demonstrated. We introduce a novel "magnetic freezing" technique for baseline measurement elimination and to enable spatial multiplexing. We have created a general protocol for adapting integrated circuit (IC) sensors to any of hundreds of commercially available immunoassay kits and custom designed DNA sequences.

We also introduce a method for immunotherapy treatment of malignant gliomas. We utilize leukocytes internalized with immunostimulatory nanoparticle-oligonucleotide conjugates to localize and retain immune cells near the tumor site. As a proof-of-principle, we develop a novel cell imaging and incubation chamber for *in vitro* magnetic motility experiments. We use the apparatus to demonstrate the controlled movement of magnetically loaded THP-1 leukocytes.

Finally, we introduce an IC transmitter and power amplifier (PA) that utilizes electronic digital infrastructure, sensors, and actuators to self-heal and adapt to process, dynamic, and environmental variation. Traditional IC design has achieved incredible degrees of reliability by ensuring that billions of transistors on a single IC die are all simultaneously functional. Reliability becomes increasingly difficult as the size of a transistor shrinks. Self-healing can mitigate these variations.

Contents

List of Figures

List of Tables

Chapter 1

Introduction

Sensing and actuation are the interfaces of intelligent systems: they allow a functional system to adapt to its environment. Being able to monitor one's health and treat disease is the cornerstone of health care. Mankind's development of diagnostic tools and therapeutics has extended our lives and improved our well-being. In this dissertation, we discuss biosensing and magnetic actuation.

We first introduce the landscape of an important segment of health care diagnostics—*in vitro* diagnostics (IVD). We discuss the transition from central lab analyzers to patient-operated devices. A brief introduction of representative commercial devices is presented along with their core technologies. Next, we consider magnetic trafficking as a therapeutic for brain tumor treatment. We discuss the various types of brain tumors and the lack of effective treatment for them. We introduce the promising prospect of immunotherapy and how magnetic actuation can be of particular utility.

1.1 Point-of-use Diagnostics

IVD is a booming industry with an estimated global market capitalization of over $50 billion annually [1]. IVD is a rapidly growing industry due to the ability to detect early onset of disease and begin early treatment. Early treatment of disease usually increases probability of successful treatment and lowers treatment costs. The detection of a disease is primarily useful when the detection event affects a clinical decision.

1.1.1 Immunochemistry

Immunochemistry is the largest market within the IVD industry with a compound annual growth rate of 7% between 2012 and 2014 [1]. The market consists primarily of large automated immunoassay and clinical chemistry analyzers used in developed countries. Clinical chemistry analyzers are large, high-throughput, automated measurement systems capable of detection of a subset of hundreds of potential biomarkers in human bodily fluid. Some examples of these systems are the Beckman

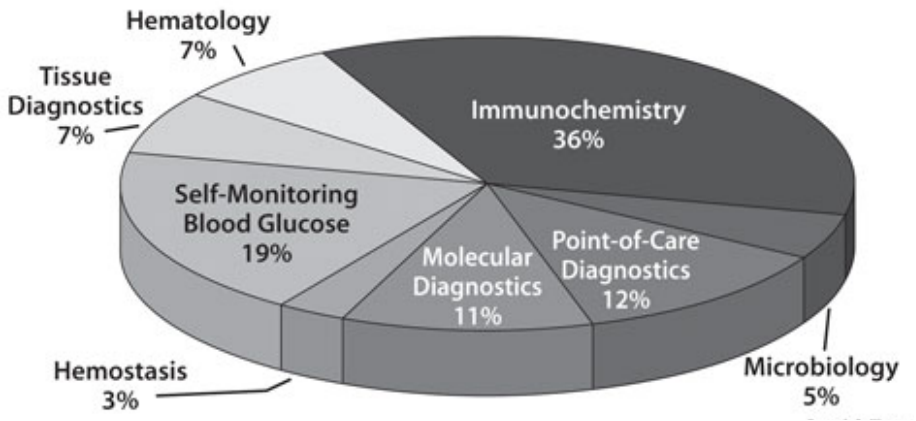

Figure 1.1: Global *in vitro* diagnostics (IVD) market in 2012 [1]. The IVD market is estimated to exceed $50 billion annually.

Coulter Unicel DxC 880i (Fig. 1.2), Roche Cobas Integra 6000, and Ortho VITROS 5600. These systems have a variety of instrumentation for full automation such as:

- Heater
- Refrigerator
- Fluid Mixing
- Waste Disposal
- Magnetic Separation
- Optical Analyzer
- Power Supply
- Reagents
- Fluid Handling
- Reaction Vessel
- Sample Vessel
- Consumables

Although these systems have extremely high throughput, they are expensive and require constant power, technician support, and a sterile lab facility to operate. Although this has been a boon for high volume tests in developed countries, it does not have the capability to operate in resource limited settings. Furthermore, it is difficult to transport, cannot be operated near the point of care, and is not suitable for infrequent testing.

Many analyzers rely on immunoassays for analyte detection. An analyte is a biomarker for a disease (for example, a protein, molecule, or even an antibody (used in serological tests)). Immunoassays were first developed in the 1950s and their use was popularized in the 1970s. They detect analytes through the labeling of antigens by antibodies. The popularity of immunoassays is largely attributable to the relative ease of developing antibodies for a particular antigen.

To develop an antibody (also known as immunoglobulin) for an antigen, a host mammal (usually a mouse, rabbit, goat, or sheep) is immunized against the antigen through antigen injection. The host's immune system will naturally develop specific antibodies against the antigen. Next, the spleen is removed from the host and disassociated in a culture medium. The B cells from the disassociated spleen are then isolated and cultured. Myeloma cells are introduced and fused to B cells using polyethylene glycol (PEG) to form hybridomas. The resulting culture can be used to produce polyclonal antibodies or separated to form monoclonal antibodies. Polyclonal antibodies are heterogeneous and bind to potentially overlapping epitopes. Monoclonal antibodies have a specific Fab region that binds to a specific antigen epitope.

Figure 1.2: Beckman Coulter Unicel DxC 880i. This large immunoanalyzer is a fully automated system requiring constant power, lab infrastructure, and technician support.

There are two types of immunoassays: competitive and non-competitive. In competitive immunoassays (simpler than a non-competitive immunoassay), two antigens compete to bind to an antibody. Binding to the target analyte is energetically favorable to binding to the non-target antigen. The non-target antigen is usually labeled. The amount of signal present from the labeled, bound antigen, or labeled, unbound antigen can be anti-correlated to the concentration of target analyte in solution. In a non-competitive immunoassay, a single target analyte is bound to a single (one-site) or pair (two-site) of antibodies. In a one-site noncompetitive immunoassay, a labeled antibody is bound to an analyte. Unbound antibodies are separated or washed away and the signal from the remaining antibodies are measured and correlated to analyte concentration. In a two-site noncompetitive immunoassay, such as a sandwich enzyme-linked immunosorbent assay (ELISA), a

capture antibody binds an analyte to a substrate and a probe antibody labels the analyte. The amount of signal present from the probe antibody is correlated to the presence of target analyte.

An immunoassay can also be categorized as a heterogeneous or homogeneous. In a heterogeneous assay, analytes are captured onto a substrate and bound to a labeled antibody. Unbound labels are washed or separated from the analyte. In a homogeneous assay, bound and unbound analytes are differentiated by some mechanism and does not require separation of analyte from label. Binding to a substrate is also not required. This simplifies sample preparation and handling.

Magnetic particles are desirable for IVD as a binding substrate because no centrifugation is needed and no clotting occurs, and they can be simultaneously used for washing and elution, they are inexpensive, they can be easily concentrated, and they can be used for higher IVD throughput.

1.1.2 Molecular Diagnostics

Molecular diagnostics is one of the fastest growing markets in the IVD industry with a compound annual growth rate of 11% between 2012 and 2014 [1]. It consists of genome and proteome analysis of humans and disease for clinical decisions. It consists of four categories: pathogenomics, pharmacogenomics, genetic testing, and blood donor screening.

1.1.2.1 Pathogenomics

Pathogenomics extends beyond pathogen infections. Metagenomic analysis of microbe diversity elucidates our understanding of complex interdependencies of disease and microbes. The human intestinal microbiota, for example, is composed of between 10^{13} to 10^{14} microorganisms with at least 100 times as many genes as the human genome [6]. These microorganisms have been linked to topics such as obesity [7], immunity [8], and cancer [9].

1.1.2.2 Pharmacogenomics

The human population shares 99.9% of its DNA sequence. The remaining 0.1% of variations account for virtually all our phenotypical differences. Approximately 80% of our genetic differences are due to single nucleotide polymorphisms (SNP). Other variations consist of sequence repeat, deletion, and chromosomal rearrangement. Our genetic variations can affect our drug metabolism. This becomes important when deciding the proper dosage levels of pharmaceutical drugs in treating disease.

One example of pharmacogenomics is the assessment of drug metabolism of the enzyme family Cytochrome P450. P450s are believed to be involved in approximately 75% of drug metabolism [10]. One of the members of the family, Cytochrome P450 2C9 (CYP2C9), is encoded by CYP2C9 gene. Over 50 SNP are located on the CYP2C9 gene, and thus, it is highly polymorphic [11]. CYP2C9 activity is responsible for the determination in warfarin dosing, an anticoagulant used to treat

thrombosis (blood clotting) [12]. However, dosing must be determined on a case-by-case basis and can vary by 20X [12]. An insufficient dose leads to illness while an excessive dose leads to severe bleeding. Nanosphere's commercial Verigene system assesses two alleles of the CYP2C9 gene to determine proper warfarin dosing [13].

1.1.2.3 Genetic Testing

Human genetic analysis is vital in the fields of forensics, paternity testing, inherited diseases, disease predisposition, and family planning.

1.1.2.4 Blood Donor Screening

High throughput screening for blood donations is essential for protecting the recipient from blood-borne pathogens. Donated blood is usually first screened using a high sensitivity, low specificity diagnostic. Next, false positives are eliminated using a higher specificity diagnostic. The WHO recommends a country have bare minimum screening for HIV-1 and HIV-2 using a combination of HIV antigen-antibody or HIV antibodies, hepatitis B using surface antigen HBsAg, Hepatitis C using HCV antigen-antibody or HCV antibodies, and syphillis using treponemal antibodies [14]. However, it estimates 47% of donations in low-income countries are tested in laboratories without quality assurance [15].

1.1.3 Point-of-Care Diagnostics

Point-of-care (POC) diagnostics is testing performed at or near the site where clinical care is delivered [16]. The last decade has seen substantial growth in POC diagnostics [1, 17]. The development of POC devices reduces initial capital costs, resource and infrastructure constraints, diagnosis and treatment time delay, and inflexibility associated with central lab analyzers [18, 19]. Several POC diagnostic systems have been recently developed using various detection methods such as electrochemical, magnetic, mechanical, optical, or electronic detection methods. A brief review of a few recent POC diagnostic systems is provided.

Nanosphere's Verigene system [13] (Fig. 1.3) is a technology based upon Professor Mirkin's bio-barcode assay [20]. The assay uses magnetic labels coated with capture antibodies or nucleic acids for a target DNA or protein. Gold nanoparticles are functionalized with a separate capture antibody or oligonucleotide, and an encoding oligonucleotide. After magnetic separation, the oligonucleotides are released and optically scanned or imaged using scattered light from evanescent excitation. Signal amplification occurs from nanoparticle catalyzed silver reduction. The detection system is able to detect infections (including respiratory, gastrointestinal, and bloodstream) as well as perform cardiac tests [13].

(a)

(b)

Figure 1.3: Nanosphere's Vergene diagnostic system. (a) Verigene Reader and (b) disposable detection cartridge.

Cepheid Inc.'s GeneXpert system [21] (Fig. 1.4) utilizes amplification and integrated sample preparation for the multiplexed detection of various infectious diseases. The system uses a miniaturized sonicator for mechanical cell lysis [22]. Amplification is achieved using PCR. Detection consists of real-time fluorescence detection. The company is able to achieve lower costs by a lack of commitment to lateral flow patents. Integrated sample preparation remains their largest hurdle. Cepheid's debut was after the 2001 anthrax attacks where the system was purchased by several US federal agencies for anthrax detection. Since then, the system has been backed by the World Health Organization (WHO) for tackling HIV in Africa as well as the Bill & Melinda Gates Foundation. The GeneXpert system costs approximately $30,000 (depending on capabilities) and the test cartridge costs approximately $25 unsubsidized.

The Xpert MTB/RIF assay has the potential to revolutionize tuberculosis (TB) diagnostics. In 2013, a total of 9 million people contracted TB and 1.5 million died from the disease, making it the world's second greatest infectious agent killer (after HIV) [23]. Drug resistant TB remains a large global problem. A 90bp mutation region in TB determines its resistance to refampin. A combination of 5 molecular beacons could determine a strain's resistance to refampin and optimize treatment. However, challenges remain as the system requires uninterrupted power and a lab to operate.

GenMark Dx's (formerly Osmetech) eSensor XT-8 is a gold electrode PCB based diagnostic (Fig. 1.6) [2]. The system uses polymerase chain reaction (PCR) amplification to improve sensitivity. The

(a)

(b)

Figure 1.4: Cepheid's GeneXpert diagnostic system. (a) Automated instrument and (b) disposable detection cartridge.

sample preparation is shown in Fig. 1.7a. Current capabilities enable a multiplexibility of 72. The disposable cartridge combines the PCB sensor with microfluidics. Detection is based off of an amperometric measurement of ferrocene. The sensing technology is shown in Fig. 1.7b.

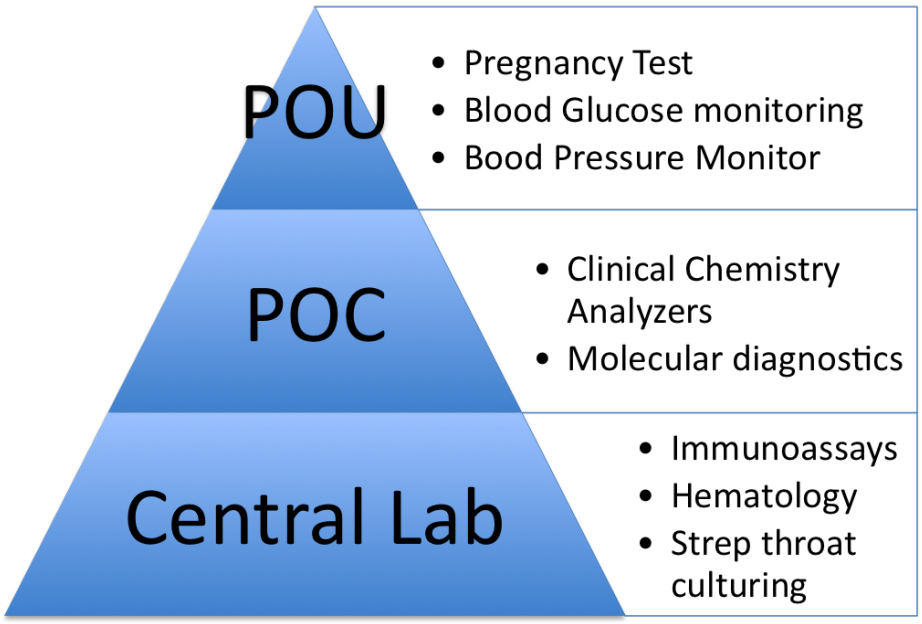

Figure 1.5: Diagnostic Devices Landscape. Diagnostic devices can be broadly classified under three categories: central lab analyzers, Point-Of-Care, and Point-Of-Use.

(a)

(b)

Figure 1.6: GenMark's eSensor XT-8 diagnostic system. (a) Detection instrument and (b) detection cartridge [2].

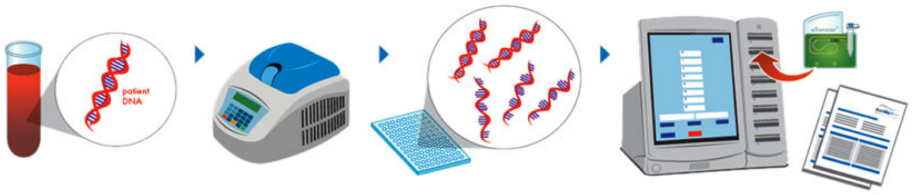

1 Patient sample is obtained & DNA extraction is performed.

2 Polymerase chain reaction (PCR) is performed to amplify patient DNA, referred to as target DNA.

3 An exonuclease reaction is performed to create single-stranded DNA.

4 Multiplex detection and result reporting are performed on the XT-8 system.

(a)

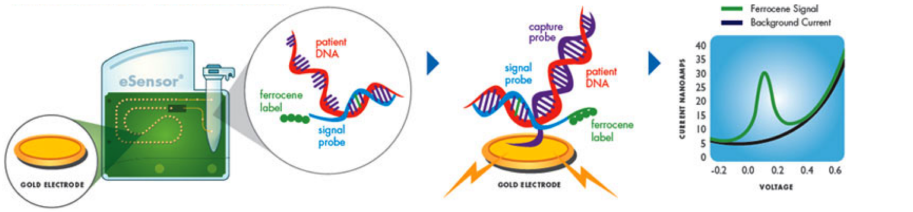

1 The target DNA is mixed with the signal probe solution. If the applicable target DNA is present, hybridization to the signal probes occurs immediately.

2 The solution is pumped through the cartridge's microfluidic chamber and the target DNA/signal probe complex completes the reaction with the pre-assembled capture probe.

3 Voltage is swept across each electrode and target DNA is analyzed by electrochemical detection.

(b)

Figure 1.7: GenMark's eSensor XT-8 (a) sample preparation and (b) detection technology [2].

1.1.4 Self-monitoring Blood Glucose and the Point-of-Use Diagnostic

As traditional central lab testing has evolved into POC diagnostics, the prevalence of point-of-use (POU) diagnostics has increased. A POU diagnostic can be performed by the end patient and some or all of the clinical care is administered by the end patient. Perhaps the best example of a POU diagnostic is the handheld blood glucose monitor.

A blood glucose monitor is used to manage Type 1 and Type 2 diabetes mellitus (DM). Diabetics require a regimen of insulin injections to help manage blood sugar levels. The monitor helps to evaluate the effectiveness of previous insulin injections and to determine the dosage next injection. Although proper treatment also requires a doctor's evaluation of the patient's cardiovascular system, the monitor combined with self-administered insulin injection enables the patient more flexibility and more effective treatment at substantially lower treatment costs.

Therefore, POU diagnostics has a distinct advantage in treating patients in limited resource settings, decreasing the time between diagnosis to treatment, and empowering the patient through increased flexibility. POU diagnostics are particularly useful in diagnosing diseases where early detection is critical to successful treatment. Some examples of favorable disease candidates for POU diagnostics include sepsis, pertussis (whooping cough), malaria, tuberculosis (TB), influenza, and human immunodeficiency virus (HIV).

1.1.5 A POU Diagnostic for Protein and Nucleic Acid Detection

We propose a POU diagnostic platform compatible with two of the largest IVD markets: molecular diagnostics and immunochemistry. This detection system is based on the frequency-shift biosensor [24–26]. Frequency-shift based magnetic sensing is a measurement technique utilizing a complementary metal-oxide-semiconductor (CMOS) integrated-circuit (IC) chip for magnetic label detection. The sensing scheme leverages the low-cost manufacturing for IC chips while demonstrating potential for multiplexing capabilities. In this article, we present modifications to this scheme for POC viability. We introduce a handheld reusable reader and a disposable open-well cartridge for the detection of nucleic acids and antigens. The diagnostic system utilizes a novel "magnetic freezing" technique to reduce measurement time, obviate baseline measurement before or during biological assay, and reduce sensor noise. We utilize these enhancements for the room temperature, amplification-free detection of a 31 base-pair DNA oligomer and the interferon-γ (IFN- γ) protein. We have demonstrated reliable measurements down to 100 pM for the DNA assay and 1 pM for the protein.

1.2 Magnetic Particle Trafficking for Brain Tumor Therapy

1.2.1 Brain and Central Nervous System Tumors

The human brain is composed of glial cells, blood vessels, and neurons. Gliomas are tumor cells derived from glial cells in the brain or spine. Gliomas account for 30% of all brain and central nervous system (CNS) tumors but 80% of malignant brain tumors [27]. Approximately 20% of gliomas are benign; the remaining are malignant [3]. Malignant gliomas are the most common and fatal primary brain neoplasm [28, 29] with median survival times between 1-2 years [3]. Gliomas are divided into three categories: ependymomas, astrocytomas, and oligodendrogliomas. Ependymomas make up 2-3% of gliomas and tend to occur intracranially in children. Astrocytomas make up approximately half of all brain tumors and are divided into grades (by the WHO) of increasing severity: I (pilocytic astrocytoma, pleomorphic xanthoastrocytoma, subependymal giant cell astrocytoma, and subependymoma), II (low-grade astrocytoma and mixed oligoastrocytoma), III (anaplastic astrocytoma), and IV (glioblastoma multiforme). Oligodedrogliomas are divided into two grades: II (low grade) and III (high grade analplastic).

Histology	# Cases	1-Yr	2-Yr	3-Yr	4-Yr	5-Yr	10-Yr
Pilocytic astrocytoma	2,538	97.64%	96.48%	95.47%	94.66%	94.05%	91.32%
Protoplasmic & fibrillary astrocytoma	718	75.39%	61.53%	55.95%	50.58%	47.58%	35.36%
Anaplastic astrocytoma	3,107	60.98%	43.02%	34.70%	30.26%	27.00%	19.01%
Astrocytoma, NOS	3,571	70.08%	59.78%	53.88%	49.79%	46.82%	36.20%
Glioblastoma	21,910	35.20%	13.17%	7.54%	5.50%	4.70%	2.32%
Oligodendroglioma	2,631	94.15%	89.95%	85.96%	82.32%	79.25%	62.62%
Anaplastic oligodendroglioma	1,058	80.30%	66.16%	58.58%	52.85%	48.42%	33.21%
Ependymoma/anaplastic ependymoma	1,938	93.78%	89.26%	86.01%	83.43%	82.27%	77.17%
Mixed glioma	1,425	87.42%	75.56%	68.54%	63.00%	58.35%	45.52%
Glioma malignant, NOS	3,096	60.69%	49.11%	45.72%	43.22%	41.76%	36.40%
Neuroepithelial	127	52.40%	41.46%	40.61%	34.71%	31.55%	27.69%
Malignant neuronal/glial, Neuronal and mixed	575	88.91%	80.32%	77.07%	72.49%	71.56%	59.82%
Embryonal/primitive/ medulloblastoma	2,050	82.35%	71.96%	67.09%	63.90%	61.69%	55.20%
Lymphoma	3,712	47.65%	38.76%	34.09%	30.87%	28.21%	20.78%
Total: All Brain and CNS[d]	52,508	57.22%	42.99%	38.09%	35.38%	33.72%	27.92%

[a]The cohort analysis of survival rates was utilized for calculating the survival estimates presented in this table. Long-term cohort-based survival estimates reflect the survival experience of individuals diagnosed over the time period, and they may not necessarily reflect the long-term survival outlook of newly diagnosed cases.
[b]Rates are an estimate of the percentage of patients alive at one, two, three, four, five, and ten year, respectively.
*[c] Estimated by CBTRUS using Surveillance, Epidemiology, and End Results (SEER) Program (www.seer.cancer.gov) SEER*Stat Database: Incidence - SEER 17 Regs Research Data + Hurricane Katrina Impacted Louisiana Cases, Nov 2010 Sub (1973-2008 varying) - Linked To County Attributes - Total U.S., 1969-2009 Counties, National Cancer Institute, DCCPS, Surveillance Research Program, Cancer Statistics Branch, released April 2011 (updated 10/28/2011), based on the November 2010 submission.*
[d]Includes histologies not listed in this table.
Abbreviations: SEER, Survival, Epidemiology and End Results; NOS, not otherwise specified.

Figure 1.8: One-, two-, three-, four-, five-, and ten-year relative survival rates[a,b] for selected malignant brain and central nervous system tumors, SEER 17 registries, 1995-2008[c] [3]. Glioblastomas are the most common type of brain and CNS tumor with median survival time less than one year.

1.2.2 Malignant Glioma Treatment Options

The three most common treatment options for malignant gliomas are chemotherapy, surgery, and radiation therapy. Chemotherapy is the use of one or several chemical substances used to treat gliomas. However, chemotherapeutic agents are usually cytotoxic. During treatment, less than 1% of the chemotherapeutic agent is delivered to the tumor cells. In brain and CNS tumors, this fraction is further reduced by the blood-brain barrier [30]. This results in healthy tissue receiving toxic substances and damage. Common side-effects of chemotherapy include alopecia (hair loss), mucositis (digestive tract inflamation), myelosuppression (suppressed blood production), and immunosuppression (suppressed immune function). On the other hand, surgery is a difficult treatment option for deeply embedded tumors and sacrifices essential peripheral healthy tissue. Finally, radiation therapy can damage essential healthy tissue and have many undesirable side effects.

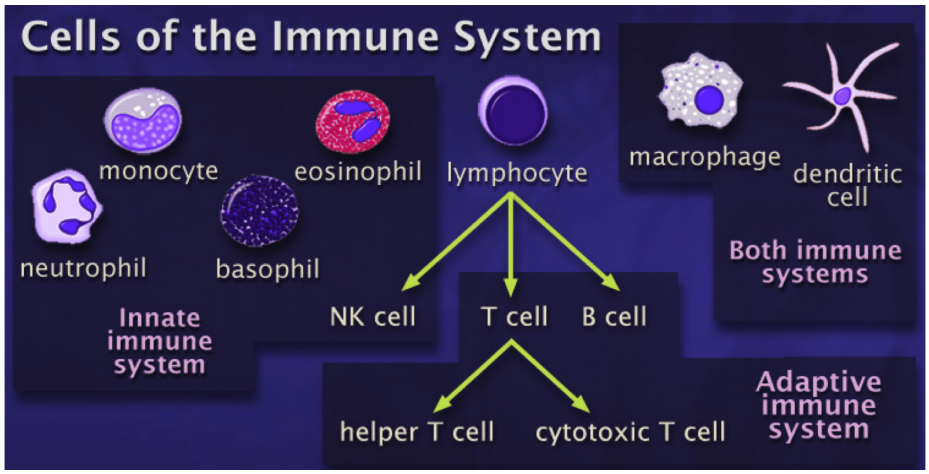

Figure 1.9: Various types of leukocytes [4]. Leukocytes can be classified by innate or adaptive immunity.

A promising new class of cancer treatment is immunotherapy [31]. One subset of immunotherapy is activated immune response, whereby the patient's leukocytes (white blood cells) are stimulated to elicit a response to the tumor (Fig. 1.9). After the activated response, the likelihood of immunological memory of the tumor is increased (retained immunity). Stimulated immunotherapy uses the body's own immune system to trigger its ability to seek out and kill cancer. Our collaborators have shown that carbon nanotubes conjugated with CpG oligodeoxynucleotides resulted in the stimulation of toll-like receptor-9 (TLR9) and cured 50-60% of mice with established gliomas [29]. This nanotube-CpG construct is readily taken up by macrophages, microglia, NK cells, and dendritic cells [29].

Activation of TLRs enhances the uptake of microorganisms by phagocytic cells, promotes secretion of Th1 cytokines, and mediates leukocyte recruitment to infected tissues. Generally, TLR9 is not found on the cell surface, but is initially located in the endoplasmic reticulum (ER) and is

then found colocalized with CpGs in the lysosomes following stimulation [32]. Therefore, because CpG-induced immune stimulation is dependent upon TLR9 interacting with CpG inside the endosomal compartment, using a platform that achieves endosomal delivery of CpG may be an attractive strategy for enhancing CpG efficacy [33].

When the cured mice were reintroduced to intracranial tumors, full immunity was retained. Furthermore, they have shown that uptake of CpG coated nanoparticles (NP) in tumor associated macrophages improves NP delivery and immune memory [34]. Various nanoparticles have been investigated as potential candidates for the delivery of CpGs, including liposomes [35], self-assembling DNA nanoparticles [36], poly(lactic-co-glycolic acid) nanoparticles [37], and gold nanoparticles [38]. CpG induces an immune response because it is a single-stranded DNA. Naturally occurring single-stranded DNA is indicative of a bacterial or viral infection and therefore elicits an inflammatory immune response. NP CpG is believed to be more effective than free CpG because the NP acts as an "anchor" for the CpG and increases its retention time near the tumor site.

1.2.3 Magnetically Trafficking Macrophages for Guided Immunotherapy

Because increased retention time of CpG near the glioma site appears to be beneficial for immunotherapy [34], this effect could potentially be enhanced using magnetic force. Instead of non-magnetic NPs, iron-oxide NPs could act as a new magnetically guidable substrate for the CpG. We hypothesize that using super paramagnetic iron oxide nanoparticles (SPIONs) as the delivery platform for the CpG would enable magnetic control of immune cells that endocytosed the particles. SPIONs respond to magnetic fields and allow for the controlled delivery of conjugated chemotherapeutics [39]. This technique may even allow for targeted delivery deep within the body [40, 41]. Magnetic targeting of drug delivery has been applied to brain tumors [42]. Recently, magnetic targeting has been extended to cells by labeling desired cell populations with SPIONs and other magnetic particles. One focus of this work has been attracting loaded cells to magnetized implanted devices, such as stents [43, 44]. Another primary application has been targeting loaded stem cells for regenerative medicine [45–48]. A limited number of publications have also described magnetic control of loaded immune cells [49]. Clinically, we envision that a SPION-based immunotherapy could be injected intracranially, internalized by local immune cells, and then enable the magnetically-controlled migration of these activated immune cells for the treatment of multifocal disease or deep brain tumors. Given a system that can adjust the field in the brain volume, particles could be aggregated and retained near the tumor site. Leukocytes such as macrophages would become activated after endocytosis of the CpG NPs. After endocytosis, the macrophages would become aggregated and retained near the tumor site, increasing their effectiveness in treating the tumor. Additionally, the field could be temporally adjusted as the neoplasm spreads or shrinks in size. Another benefit of magnetic particles is that they can be used as a magnetic resonance imaging contrast for *in vivo*

evaluation of macrophage distribution. A few possible treatment scenarios could be attempted:

- Macrophages would first be extracted from the patient. The macrophages would be introduced to a CpG NP media solution. After endocytosis, the macrophages would be reintroduced to the patient. A magnetic field profile would guide the macrophages to the tumor site.
- Macrophages would similarly be extracted from the patient. After introduction and endocytosis of CpG NPs, the macrophages would be injected directly to the tumor site. A magnetic field profile would retain the activated macrophages near the tumor site.
- Instead of macrophage extraction, CpG NPs could be directly injected to the tumor site. A magnetic field profile would retain particles near the tumor site while the body's immune system recruits leukocytes to the NPs.

1.2.4 Prototyping a Wearable, Dynamically Programmable Magnetic Field (DPMF) Head Enclosure

The eventual treatment will require precise 3D magnetic control of magnetic field profiles within the brain. This could consist of a collection of programmable current elements enclosing a portion of the head. By choosing the magnitude and direction of a collection of current elements, a wide variety of magnetic fields can be achieved. However, monitoring the effectiveness of guided cell motility in the brain is difficult. Magnetic resonance imaging (MRI) would first require removal of the programmable current elements. It is difficult to image to high resolutions on a short timescale using MRI, but longer timescales would be prohibitively expensive to operate (despite recent improvements from compressed sensing). 3D slice fluorescence imaging of a brain is more suitable for an endpoint evaluation and does not allow for time-lapsed imaging. Radioactive isotope imaging would also require complicated infrastructure. To evaluate both short-term and long-term motility of nanoparticles and cells, we designed a novel imaging, incubation, and magnetic manipulation cell box (Fig. 1.10a). The cell box allows for long-term viability of cells while adapting to a standard 100 mm petri dish. A large cell media reservoir provides nutrients to cells while an internal atmosphere distribution system ensures pH control of the media. The cell box and petri dish are compact enough to be imaged with typical inverted microscopes. A clear glass coverslip separating the DPMF and cell media allows for easy visual alignment. A waterproof seal separates electronics from cell media. A custom DPMF controller (Fig. 1.10b) enables the DPMF to interface to a computer for accurate timing of magnetic profile actuation.

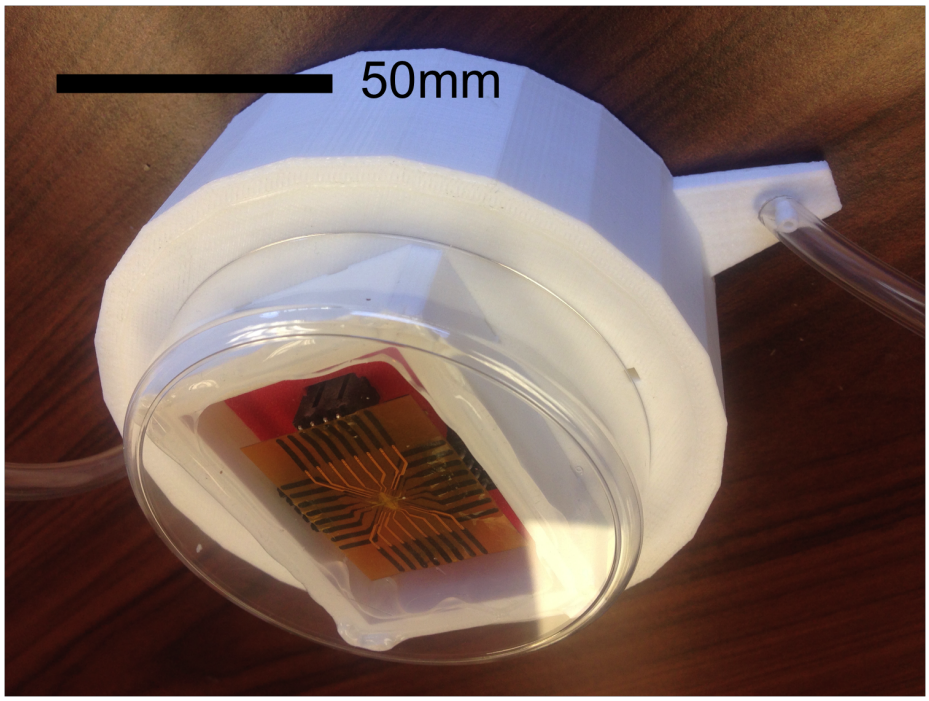

(a)

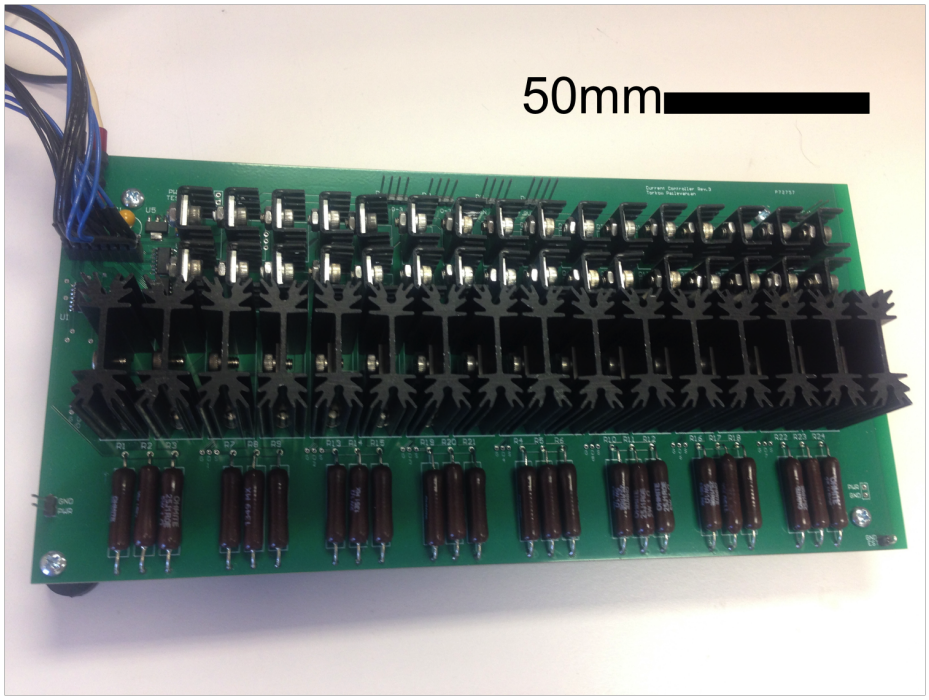

(b)

Figure 1.10: (a) One of the core components of the DPMF device is a 3D-printed cell box. The box is printed from ABS plastic and contains life-support features for magnetically trafficked cells. A CO_2 inlet port and distribution channels ensure optimal pH of cell media. A coverslip slot allows for the waterproof attachment of a large coverslip. The interface ensures that the system electronics do not interfere with cell media. The cell box adapts to a standard 100 mm petri dish and fits on typical inverted microscopes. (b) A computer-interfaced controller adjusts the current distribution of the DPMF. The total size of the controller is 100 mm x 200 mm.

1.3 Contributions

In this dissertation, we present an IC-based platform for biological sensing. We also propose a method for magnetically-guided immunotherapy of intracranial gliomas. We introduce an imaging, incubation, and magnetic manipulation chamber for *in vitro* cell trafficking. We also use principles of self-healing IC design in a mm-wave transmitter architecture and a high-power stacked PA. Specifically, we demonstrate:

- A handheld, reusable reader and low-cost disposable cartridge for the detection of nucleic acids and antigens.
- A novel magnetic freezing technique for baseline measurement elimination and to enable spatial multiplexing.
- Room temperature, amplification-free detection of a 31 bp DNA oligomer and the interferon-gamma protein.
- Reliable assay measurements down to 1 pM for protein and 100 pM for DNA demonstrated.
- A general protocol developed for adapting sensor to any of hundreds of commercially available immunoassay kits AND custom designed DNA sequences.
- A custom cell imaging and incubation chamber for long-term magnetic manipulation of immune cells.
- A 2D magnetic field array designed for *in vitro* manipulation of nanoparticle-loaded leukocytes.
- Speeds of 140 μm/s achieved for dynamic nanoparticle movement and 300 μm/s for cell aggregation.
- As a demonstration of cell trafficking, THP-1 lymphocytes loaded with SPION-CpG particles are magnetically manipulated.
- A passively cooled current controller designed for computer-interfaced control of magnetic fields.
- Self-healing algorithm and infrastructure (phase rotator, phase detector, RF power sensor, coupler, DC current sensor, digital control) developed for a power mixer and a high power amplifier.

1.4 Organization

The thesis is organized as follows. In section 2.1, we introduce a platform for biosensing. Surface chemistry protocols are developed to functionalize a standard IC chip for biological detection.

Biological protocols are developed using these functionalizations for the detection of proteins and nucleic acids. In section 2.2, we develop the theory of magnetic particle manipulation. The theory describing motility in solution is also described. In section 3.2 and section 3.3, we introduce sensing and actuation of a very different kind: electronic sensors and actuators are designed to "self-heal" the performance of two IC architectures. In section 3.2, we detail a segmented power-mixer based mm-wave transmitter capable of multi-Gbps wireless communication. Self-healing capabilities such as symbol healing and efficiency optimization are introduced. In section 3.3, we present a high power stacked PA with self-healing capabilities. In chapter 4, we provide a more detailed description of biological protocols.

Chapter 2

Magnetic Sensing and Actuation

2.1 A Handheld Magnetic Sensing Platform for Antigen and Nucleic Acid Detection

2.1.1 Introduction

Point-of-care (POC) diagnostics represents a growing segment of the health care industry [17]. Although many types of sensors have been proposed with high sensitivities, few have demonstrated the key features that will allow a device to reach widespread use: low-cost, multiplexing, portability, easily integrated sample preparation, and quick measurement time [18, 19]. In this dissertation, we present a complete handheld diagnostic device (Fig. 2.1) with two fully implemented assays for proteins and nucleic acids (Fig. 2.3). It is based on the novel "magnetic freezing" scheme that removes the need for baseline measurements, allows for multiple sensor measurements, and eliminates the long warm-up and calibration phases. To the best of our knowledge, magnetic freezing is a new technique and previously unpublished. We have devised a disposable, low-cost single chamber cartridge-based approach, which simplifies the sample handling significantly (Fig. 2.1). We have developed all the necessary surface chemistry to functionalize the surface of a standard CMOS chip, further reducing the cost and complexity of this handheld diagnostic device. We also eliminate expensive and bulky infrastructure that limits other sensing technologies such as microfluidic pumps and optical elements. A crucial component of any POC diagnostic is the biosensor used to detect biologically relevant targets. Many biosensors have been proposed utilizing optical (e.g., [50–52]), electrochemical (e.g., [53–60]), mechanical (e.g., [61]), or magnetic (e.g., [24, 62–66]) sensing modalities. Magnetic based platforms enjoy higher sensitivity and virtually non-existent background due to the absence of strong magnetic properties in most biological samples. The same magnetic labels can also serve as means of magnetic manipulation during sample preparation (e.g., separation, purification, lysing, etc.) in an integrated system [55, 63, 67–69].

One promising class of magnetic sensors is the complementary metal-oxide-semiconductor (CMOS)

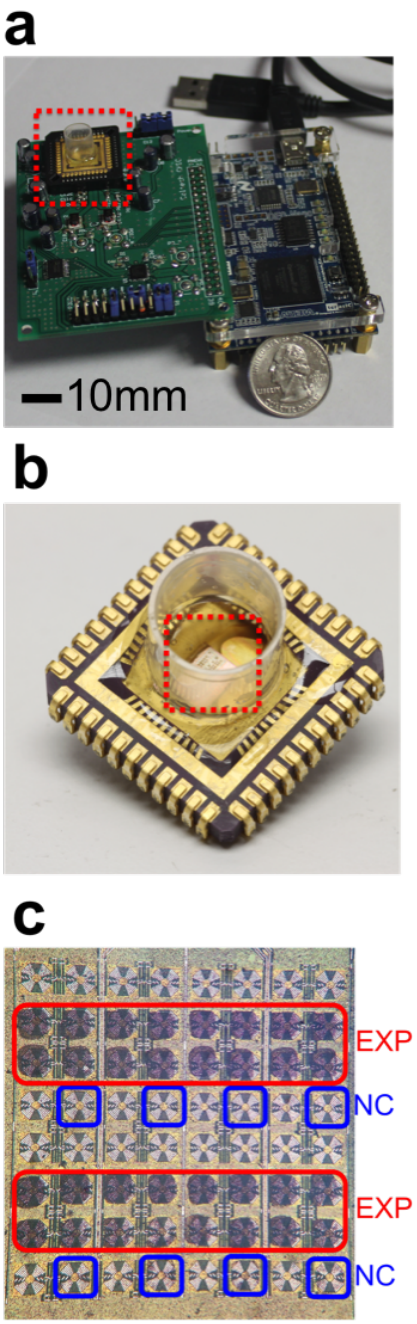

Figure 2.1: (a) Handheld Diagnostic Device. The device consists of a plug-in cartridge, circuit board, and single USB data interface cable for communication and power. (b) Disposable Cartridge. The disposable cartridge consists of an electrically connected integrated circuit chip inside a polypropylene well. (c) Chip Surface after Immunoassay. The chip inside the cartridge has 48 sensor sites and 16 reference sensors. Sensor sites designated by EXP and NC were used for printing the capture probe or negative control, respectively. Some sensing sites were left blank to examine background binding. In the DNA and antigen assays, the presence of biological targets leads to the accumulation of magnetic beads over the sensor.

frequency-shift based magnetic resonating sensor [24–26]. It relies on detecting the shift in the natural frequency of a free-running oscillator based on an electromagnetic resonator in the presence of external magnetic material. The resonator is often implemented on a silicon chip using an inductor, L, and a capacitor, C, forming an LC resonator. When a magnetic bead is in the vicinity of the inductor, it increases its inductance, which in turn lowers the resonance frequency. This leads to a small yet discernible drop in the oscillation frequency that is registered by electronically counting the number of cycles over one or multiple time intervals. The frequency shift can be correlated to the number of beads near the resonator. A single-chip array of frequency shift sensors was designed using integrated circuits (IC) in a CMOS process and previously reported [24]. A novel noise reduction technique, correlated double counting [25], was used to further enhance the chip's sensitivity. This CMOS chip was used to implement the handheld diagnostic reported here. The CMOS implementation is central to a low-cost, low-power implementation of this handheld diagnostic system due to its highly favorable cost structure in large volumes. The sensor has the benefits of low power, low cost, and high scalability.

Although the frequency-shift biosensor of Wang, et al. [24] was proposed for potential biological applications, several important challenges had to be overcome before its widespread deployment. It was observed that to achieve high accuracy measurements, each sensor oscillator had to be allowed to run (warm up) for long periods of time up to 30 min. Furthermore, to reduce the detection noise, the beads needed to be rapidly removed from the sensor surface to obtain a baseline right after the sample read. This rapid removal was necessary to do the two measurements within a time interval shorter than the drift time constants of the sensor oscillator. In a realistic biological experiment, the experimental interval is much longer than the drift time constant due to washing, target binding, and bead binding. Additionally, replicate measurements on multiple sensors would not allow for any warm-up time. To remedy these obstacles, we have developed a new technique called magnetic freezing. By saturating the magnetization of the magnetic beads with a small permanent magnet, the bead's effect on the sensor is neutralized. This obviates the need for a baseline measurement before the experimental assay, thereby reducing frequency drift and improving the sensor signal-to-noise ratio. Additionally, the sensor does not need to measure during the biological assay.

Another hurdle for widespread adoption is the physical size and cost of the biosensor measurement equipment. In this design, we have integrated the entire functionality of the sensor onto a reader printed circuit board (PCB) that in tandem with a processing unit board constitute the entirety of the reusable unit that connects to USB (Fig. 2.1). We have also designed a disposable open-well cartridge that combines all sensor sites (48 active and 16 reference) in a single reaction well (Fig. 2.1). The single well allows for easy sample and reagent loading without the need for microfluidic pumps or structures. This design offers the option to perform the biological assay separately on a single or multiple disposable cartridges and to plug them (batch processing) into a socket on

the reader PCB at the conclusion of the biological assay. This approach significantly lowers the marginal bill materials for the reader to less than $10 and the disposable cartridge to less than $1 in large volume. In order to demonstrate the viability of the sensor for biologically relevant assays, we have developed and demonstrated two representative practical assays detecting protein and nucleic acid targets [70]. We performed these two exemplary assays using our CMOS magnetic handheld diagnostic reader to detect an interferon-γ protein (relevant for Tuberculosis diagnostics) and a 31 bp DNA oligomer. This is the first demonstration of complete nucleic acid or protein assays using a CMOS frequency-shift magnetic diagnostic sensor to the best of our knowledge. All assays were completed at room temperature without any need for amplification. We demonstrated detectable concentrations of DNA between 100 pM-10 nM and protein between 1-30 pM in our first demonstration. Our developed assay incorporates surface chemistry compatible with not only our frequency-shift biosensor, but also with any standard CMOS IC chip.

2.1.2 Handheld, Portable Cartridge Reader

Our handheld, diagnostic device consists of two major components: a small, disposable cartridge and the reader (Fig. 2.1). The disposable cartridge consists of the sensor chip mounted on a chip carrier and protected with a polypropylene housing. The reader consists of a commercial field-programmable gate array (FPGA) development board (terasIC, Dover, Delaware) with a custom-designed PCB 2.2. The FPGA provides both power and data channel to the PCB, and bio sensor chip responds to programming sequence sent from the FPGA with a differential oscillation frequency of 900Mhz to 1GHz 200mV V_{p-p} in OUTN and OUTP. The frequency divider chip divides down the frequency by 22 and converts it to CMOS level(3.3V V_{p-p}) so that the FPGA will be able to receive it.

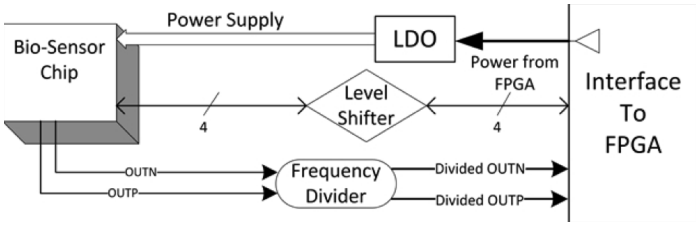

Figure 2.2: Block diagram of digital reader.

The sensing scheme caters to a very simple and small form factor. Data processing consists of a frequency divider ($\div 22$) and digital counter. Four supply biases are used to bias/power the chip. A crystal oscillator serves as a frequency reference and clock. The sensing parameters are relayed to on-chip shift registers. The device communicates to a computer through a single USB cable, which also provides power to the unit. The entire biological assay is performed in the well of the cartridge. At the end of the assay, the cartridge is plugged into the reader for data acquisition.

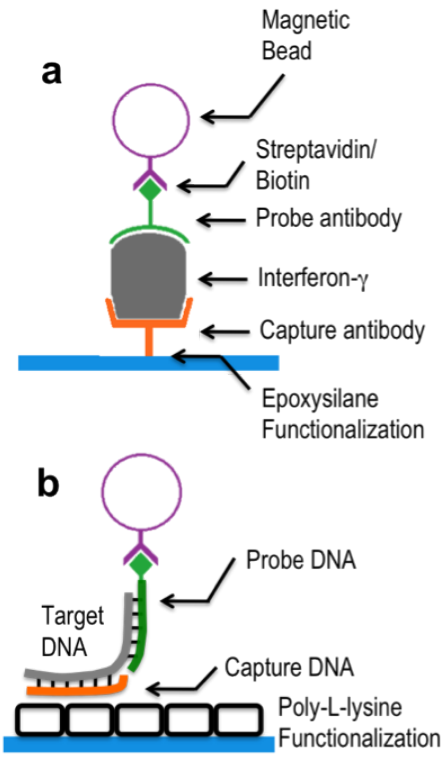

Figure 2.3: (a) Sandwich Assay for IFN-γ. Surface functionalization consists of an epoxysilane group to covalenetly attach the capture antibody. The probe antibody binds to a separate epitope of IFN-γ. The magnetic bead attaches to the probe antibody through a streptavidin-biotin attachment. (b) Sandwich Assay for DNA oligo. A capture DNA strand complementary to a portion of the oligo strand is attaches to the PLL surface through electrostatic adsorption. The probe DNA strand is complementary to a second portion of the target strand and attaches to the bead through a streptavidin/biotin attachment.

2.1.3 Easy-to-use Open Well Cartridge

The core of our user-friendly interface is allowing for the sample and reagents to be loaded into a single open reaction well. We have previously demonstrated a microfluidic platform for DNA binding [24]. However, the requirement for external pneumatic pressure control is restrictive to a POC solution. Therefore, a well-based design was incorporated to allow the DNA assay to be conducted by simply filling and emptying the cartridge. Filling the cartridge consisted of pipetting solution into the cartridge. The foundation of our cartridge is a chip carrier that can be plugged into a socket on our reader. The IC biosensor chip is attached to the surface of the cartridge using a conductive silver epoxy (MG Chemicals, Burlington, Ontario, Canada). Next, our chip surface is functionalized for capture probe attachment. The capture probe and negative control (NC) are printed onto each of our sensor surfaces using a contact pin based printer (Fig. 2.1). After printing, the IC chip is electrically connected to the chip carrier by wirebonding from electronic pads to the chip carrier leads. To provide structural support and waterproofing for the wirebonds, a two-part

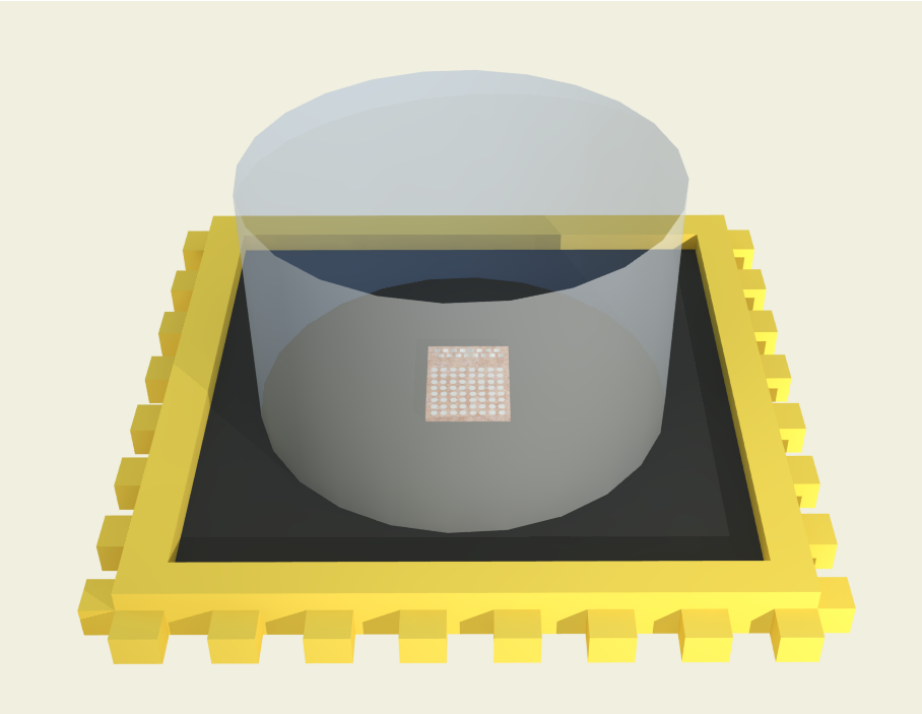

Figure 2.4: A low-cost, disposable cartridge is designed to house the sensor array. It consists of a chip carrier used to enable plug-and-play feature inside the reader. The sensory array is electrically connected to the carrier and a well is formed above the carrier.

epoxy is applied to the wirebonds. The surface is heated to 80°C for 10 min before epoxy application to remove adsorbed water and ensure a good seal [71]. Finally, the polypropylene housing is epoxied to the chip carrier to form the open well. After fabrication, the cartridge can be stored in 4°C storage until the assay needs to be performed.

2.1.4 Magnetic Freezing

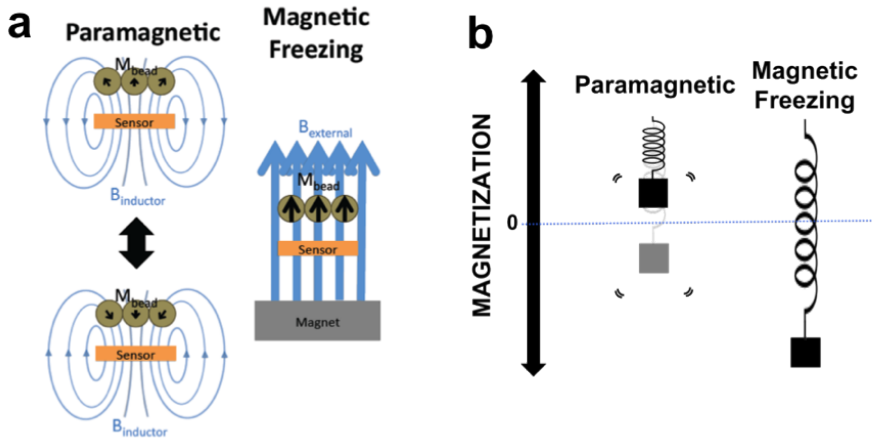

Figure 2.5: (a) The Magnetic Freezing Effect is analogous to (b) an oscillating mass. In a paramagnetic state, the magnetizations of the beads (M_{bead}) are allowed to oscillate up and down. When the small external magnet is applied, the magnetization saturates. The saturation prevents the oscillation of the beads' internal magnetization and no longer contributes to the inductance change of the frequency shift sensor.

2.1.5 Surface Chemistry of Integrated Circuits (IC) for Biological Samples

A key component of constructing the cartridge is the functionalization of the IC chip's silicon nitride surface. Although silicon nitride's non-reactivity serves as a great passivation layer for the IC chip, it presents a challenge to functionalizing the surface. In order to attach molecules to this inactive surface, a 2 μm layer of glass was deposited to the surface using a plasma-enhanced chemical vapor deposition (CVD). The deposition also reduces surface roughness. Our surface functionalization allows capture DNA strands or antibodies to bind to the surface of the chip. Various other functionalizations were evaluated to have lower binding density and uniformity. The protocols are detailed in the Appendix.

Different functionalizations were used to prepare the silicon chip for either DNA capture strand or capture antibody attachment. Several attachment chemistries for antibody and nucleic acid attachment are commonly used for microarray applications including hydroxyl, poly-L-lysine (PLL), amine, aldehyde, and epoxy coatings. The protocol was modified from existing microarray protocols [72–78]. For DNA attachment, a PLL surface is used to allow for the electrostatic adsorption of DNA. Of these coatings, the amine coating of the PLL surface has the highest binding density, sensitivity, and uniformity. To deposit the PLL layer, first, the chip was plasma etched for 1 min to increase reactivity of deposited glass to increase PLL density. Next, the chip was incubated for 30 min in a PLL solution consisting of 37.5 ml nanopure water, 10.1ml filtered 1X PBS, and 8.8 ml PLL from Sigma-Aldrich (St. Louis, MO). The functionalized chip is then stored in a desiccator and allowed to sit for 2 weeks to cure the poly-L-lysine, thus increasing hydrophobicity.

For antibody attachment, an epoxy surface was prepared to allow for covalent attachment to the capture antibody. The chip was immersed for 10 min in 3M H_2SO_4 followed by 10 min of 3M HCl. Immediately after, it was rinsed with water and dried with compressed nitrogen gas [76]. The chip was immersed in 2% (3-Glycidyloxypropyl) trimethoxysilane (Sigma, Aldrich) in 95% ethanol for 15 min. Then it was rinsed with ethanol to remove unbound epoxide groups. The chip was then dried with nitrogen and baked at 110°C for 15 min for covalent attachment of silane groups to the glass substrate [50].

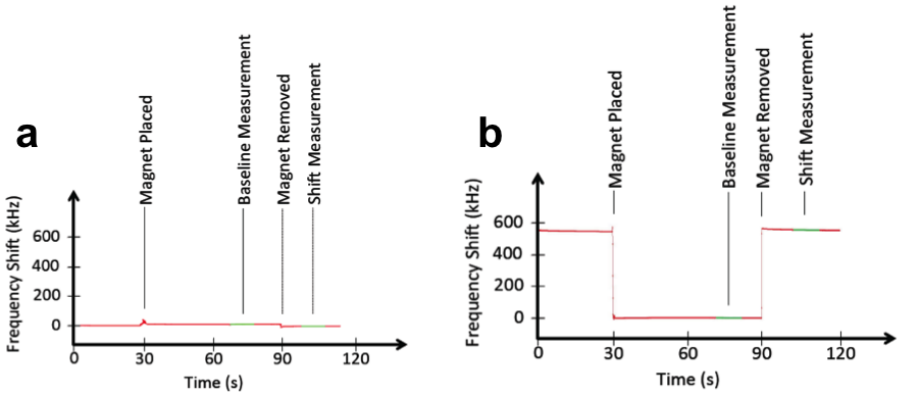

Figure 2.6: Magnetic Freezing. To illustrate the effect of magnetic freezing, a sensor with beads (a) and without beads (b) is measured over a much longer time period than typical data acquisition. After the magnet is placed under or removed from the sensor, an immediate shift in frequency occurs. This difference in frequency shift is used to quantify magnetic beads over the sensor.

2.1.6 Probe Printing

After creating a chemically reactive surface on our IC chip, we need to print experiment-specific attachment probes to our sensor surface. For the DNA sandwich assay, synthetic oligo probe strands (IDT, Skokie, IL) were used for attachment to the PLL surface. The probes were printed onto the chip surface using the SpotBot 2 contact pin based microarray printer (Arrayit, Sunnyvale, CA) (Fig. 2.7). The print solution was composed of 10 μl of 2X microspotting solution (Arrayit, Sunnyvale, CA) with 10 μl of 50 μM probe DNA . The chip was then allowed to dry overnight in a desiccator. Next, the chip was baked at 80°C for 80 min to further dry the chip and enhance DNA binding. Following printing and drying, the chip was placed in a container with BlockIt Plus Microarray Blocking Buffer (Arrayit, Sunnyvale, CA) and placed on an orbital shaker for 1 hr at 100 rpm. Finally, the chip was lightly rinsed for 30 s in nanopure water and spun dry.

For the Immunoassay, antibodies were printed using the SpotBot 2 microarray printer at room temperature. Humidity level was maintained between 50-55%. Print solution was prepared by mixing 10 μl stock solution of antibodies with 10 μl of protein printing buffer (ArrayIt, Sunnyvale, CA). Protein solution buildup in the pin reduced the uniformity of the printed spots on the sensors.

Thus, the pin was routinely cleaned prior to printing by sonication in 50mM KOH from 10 min to 1 h [79]. After printing every 10 spots, the pin was sonicated for 10 min in distilled H_2O, ArrayIt light pin cleaning protocol [80]. After printing antibodies on the sensors, the chip was left in the desiccator to dry overnight.

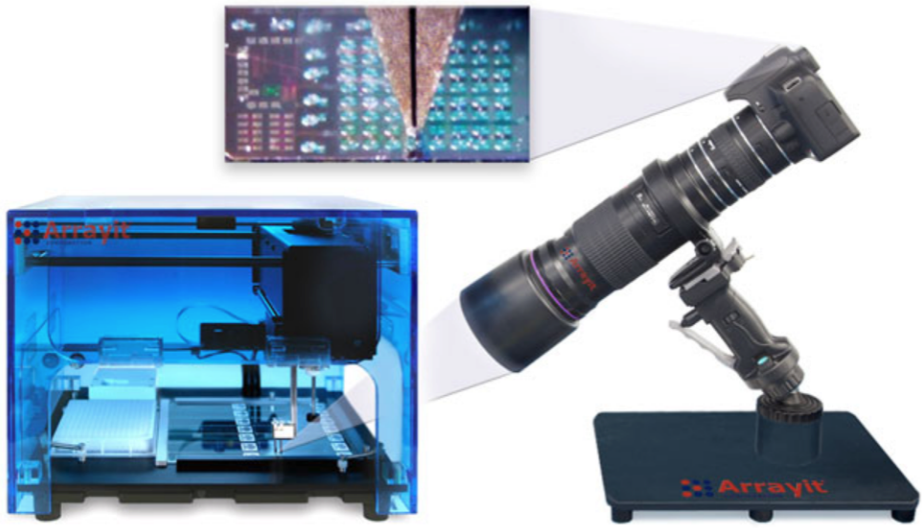

Figure 2.7: A microarray printer is modified to align print spots on the surface of the sensors.

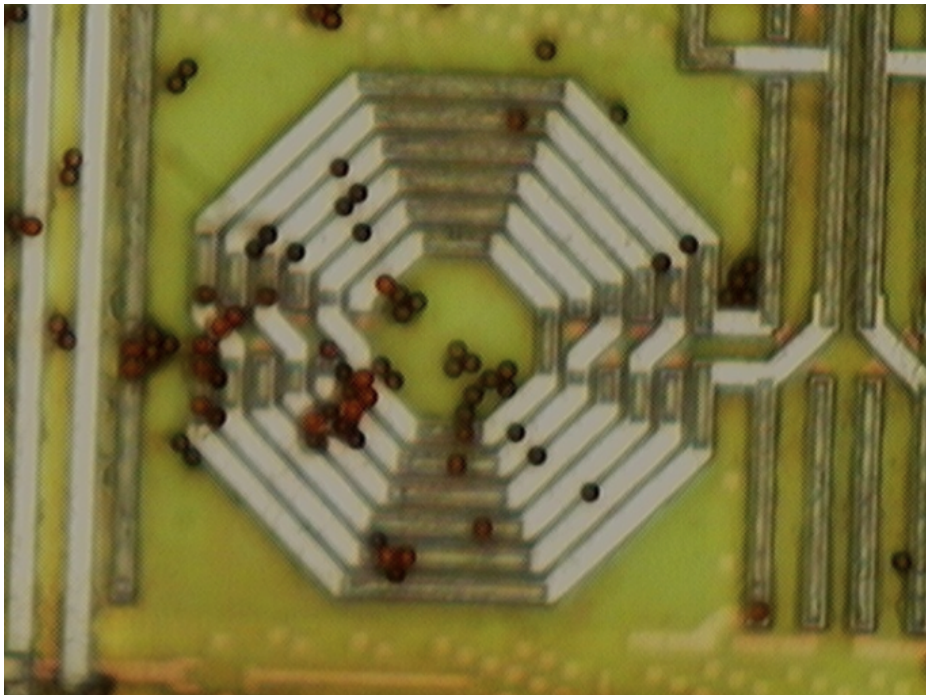

Figure 2.8: A distribution of 4.4μm beads over the sensor surface.

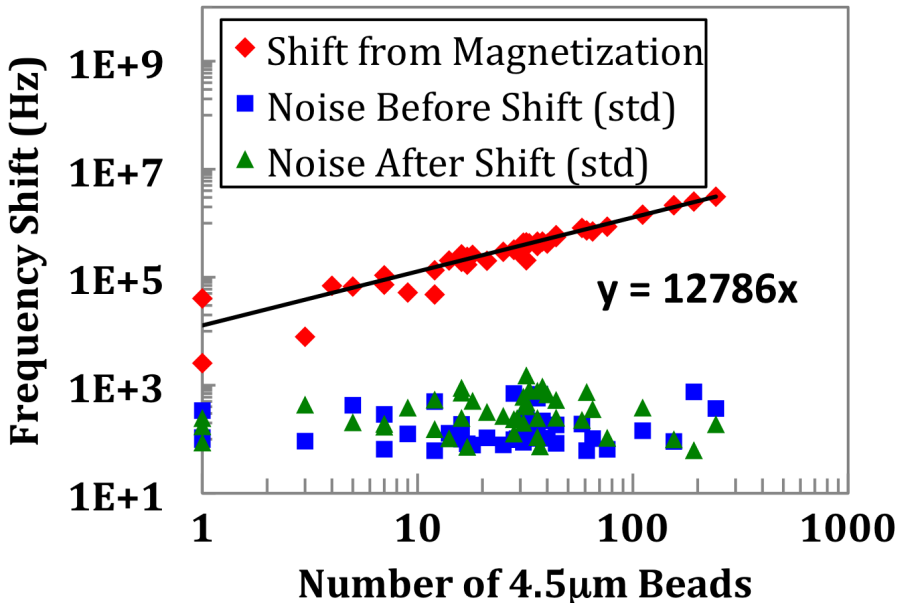

Figure 2.9: Magnetic Freezing Quantification of 4.5 μm beads. The average frequency shift for each 4.5 μm bead is 12.8 kHz. The coefficient of determination, R2, was greater than 0.99.

2.1.7 DNA Protocol

After probe printing, the chip can be stored until a sample is ready to be tested. To test the viability of the instrument for the quantification of unique DNA targets, we employed a sandwich assay consisting of a capture (5'-TTT TTC TGG TTG GGT TGA TTG GAT TTA GCT TGG C-3'), target (5'-ATC CAA TCA ACC CAA CAA TAT TGA TAA GGA T-3'), and a biotinylated probe strand (5'-Biotin-ATC CTT ATC AAT ATT-3') for indirectly labeled detection. A non-complementary NC capture strand (5'-ATG CGA AAC GAT CCT CAT CCT GTC TCT TGA-3') is also printed to test cross binding.

The hybridization assay took place within the open well. Emptying the well consisted of gently inverting the well. Buffers used in the assay were a hybridization buffer (1X PBS, 1mg/mL BSA, 5nM EDTA, 0.1% Tween-20, 0.1mg/mL salmon sperm DNA), a Bead Binding and Washing Buffer (5mM Tris-HCl pH 7.5, 0.5mM EDTA, 1M NaCl), Stringent Wash Buffer 1 (Arrayit, Sunnyvale, CA), and Stringent Wash Buffer 2 (Arrayit, Sunnyvale, CA). First, the dry well was washed 3 times with Hybridization Buffer. Next, a hybridization solution containing varying concentrations of target DNA and 1 μM biotin labeled probe DNA was prepared. A total of 200 μl of hybridization solution was added to the well and allowed to incubate at room temperature for 30 min. During hybridization, a solution of streptavidin conjugated 1μm diameter super-paramagnetic beads was prepared. Ten μl of 10 mg/ml Dynabeads MyOne Streptavidin C1 (Invitrogen, Carlsbad, CA) was washed and resuspended 3 times in 100 μl of Binding and Washing Buffer per the manufacturer's

protocol [81]. After DNA incubation, the well was rinsed twice each in DNA Stringent Wash Buffer 1 and 2 (Arrayit, Sunnyvale, CA) for 2.5 min at a time. The well was then rinsed 3 times in Binding and Washing Buffer. The bead solution was added and allowed to bind for 20 min. Lastly, the well was washed another 3 times with Binding and Washing Buffer, then washed 3 times with nanopure water, and then emptied. A more detailed protocol can be found in the Appendix section "Detailed DNA Functionalization of IC."

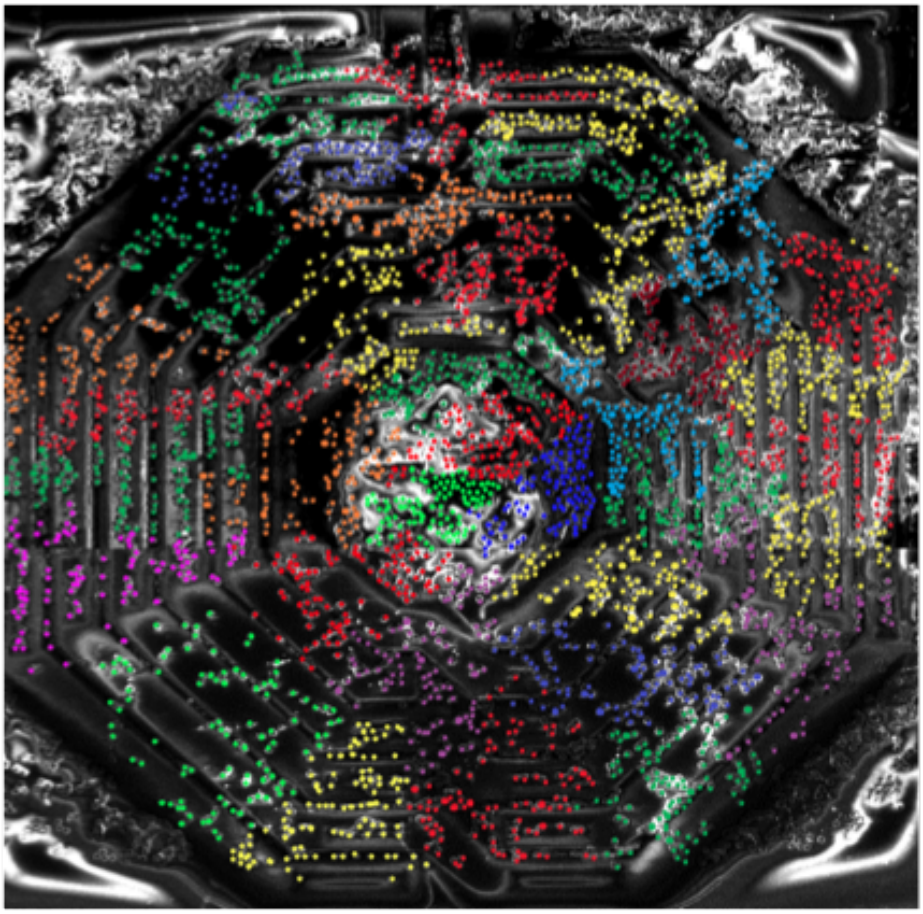

Figure 2.10: Scanning electron microscope image of beads over our sensor. These beads were counted and compared with measured signal. Each contiguous colored group represents 100 beads.

2.1.8 Immunoassay Protocol

IFN-γ and Granulocyte-macrophage colony-stimulating factor (GM-CSF) ELISA MAX Standard kits were obtained from Biolegend (San Diego, CA). IFN-γ capture antibodies were used for the primary assay. GM-CSF capture antibodies were used as negative control. Assay dilutent (1% BSA in PBS) was prepared prior to use. Lyophilized IFN-γ protein was reconstituted in assay dilutent and stored in a -80°C freezer in polypropylene vials. The chip was removed from the desiccator and blocked for 1 h in 500 μl of BlockIt Plus solution (ArrayIt, Sunnyvale, CA) in an orbital shaker at

125rpm. Afterwards, the chip was rinsed 5 times with 400 μl of Wash Buffer (0.05% Tween-20 in PBS) to remove the blocking solution. The IFN-γ stock solution was thawed and diluted to the target concentration. A total of 100 μl of protein solution was added to the well and incubated for 2 h at room temperature with shaking at 125rpm. The well was rinsed 5 times with 400 μl of wash buffer to remove unbound proteins. IFN-γ detection antibody (200X dilution of stock solution in assay diluent) was added to the well and incubated for 1 h at room temperature with shaking at 125rpm. Unbound capture antibodies were washed 5 times with 400 μl of wash buffer. A total of 5 μl of 1 μm diameter Dynabeads MyOne Streptavidin C1 coated magnetic beads was washed 3 times with PBS to remove preservatives from the bead solution [81]. The beads were then resuspended in 100 μl of PBS. Afterwards, the bead solution was added to the well and was incubated for 20 min with no agitation. After incubation, 5 μl of 25% Glutaraldehyde solution (Sigma-Aldrich, St. Louis, MO) was added to the well for fixation [82]. After a 10 min incubation, the well was rinsed 5 times with wash buffer. Finally, the well was rinsed 5 times with water to prevent crystallization of remaining salt solution on the chip. The chips were left to dry for measurement.

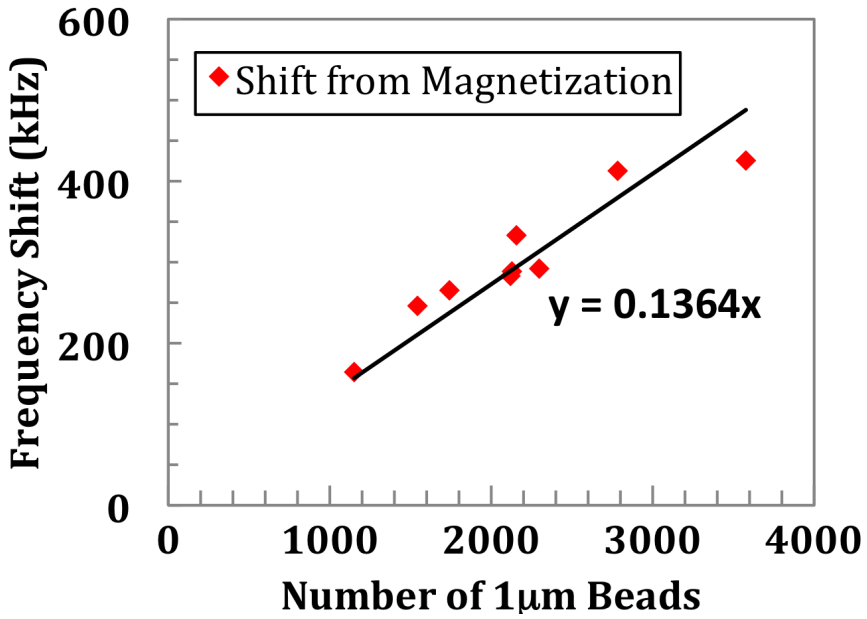

Figure 2.11: Magnetic Freezing Quantification of 1 μm beads. These beads were used in the DNA assay and immunoassay. The average frequency shift for each 1 μm bead is 136 Hz.

2.1.9 Measurement and Processing

Following the hybridization assay, the chip can be measured while immersed in solution or dry. If allowed to dry, the chip could be measured months after the hybridization assay with less than 1% change in measurements. The reader is connected to an external laptop and a graphical user interface is initiated. Measurement consists of two cycles of measurements. The time to obtain a

single measurement is 100 ms for a combined reference and sensor measurement. During a cycle, each sensor is measured for 5 s for a total of 50 measurements per sensor. All measurements had a standard deviation of less than 20 Hz. Between 1-48 sensor sites can be measured, within up to 4 min for all 48. One cycle of measurements establishes the baseline frequency in the presence of a small rare-earth magnet. Next, the magnet is removed from the PCB. During the next cycle of measurements, the endpoint frequency measurement is obtained.

The difference between the baseline measurement and the endpoint measurement is used to infer the number of beads over the sensor. More bead binding implies a higher concentration of target analyte. A graphical user interface is used to acquire the data and initiate function (Fig. 2.12).

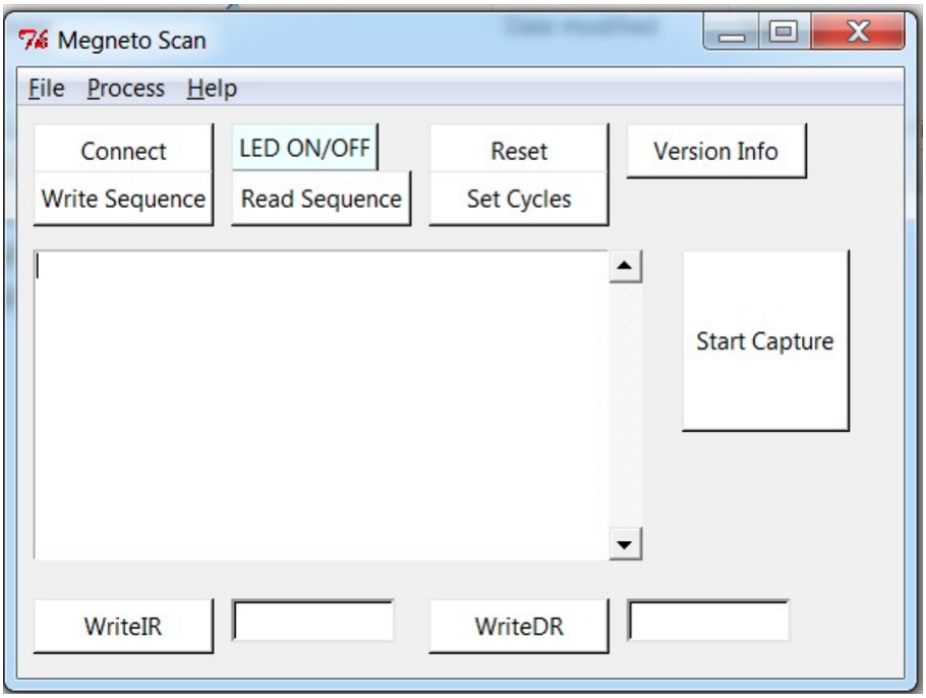

Figure 2.12: DNA Quantification. In the DNA assay, target concentrations can be detected from 100 pM to 10 nM. At the limit of detection, 100 pM, the frequency shift from the target sensor is over two times the shift from a non-complementary NC sensor.

2.1.10 DNA Sandwich Assay

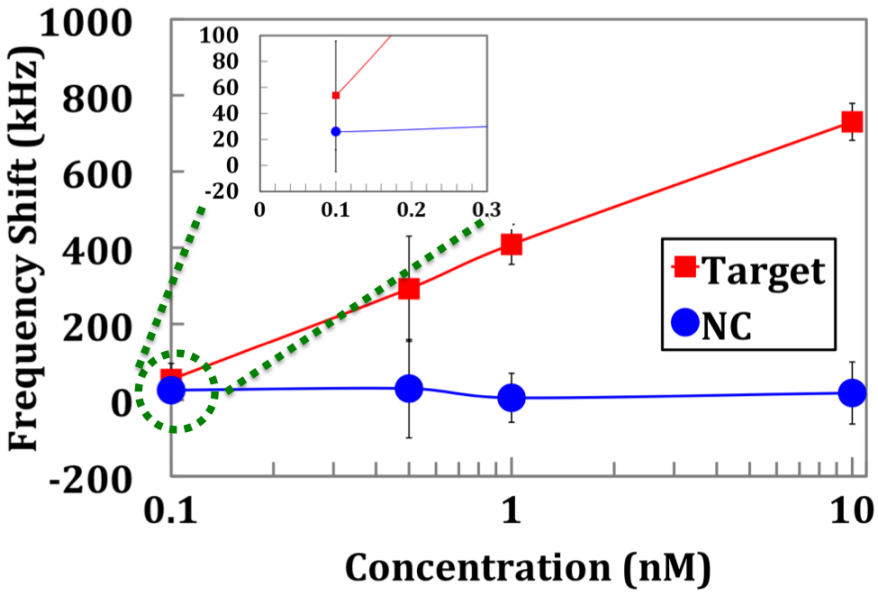

Figure 2.13: DNA Quantification. In the DNA assay, target concentrations can be detected from 100 pM to 10 nM. At the limit of detection, 100pM, the frequency shift from the target sensor is over two times the shift from a non-complementary NC sensor.

2.1.11 Data Processing

The simple processing scheme obviates the need for high computational power or filtering schemes. A simple arithmetic division is the heart of the signal processing. The presence of magnetic beads leads to a shift in the resonant frequency. The resonant frequency is determined directly from the number of periods over the measurement time. Optimal counting intervals have been previously explored [25].

Magnetic freezing is a novel technique that adds functionality to and improves performance in frequency-shift based magnetic biosensors. We previously demonstrated the large linear dynamic range of the sensor to magnetic beads as well as single bead sensitivity [24]. Techniques such as incorporating a reference sensor and a correlated double counting scheme reduced a very large fraction of frequency drift. Traditionally, a frequency-shift oscillator based magnetic biosensor without magnetic freezing requires approximately 30 min of warm up time for the oscillator to become stable. Moreover, frequency drift in oscillators compounds this problem by increasing the noise of the sensor. In the previous detection scheme, sensitivity of the biosensor was determined by the immediate presence or absence of magnetic beads over the sensor. This would obviate long-term frequency drift by obtaining frequency shift measurements immediately after the baseline measurement. However, this is not compatible with a typical biological assay. In a biological assay, the baseline measurement would need to be acquired before the entire assay, with the final measurement needing to be taken at the conclusion of the assay. This would allow significant oscillator drift to accumulate, thus

significantly decreasing sensitivity. In addition to the requirement that the biosensor would need to stay on during the entire assay, the system would be incapable of conducting measurements over multiple sensors because only one sensor could be maintained active during the assay.

Magnetic freezing solves all these issues (elimination of warm up, removal of active requirement of the system during assay, elimination of baseline measurement before assay, inability to obtain measurements from multiple sensors) by requiring only one set of measurements at the conclusion of the assay. This is accomplished by first measuring the sensor at the end of the assay using the previously described frequency shift technique, as seen in Fig. 2.5. In an unfrozen state, the beads are able to track the magnetization induced by the inductor. Next, an external magnet is used to saturate the magnetization of the bead. This holds the magnetization to a point of saturation. The magnetic field of the inductor cannot modulate the magnetization vector of the beads due to the magnetic saturation of the beads. Thus, the beads have no significant effect on the inductance. A small (9.5mm x 9.5mm x9.5mm) neodymium magnet with a surface field of 0.5T is used to saturate magnetization. By having magnetization saturated, the magnetic domains inside the bead are not allowed to track the 1GHz oscillation frequency of the inductor. This prevents the beads from increasing inductance and lowering the resonant frequency of the electrical oscillator.

To examine the effect of magnetic freezing, an experiment was conducted by randomly distributing between 1-250 4.5 μm diameter beads (for ease of counting) over the sensor surface. An external magnet was attached and removed from underneath the sensor. For demonstration of the magnetic freezing effect, a sensor is measured continuously for 120 s. At t=30 s, the small magnet is placed underneath the sensor and PCB (Fig. 2.6). The shift in frequency is immediate, limited only by how quickly one can place the magnet. The baseline measurement is taken by calculating the mode of frequency shift over a few seconds. The noise before the shift is calculated by computing the standard deviation of the data. After removing the magnet at t=60 s, the mode and standard deviation is again calculated over a period of a few seconds. This experiment was repeated for all 48 sensors and the results are shown in Fig. 2.9 and Fig. 2.8. An average frequency shift of 12.8 kHz per bead was measured. A shift was detected for a quantity of beads between 1-250. The limit of detection can be seen to be a single bead. The sensor did not show any signs of saturation. Experimental data and electromagnetic simulation revealed that the sensor could have beads stacked up to 40 μm above the sensor surface before saturating (Fig. 2.20). For biological studies, paramagnetic beads of 1 μm diameter were used for the protein and nucleic acid assays. To quantify the beads, sensors were imaged using a scanning electron microscope. The number of beads over the sensor were counted (Fig. 2.10) and compared with measured signal. The quantification of these beads is shown in Fig. 2.11.

An important trend in biotechnology is the emergence of nucleic acid testing (NAT) [22]. Areas with the printed capture strand would result in beads binding to the sensor surface, as seen in Fig. 1c.

Conc. (nM)	Conc. (pg/mL)	Exp. Freq. Shift (kHz)	NC Freq. Shift (kHz)
10	5000	730	18
1	500	409	6
0.5	250	293	30
0.1	50	54	26

Table 2.1: Frequency-shift measurements versus frequency for the DNA assay.

Reference sensors and sensors printed with the NC capture strand would exhibit some fluctuations in frequency shift measurements due to variations in background bead binding to the chip. However, the NC sensors did not appear to have a different level of binding than the background binding level, indicating little or no cross binding of the sandwich assay.

Quantifiable target DNA concentrations could be detected over two orders of magnitude (Fig. 2.13 and Table 2.1). The limit of detection for the sensor was 100 pM, where the frequency shift was more than two times the background level. The sensor reached a saturation level at 10 nM. Although this sensitivity is less than traditional amplification-based technologies, this device did not depend on the stringent heating/cooling cycles of amplification technologies. This allows for a simpler, more reliable detection system.

2.1.12 Immunoassay detection of Tuberculosis biomarker IFN-γ

Although NAT testing has demonstrated significant progress in diagnostics, a more diverse variety of biomarkers can be detected with traditional immunoassay. To test the biological impact of the sensor, the TB biomarker IFN-γ was detected as well as its cross-binding with a GM-CSF capture antibody. Compared with the DNA assay, the immunoassay had a higher level of background binding and variability. The results of the immunoassay are shown in Fig. 2.14 and Table 2.2. The minimum detectable concentration of protein was 1 pM. The sensor saturated at approximately 30 pM. Two additional concentrations were measured outside of the quantifiable range of the ELISA kit: 60 pM and 150 pM. It is important to note that even though a single antigen was detected using a standard sandwich ELISA kit, the IC surface chemistry and detection system are compatible with any other sandwich immunoassay.

2.1.13 Cartridge Variability

A reliable diagnostic should yield the same measurements for the same target concentration. Various sources of variability affect overall cartridge variability: electronic chip-to-chip variability, capture strand/antibody print alignment, and biological assay variability. All three of these variability sources contributed to the overall DNA assay and immunoassay quantification variability. Due to

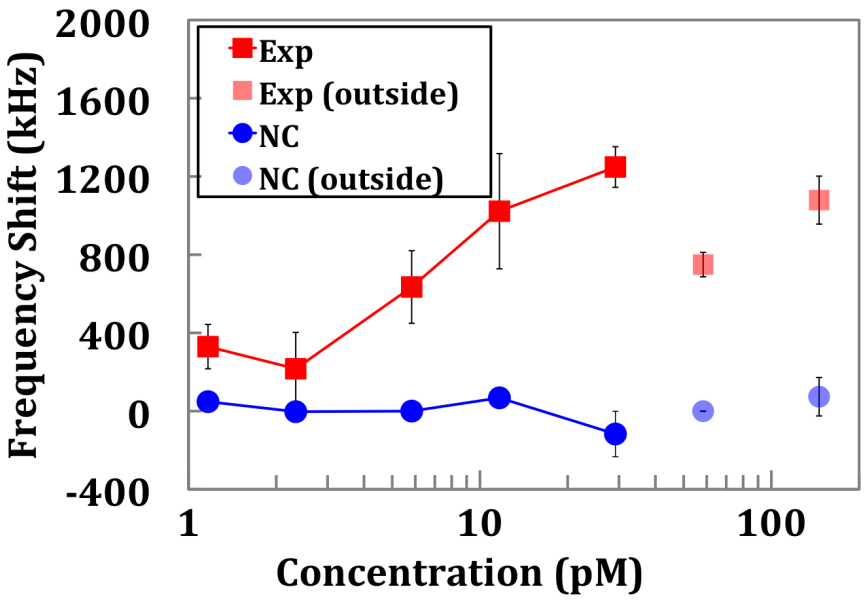

Figure 2.14: Immunoassay Quantification. The limit of detection for IFN-γ was approximately 1pM. The sensor surface was saturated with beads at 30 pM. The negative control (NC) consisted of sensors sites printed with an antibody specific to Granulocyte-macrophage colony-stimulating factor (GM-CSF). Two additional concentrations were tested at 60 pM and 150 pM. However, these concentrations were outside the quantifiable range of the ELISA kit and therefore not as reliable.

the nature of contact printing, variations in spot printing could be misaligned by as much as 50 μm. This misaligns capture molecules over the sensor and thus reduces the number of magnetic beads detected. This leads to an underestimation of target molecules.

In order to quantify chip-to-chip variability, the same number of beads must be measured across multiple cartridges. A total of eight separate cartridges were measured. First, cartridges were measured with no beads present. This leads to a standard deviation of less than 4kHz, or the equivalent of less than 30 beads.

Next, we attempt to place a constant number of beads on the same sensor of the eight cartridges. The tip of a wooden probe is coated with a solution of 1 μm magnetic beads, and subsequently, a thin

Conc. (pM)	Conc. (pg/mL)	Exp. Freq. Shift (kHz)	NC Freq. Shift (kHz)
150	2500	1080	74
60	1000	740	30
30	500	1250	-117
10	200	1020	68
6	100	630	0
2	40	220	-3
1	20	330	48

Table 2.2: Frequency-shift measurements versus frequency for the immunoassay.

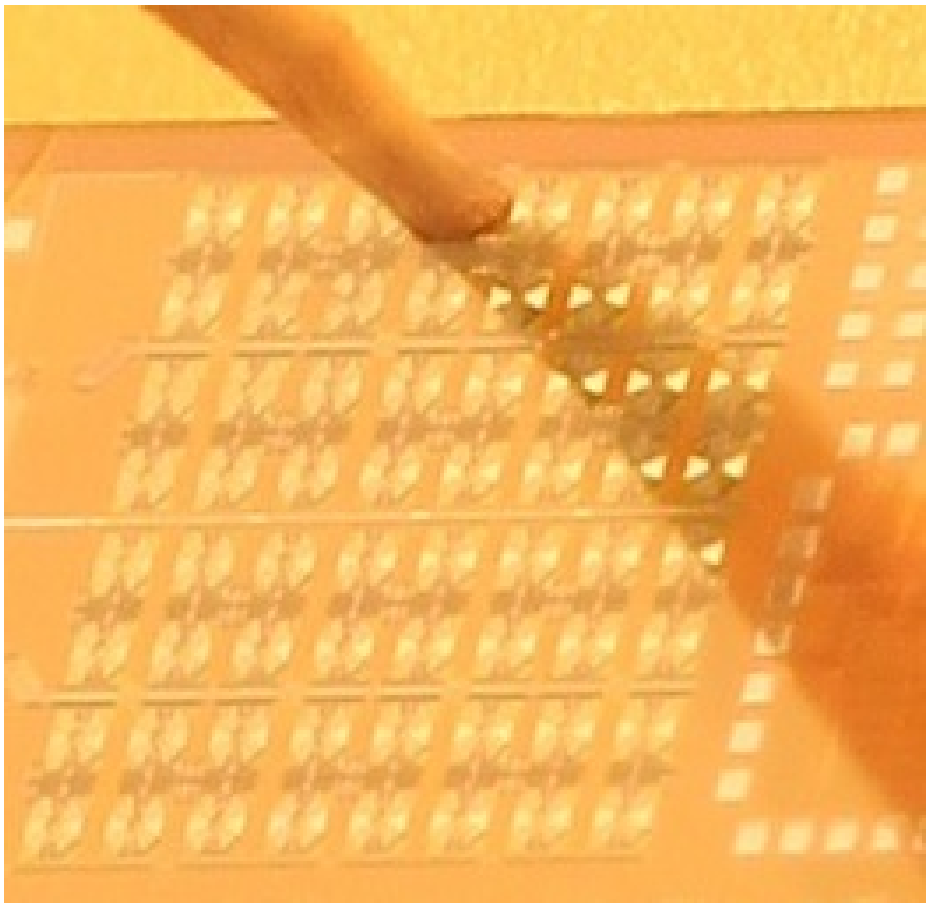

Figure 2.15: In order to isolate each cartridge's variability in quantifying beads, it is necessary to ensure each cartridge measures the same quantity of beads. A distribution of beads is fixed to the tip of a non-magnetic wooden probe using a synthetic polymer resin. The probe is visually aligned to a sensor on each cartridge and frequency shift measurements are obtained.

layer of synthetic polymer (Sally Hansen, New York, NY) to permanently attach the beads. Both the wooden probe and nail polish have a negligible effect on the sensor because they are non-conductive and nonmagnetic. The probe is visually aligned to the surface of the sensor for each cartridge and measured (Fig. 2.15). The results of the cartridge-to-cartridge variability are shown in Fig. 2.16. The standard deviation of the probe measurements is significantly higher than those of blank cartridge measurements. However, the standard deviation of the probe measurements is approximately 10% of the overall signal. This corresponds to approximately 10 μm of probe misalignment for our 120 μm diameter sensor. Thus, the variation is likely due to probe misalignment.

2.1.14 Limitations of dB/dz for Label-free Detection of Nucleic Acids

A general method for the label-free detection of a nucleic acids is proposed 2.17.A hybridization event results in the label having an average position closer to the sensor surface. The scheme depends on the ability for the sensor to discriminate how closely the label travels near the sensor surface.

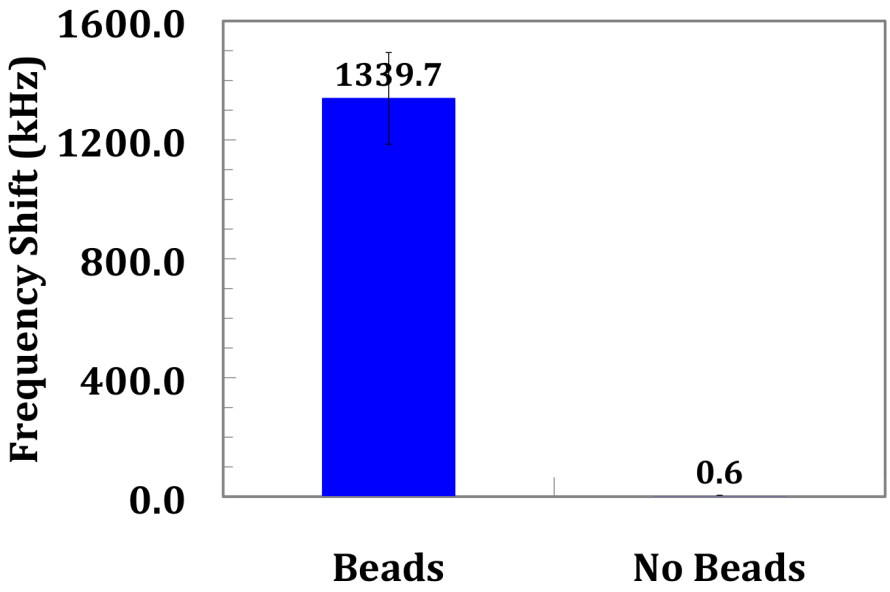

Figure 2.16: Cartridge-to-Cartridge Variability. An important metric of a diagnostic is its ability to reproducibly detect the presence of a fixed number of target molecules. To emulate a fixed number of target molecules, the average frequency shift of eight cartridges are measured with similar numbers of magnetic beads. First, the cartridges' variability is measured with no beads present. A standard deviation of 4 kHz was measured. Next, a probe with a fixed number of beads was measured on each sensor. A standard deviation of 150 kHz, or 10% of the overall signal was measured. This is likely due to probe-sensor misalignment.

Figure 2.17: Method for the label-free detection of nucleic acids.

Although this detection method could be extremely useful because of the elimination of the need for labeling, this detection scheme is difficult to realize in frequency-shift oscillator-based biosensors. The detection scheme relies on the ability to discriminate proximity changes of the magnetic label to the sensor surface.

An experiment is conducted to measure the vertical sensitivity of a frequency-shift biosensor to vertical displacement of magnetic particles. The tip of a non-magnetic wooden probe was coated

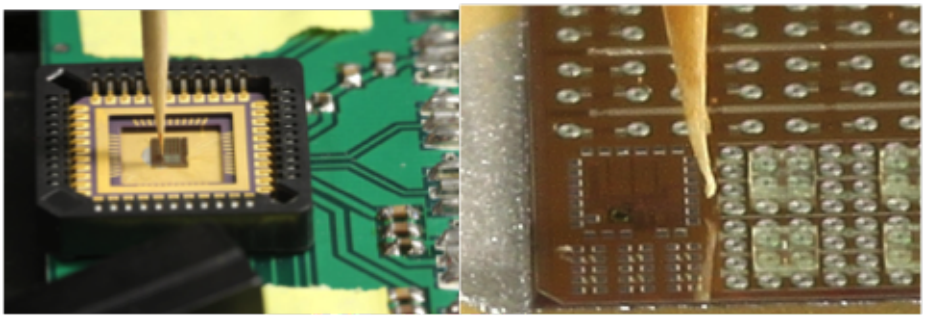

Figure 2.18: To test the vertical sensitivity of the sensors to beads, a toothpick containing beads on the tip was moved at varying positions above the sensor using a micrometer. As a control, a toothpick without beads was measured at the same heights.

with superparamagnetic particles (Fig. 2.15). The probe was positioned above the sensor surface using a micrometer positioner. The sensor is measured at various displacements above the sensor surface. Additionally, electromagnetic simulations are conducted to estimate the vertical sensitivity of the biosensor (Fig. 2.19). The results of the experiment and simulation are plotted in Fig. 2.20, showing positive agreement.

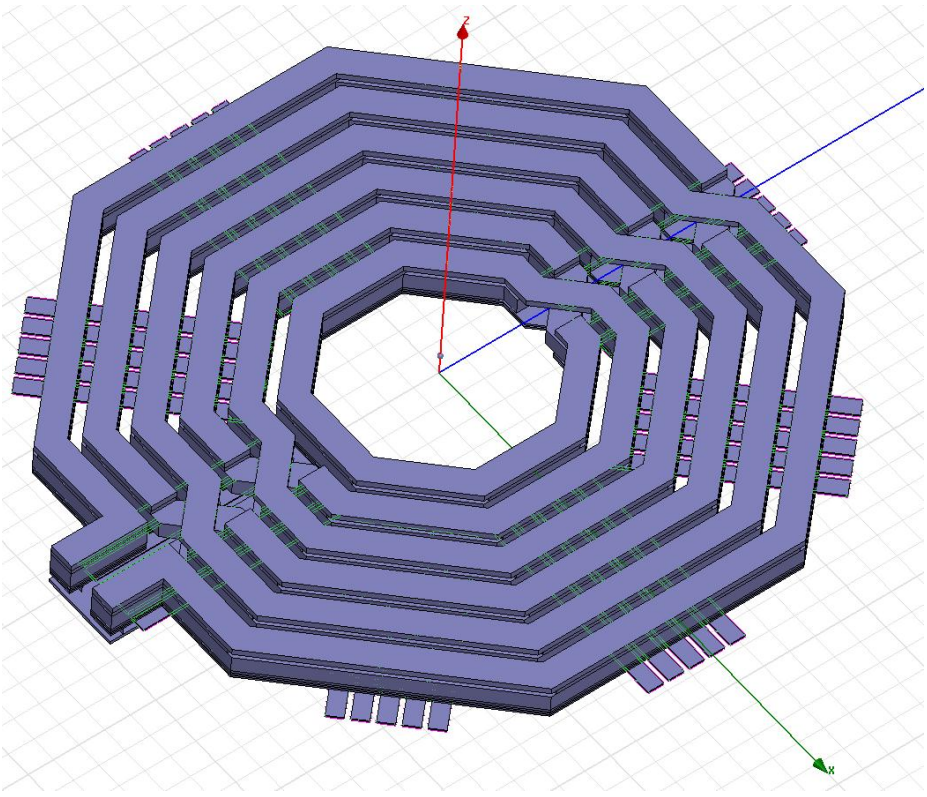

Figure 2.19: Additionally, an electromagnetic simulation was used to determine the vertical sensitivity of the sensor to magnetic beads.

It can be seen that the sensor has a "volume" of detection of approximately 40μm above the

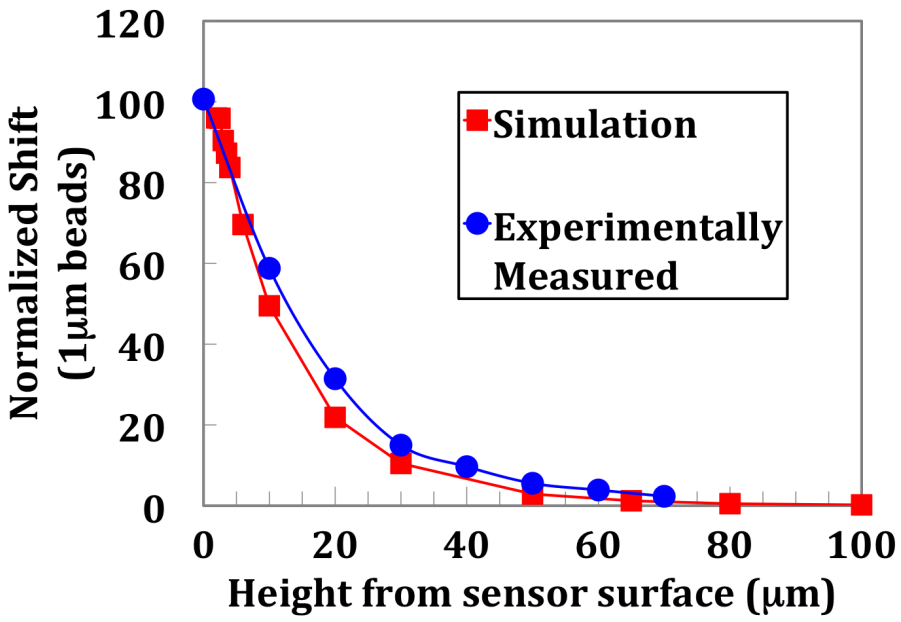

Figure 2.20: The results of the simulation and experiment reveal a 10%, 50%, and 90% reduction in sensitivity at bead heights 3μm, 13μm, and 40μm above the sensor surface, respectively

sensor surface (Fig. 2.21). However, this displacement would be difficult to realize in the label-free detection scheme because the probe strands would need to be too long (thousands of basepairs long) for detection. Despite this limitation, the volume of sensing can be potentially used to increase the dynamic range and sensitivity of the frequency-shift biosensor by using a composite structure above the sensor surface (such as a porous membrane or cellulose chamber) to enhance the binding of magnetic labels above the sensor.

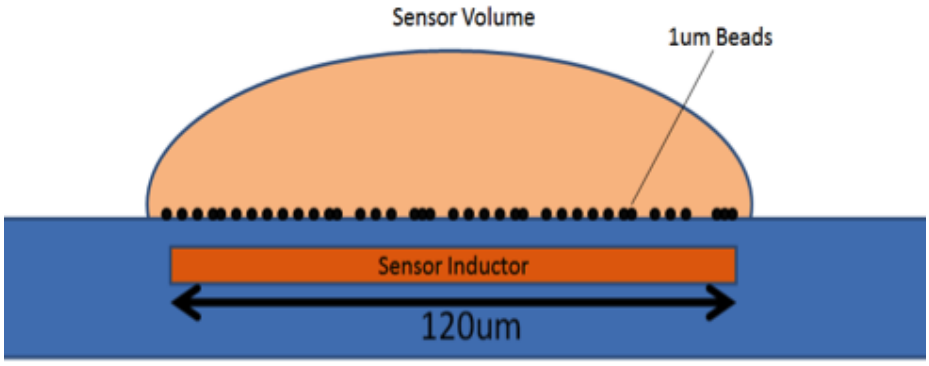

Figure 2.21: Only a fraction of the total sensing volume is used in the surface binding-based approach. Future designs could utilize the full sensor volume and expand the dynamic range of the sensor.

2.1.15 Additional Label-free Detection Schemes

Additional label-free detection schemes are proposed. In a scheme called the "bead release assay," the hybridization of a target nucleic acid strand prevents a secondary labeled probe strand to bind to the primary probe strand (Fig. 2.22). This is similar to a competitive immunoassay. The target strand hybridization must be energetically favorable to the secondary probe strand hybridization. However, if the target strand is not complementary to the primary probe strand, the secondary probe strand is hybridized and the magnetic label binds to the sensor surface. Unlike previous detection schemes, the presence of magnetic labels near the sensor surface is indicative of the lack of target strands in the biosample.

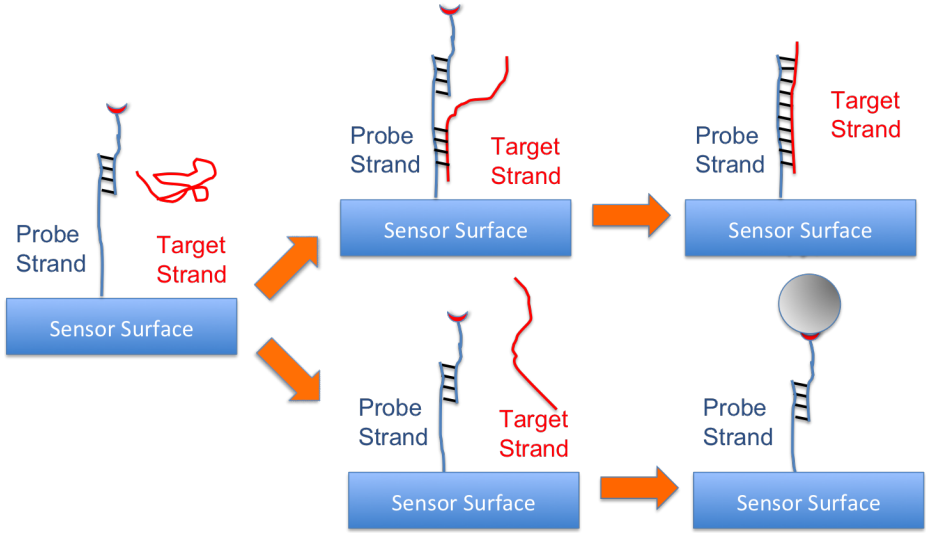

Figure 2.22: Bead release assay. Presence of complementary target strand prevents magnetic labels from binding to the sensor surface.

The energetics of this detection scheme was simulated using a thermodynamic modeler [83]. The primary probe strand (5'-GACTTGCATCA TACTACAACGTCGTCCGTTT AAGGGCCCAGC-TAGGATCA3') and target strand (5' TGATCCTAGC TGGGCCCTTAAACGGACGACGTTGT AGTATGATGCAAGTC-3') dimer was more energetically favorable (-16.35kcal/mol) than the probe strand and secondary probe strand (5'-TGATCCTAGC-3') dimer.

We demonstrate the bead release assay on a glass slide (Fig. 2.23). We also demonstrate the dose response of target strands and the resulting difference in binding level (Fig. 2.24). The limitation of the bead release assay is a low dynamic range.

We propose additional potentially label-free schemes [84]. In Fig. 2.25, a hybridization event results in a change of persistence length of the nucleic acid. This results in discernible aggregate motion of the particle because its positional distribution is changed. In a separate scheme (Fig. 2.26), target strand hybridization results in the opening of a nucleic acid hairpin structure. The

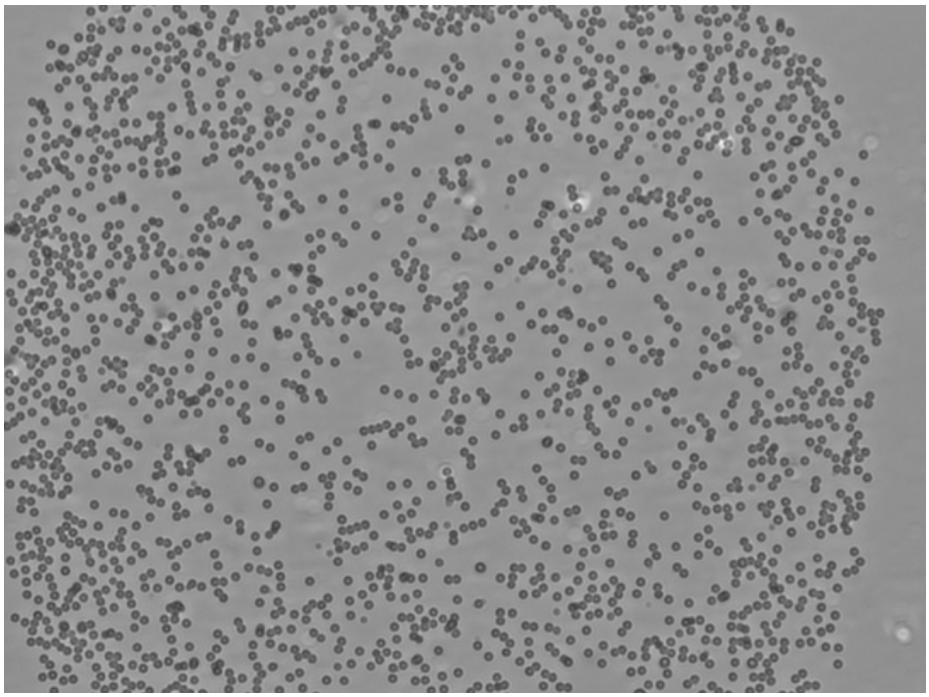

(a)

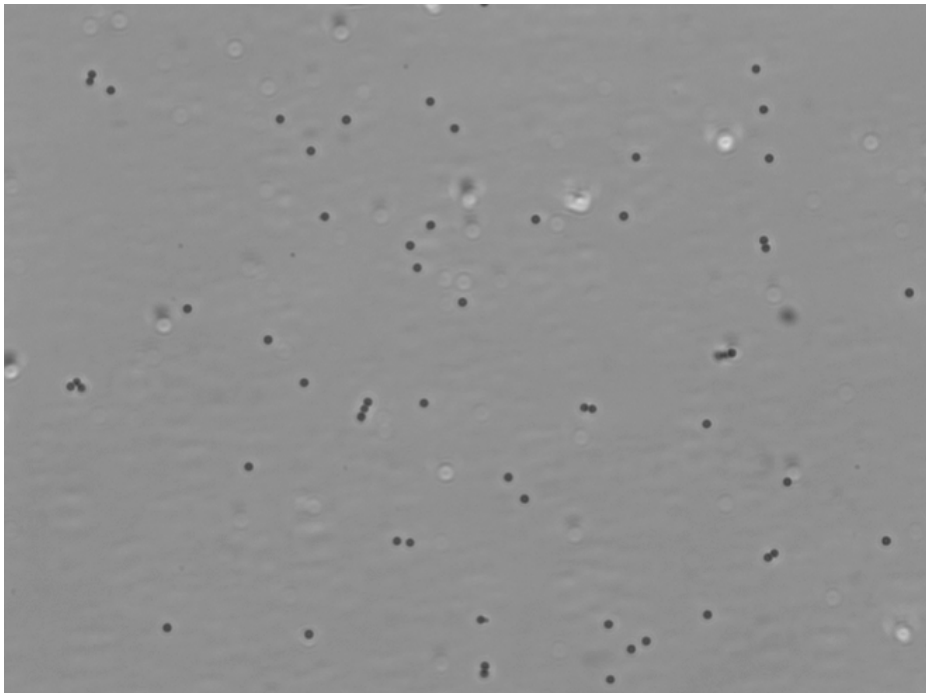

(b)

Figure 2.23: Demonstration of bead release assay for (a) noncomplementary and (b) complementary target.

bead is released from a positional distribution near the sensor surface. In a variation of an earlier label-free sensing scheme, the lateral sensitivity of a sensor is exploited to lead to signal change (Fig.

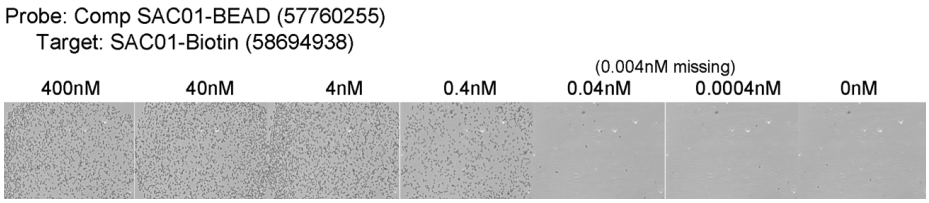

Figure 2.24: Dose response of bead release assay. Results show a steep transition in bead binding from 4 nM to 0.04 nM target concentration.

2.27).

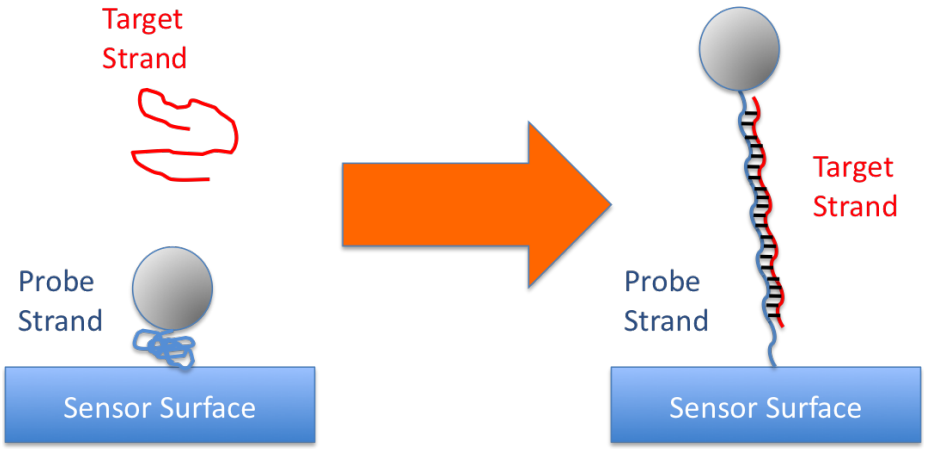

Figure 2.25: Persistence length change of a hybridization event leads to a change in position distribution of the label.

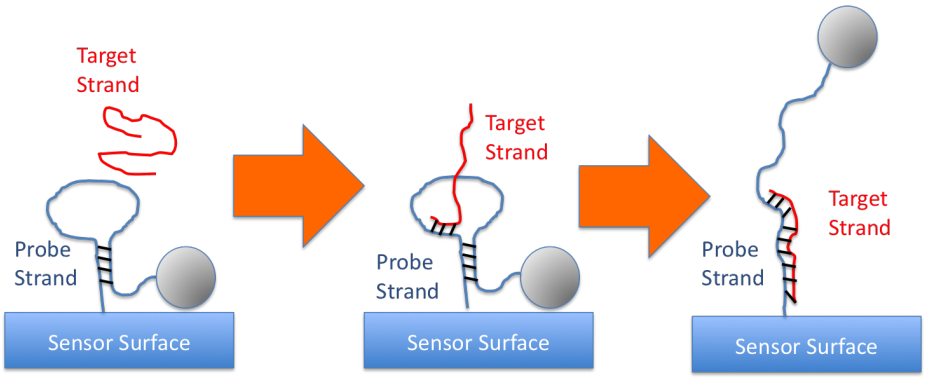

Figure 2.26: Target hybridization leads to the opening of a nucelic acid hairpin structure.

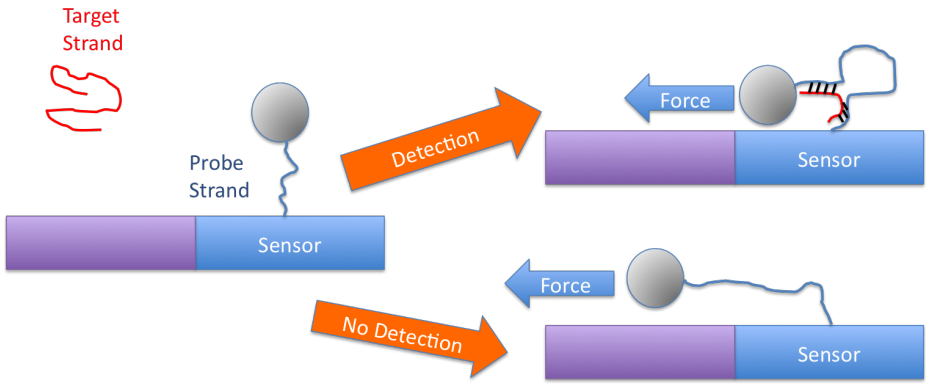

Figure 2.27: An external force (for example flow, gravity, or magnetic) is used to exploit the lateral sensitivity of the sensor and lead to signal change.

2.1.16 Variations of Magnetic Freezing

Magnetic freezing enables the elimination of a baseline measurement before or during the biological assay. In addition, the effect of oscillator frequency drift is significantly reduced. In our previously mentioned magnetic freezing scheme, a small magnet is placed near the center. In a POU diagnostic, this magnet could be integrated into the device lid. The presence of the magnet saturates the superparamagnetic particles and neutralizes their effect on the biosensor. The saturation of the biosensor as a function of magnet displacement is examined. The external magnet is placed above the sensor and its vertical position is varied using a micrometer positioner (Fig. 2.28). The magnet starts at a position a cm above the sensor . Next, the magnet is moved up 10 mm, then returned to its starting position. Subsequently, the magnet is moved up vertically in steps of 3mm, then returned in steps of 3mm. Finally, this process is repeated for steps of 2 mm, and then 1mm. The results of this shift is shown in Fig. 2.29. The saturation profile can be seen from the results.

An alternative saturation and unsaturation could be achieved using a permanent magnet rotated using a small motor without any rotational encoder or positional feedback mechanism (loosening the tolerance requirements of the motor and reducing cost) (Fig. 2.30). The sensor response is shown in Fig. 2.31a. The FFT of the signal is shown in Fig. 2.32a. Low frequency drift in oscillator signal and motor speed drift is filtered using a band pass filter centered on the peak frequency. A script was written to automatically calculate the peak frequency and adjust the bandpass filter. The filtered frequency response is shown in Fig. 2.32b. The filtered signal is shown in Fig. 2.31b. A new signal was constructed using the maximum and minimum values of both the unfiltered and filtered signal (also the amplitude of the signal envelope). The new resulting signal is shown before and after filtering (Fig. 2.33). As can be seen, the noise in the signal is suppressed using filtering.

An alternative to filtering and envelope detection of the motorized magnetic freezing scheme is a method similar to lock-in amplification. A script automatically determines the peak frequency

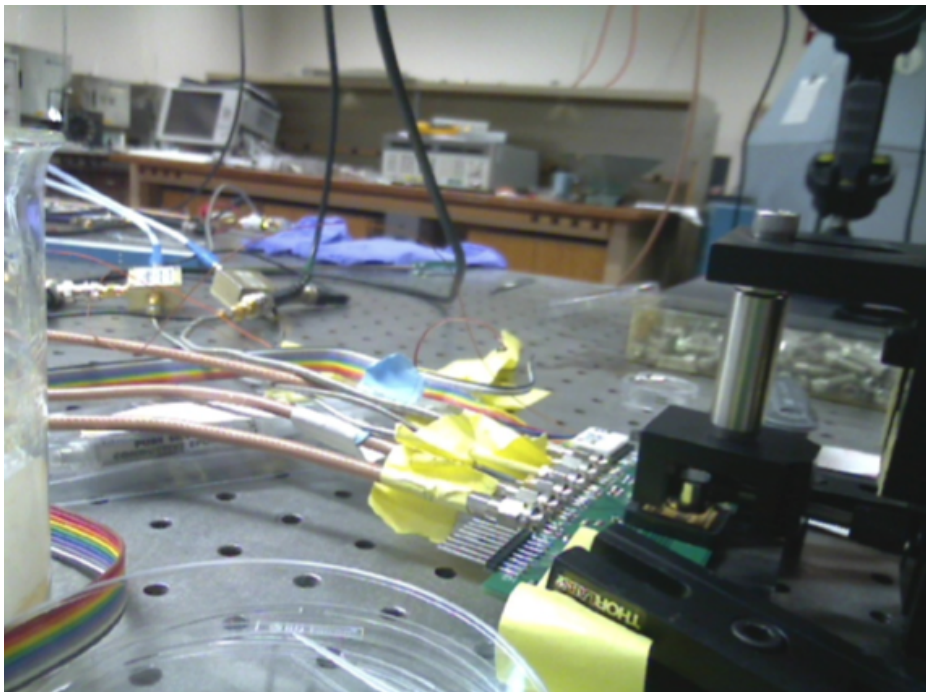

Figure 2.28: To test sensitivity of magnetic freezing to magnet placement, a magnet's position is varied vertically above the sensor.

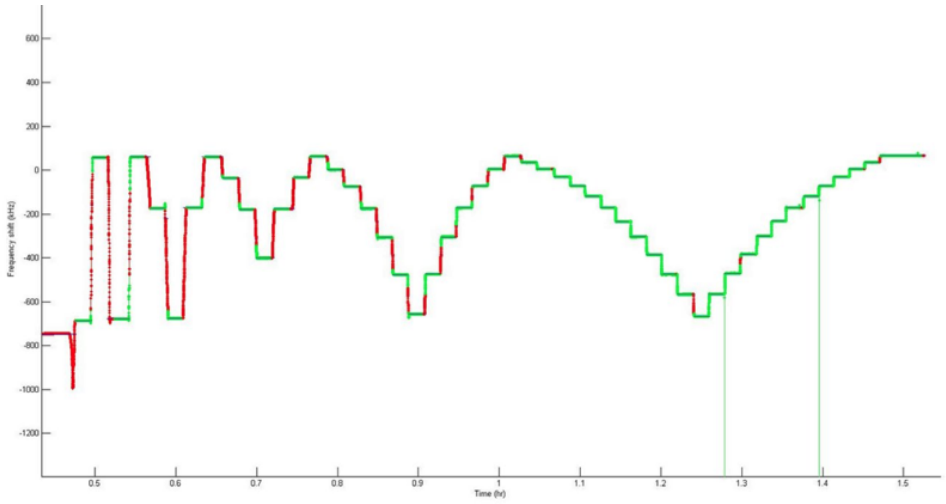

Figure 2.29: Demonstration of vertical sensitivity of saturating magnet. The magnetic saturation curve can be seen from this graph.

power of the FFT of the signal (Fig. 2.34a). Next, the signal is multiplied by a sinusoid in the time domain. Assuming proper phase shift, the multiplication of the sinusoid and signal should correlate to beads over the sensor. However, the proper phase shift is difficult to ascertain. Thus, the original signal is multiplied with many sinusoids of varying phase shifts, and a maximum convolution power is obtained. The convolution power versus beads over the sensor is shown in Fig. 2.34b. As can be

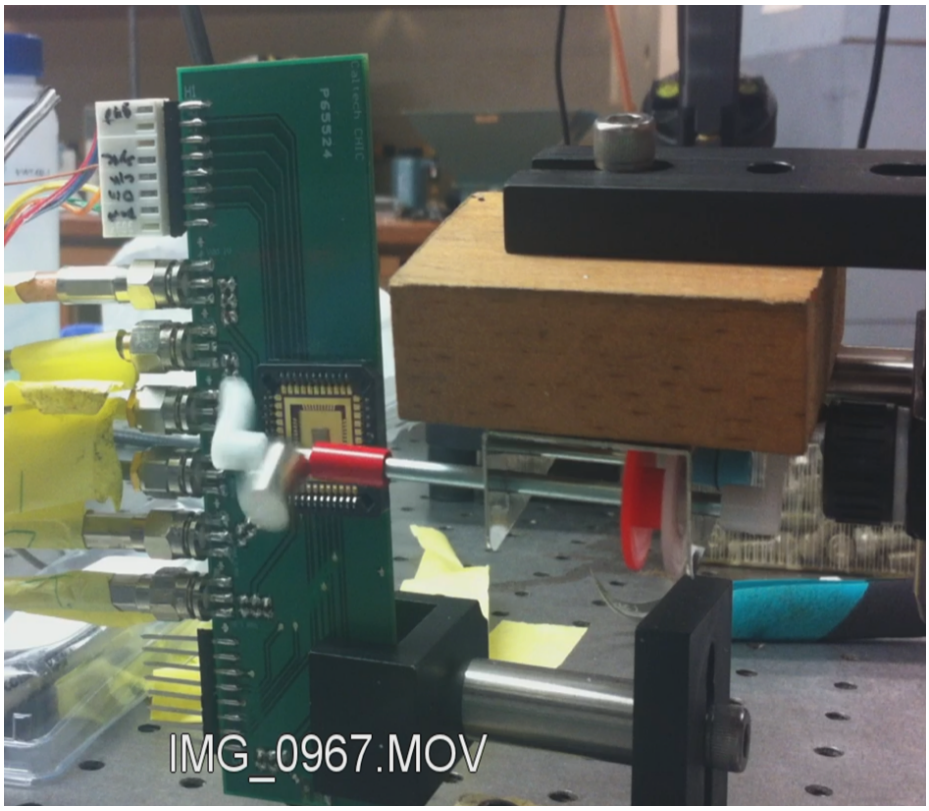

Figure 2.30: Variation of magnetic freezing using a rotating magnet.

seen, the resulting signal is more linear than the previous detection scheme.

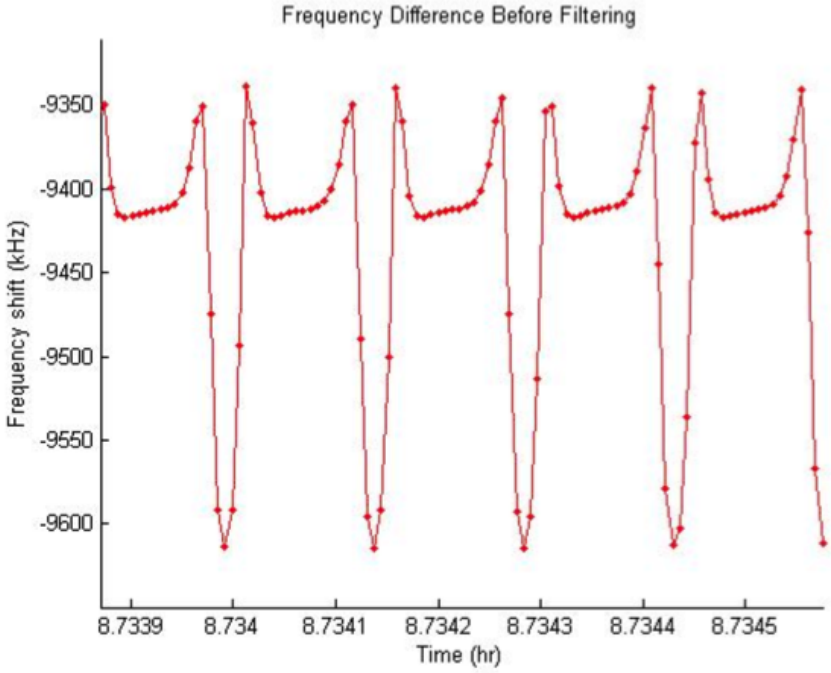

(a)

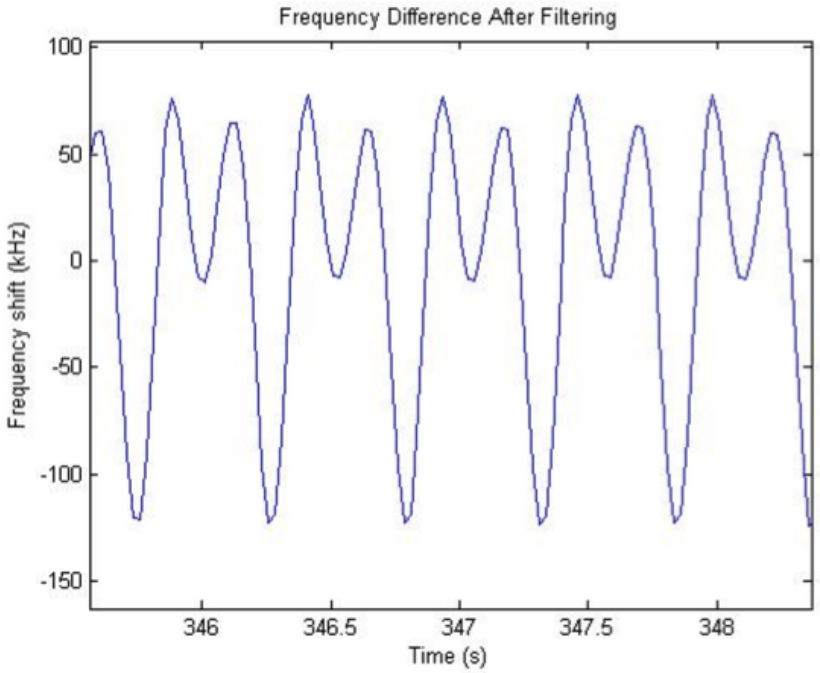

(b)

Figure 2.31: Sensor response to motorized magnetic freezing (a) before and (b) after filtering.

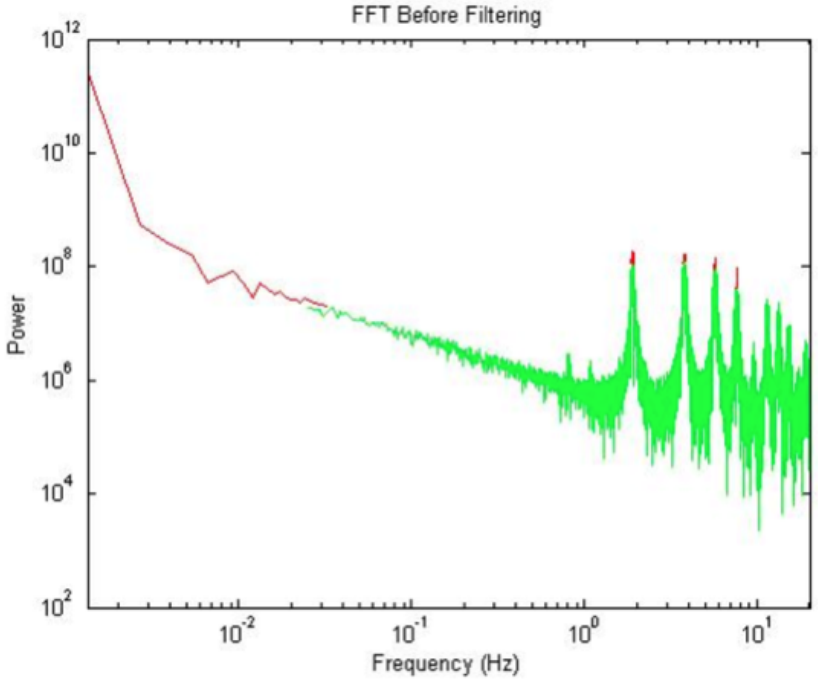

(a)

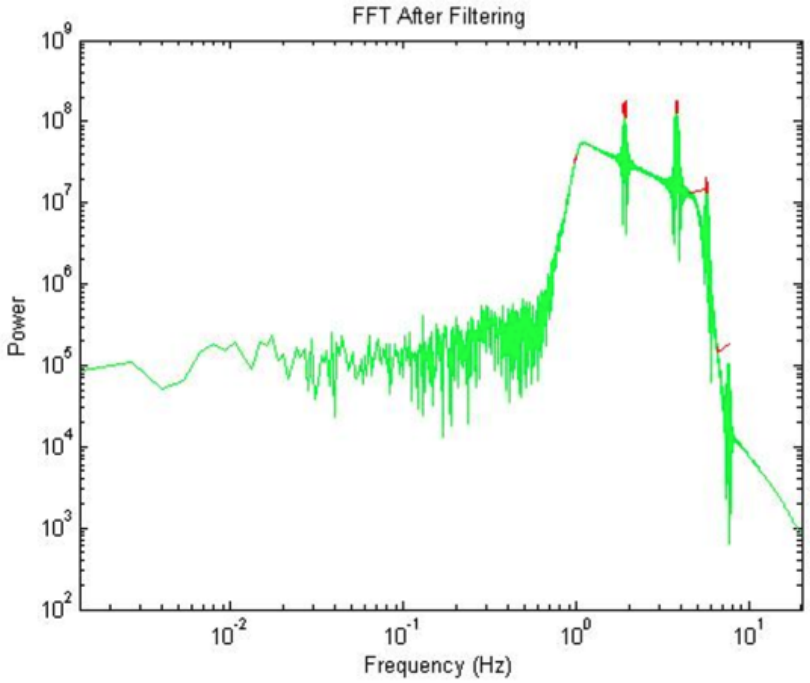

(b)

Figure 2.32: FFT of sensor response to motorized magnetic freezing (a) before and (b) after filtering.

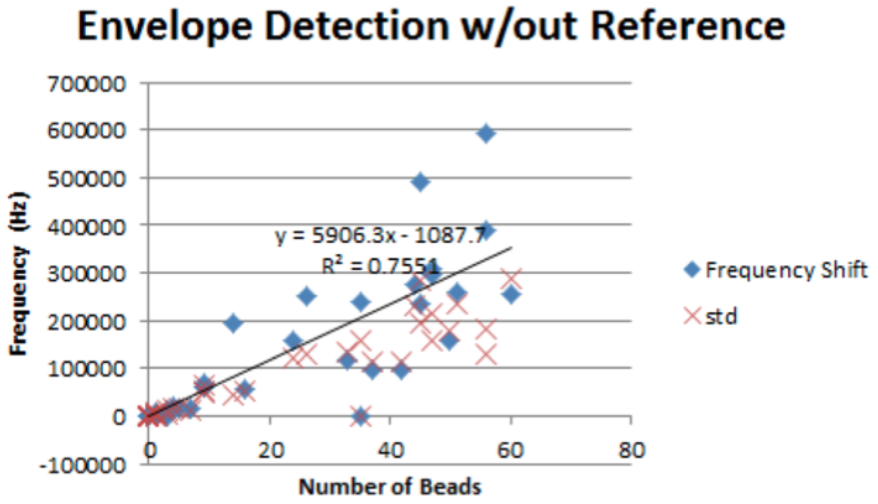

(a)

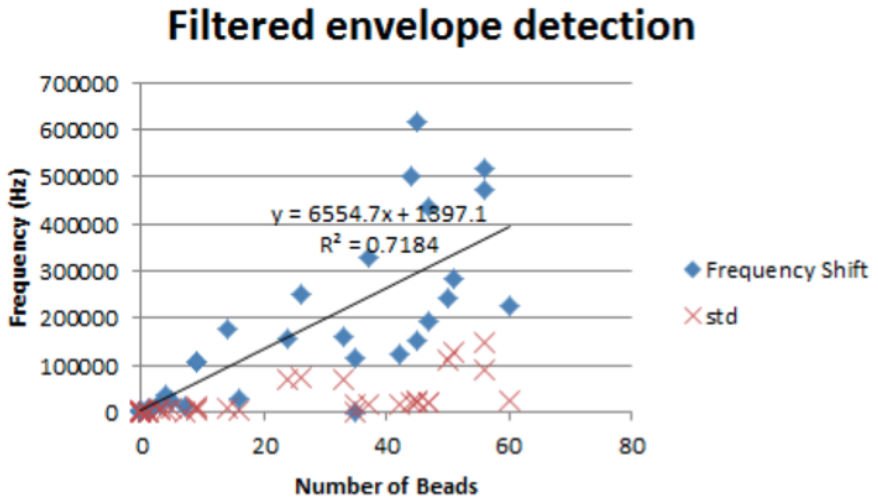

(b)

Figure 2.33: Bead quantitation of motorized magnetic freezing(a) before and (b) after filtering.

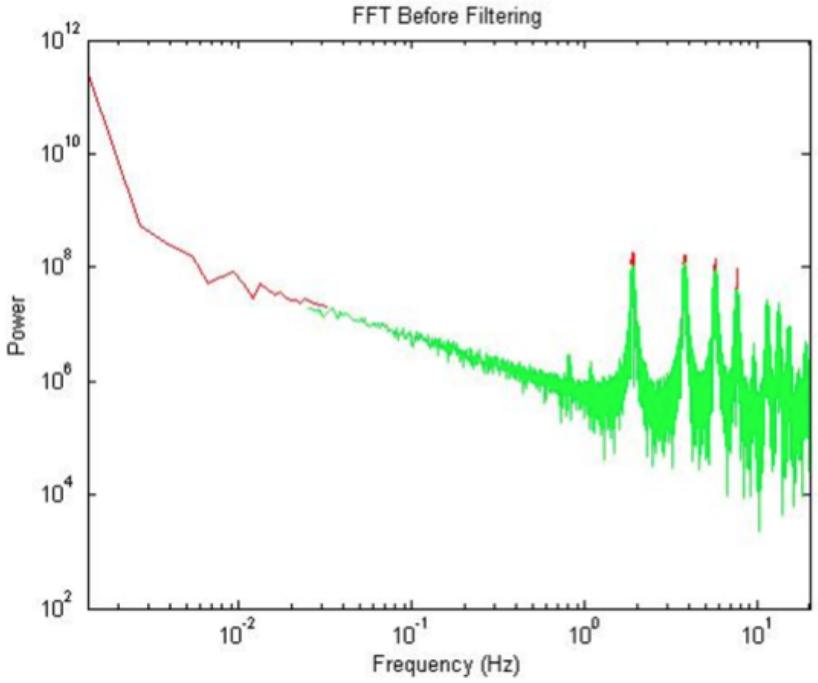

(a)

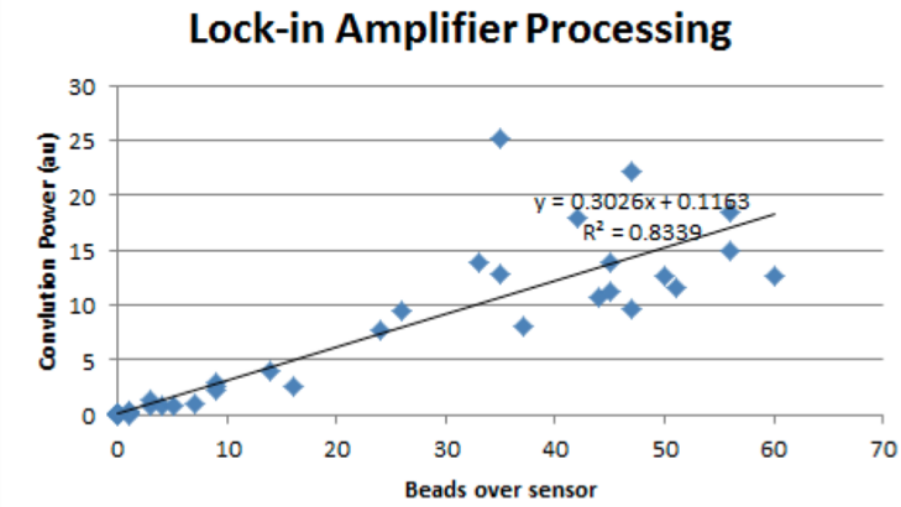

(b)

Figure 2.34: Lock-in amplification of motorized magnetic freezing (a) FFT and (b) quantitation.

2.1.17 Absolute Oscillation Frequency of Biosensor Array

In the frequency shift biosensor, two frequency differences are calculated. The first difference is between the absolute frequency of the sensing inductor and that of the reference inductor. This is done to reduce correlated noise in measurements. The second difference is an additional subtraction between the previously mentioned reference difference and the same difference while the sensor is magnetically frozen (baseline measurement). The difference between the reference and sensing inductor has an offset. Experiments are conducted to discern the source of this offset. The source of these fixed offsets are due to a process dependent capacitance variation in the IC. However, fixed offsets do not impact the final signal from the system.

The biosensor array is shown in Fig. 2.35. The absolute frequency difference can be seen in Fig. 2.36. To analyze the trend of the absolute oscillation frequency, the mean and standard deviation of aggregate columns are plotted (Fig. 2.37a). The sensors are 16 repeated standard cells of a VCO. Therefore, the trend in oscillation among the pairs should correspond with the separation of the VCOs: 360 μm. Where would the capacitors of the second, 4th, and 6th rows have be located such that there exists a constant gradient of capacitance, and thus a constant gradient of oscillation frequency? The repositioned rows are shown in Fig. 2.37b. The new separations distances were drawn with a ruler to the right of the biosensor array (Fig. 2.35a). By juxtaposing the ruler to approximately the center of mass of the first capacitor, we can see the other rulers line up to the center of mass of subsequent capacitors. This implies that a process gradient leads to a linear dependency of capacitance, and thus resonant frequency.

2.1.18 Conclusion

We have presented a low-cost, low-power, amplification-free, handheld diagnostic platform for point-of-care diagnostics. The platform consists of a disposable cartridge containing 48 sensor sites in an area of 3 mm^2. The cartridge can be easily and cost effectively scaled for more sensor sites without increasing the size or cost of the platform. The platform requires no bulky or expensive infrastructure such as microfluidic pumps or optical elements. Scanning time consists of 10 s per sensor site at the conclusion of the biological assay and requires no calibration or warm-up. All sites are contained in a single reaction well for ease of use and we have demonstrated specificity of capture oligomers and antibodies for a target DNA sequence and IFN-γ. We have demonstrated simultaneous measurement of multiple sensing sites and believe this could be extended to enable spatial multiplexing of multiple targets. Commercial products exist [81] for magnetic bead extraction of genomic DNA from whole blood at concentrations greater than 1 nM. Additionally, our technology could be coupled with various isothermal DNA amplification techniques for applications that require increased sensitivity [22]. Both DNA and antigen targets are compatible with the detection system.

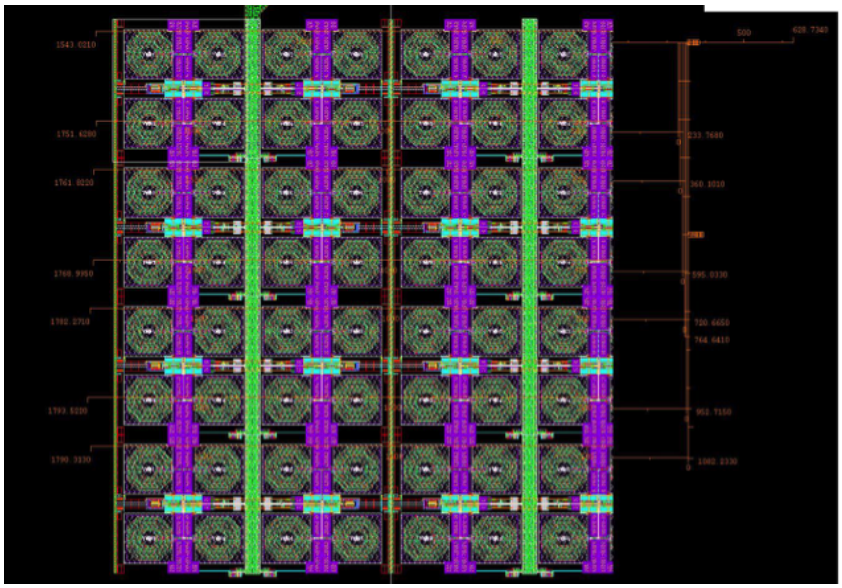

(a)

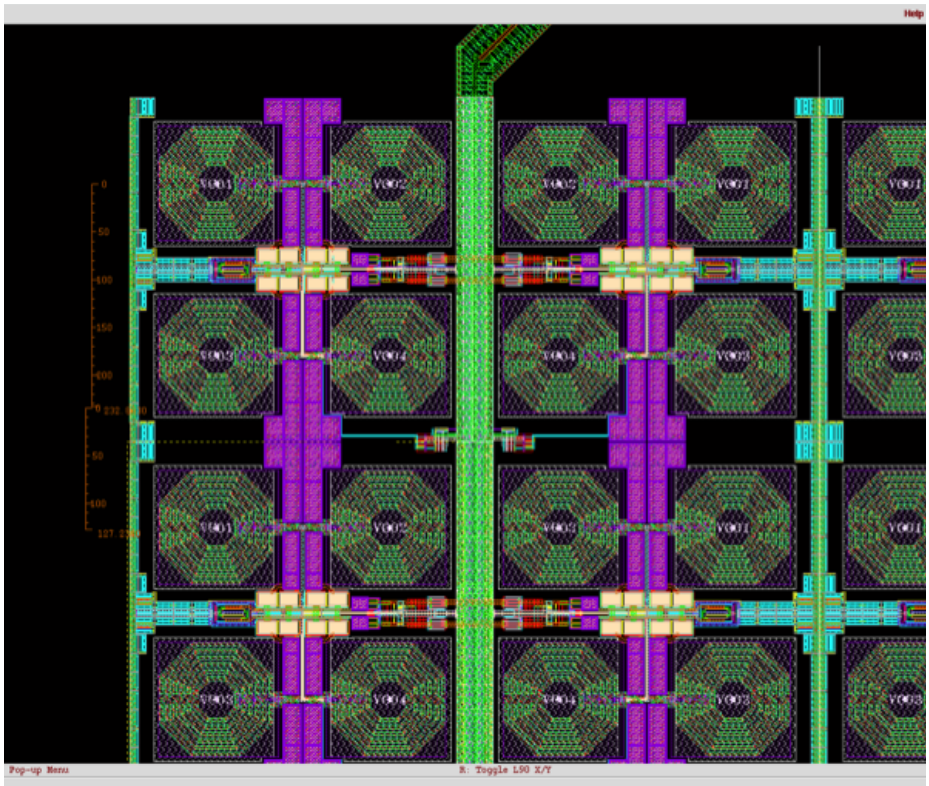

(b)

Figure 2.35: (a) Layout of biosensor array and (b) zoomed picture. Capacitors are colored purple.

To use the sensing platform, a user plugs in the prefabricated cartridge specific to the cartridge reader. Next, the assay The platform has been demonstrated to be capable of indirectly-labeled detection of DNA to 100 pM and IFN-γ antigen to 1 pM. The sensor sites can be used to detect

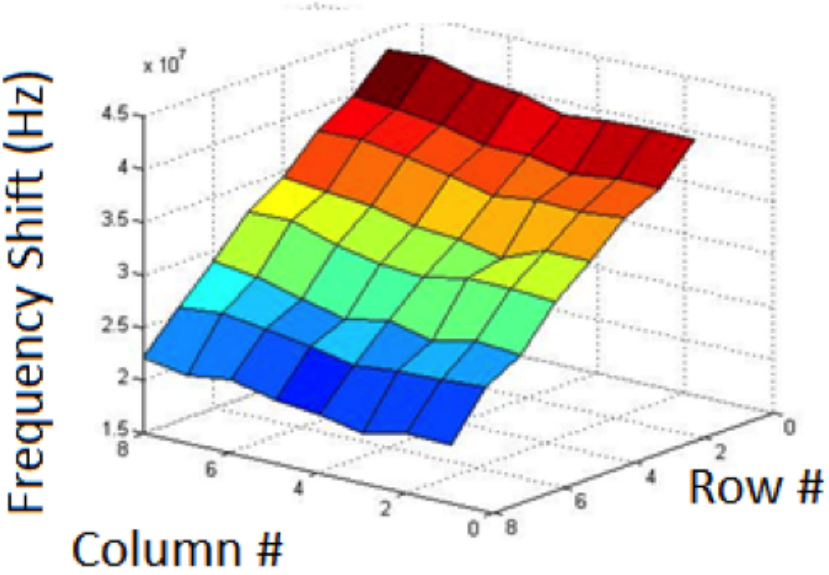

Figure 2.36: Frequency shfit of each sensor in the biosensor array. The actual frequency shift is the plotted value added to 960MHz. A row-dependent linear gradient of oscillation frequency can be seen.

multiple unique targets or replicate targets for higher fidelity. This platform leverages the research and development in magnetic bead manipulation, thus allowing the technology to be compatible with magnetic bead based sample preparation. We have also developed a reliable protocol to functionalize DNA oligomers and antibodies to CMOS based sensors. The same protocols can theoretically be applied to many different DNA sequences or one of hundreds of commercially available sandwich immunoassay kits. We have introduced a measurement technique called magnetic freezing to improve noise performance, eliminate the need for a baseline measurement, and decouple the biological assay from scanning. Because our reader was constructed with standard electronics that can be integrated onto IC chips, the entire measurement system could consist of just the disposable cartridge with a small battery. These milestones enhance the POC viability of the magnetic frequency shift biosensor and future silicon IC biosensors. The sensor can be combined with lateral flow or microfluidics 2.38 for integrated sample preparation.

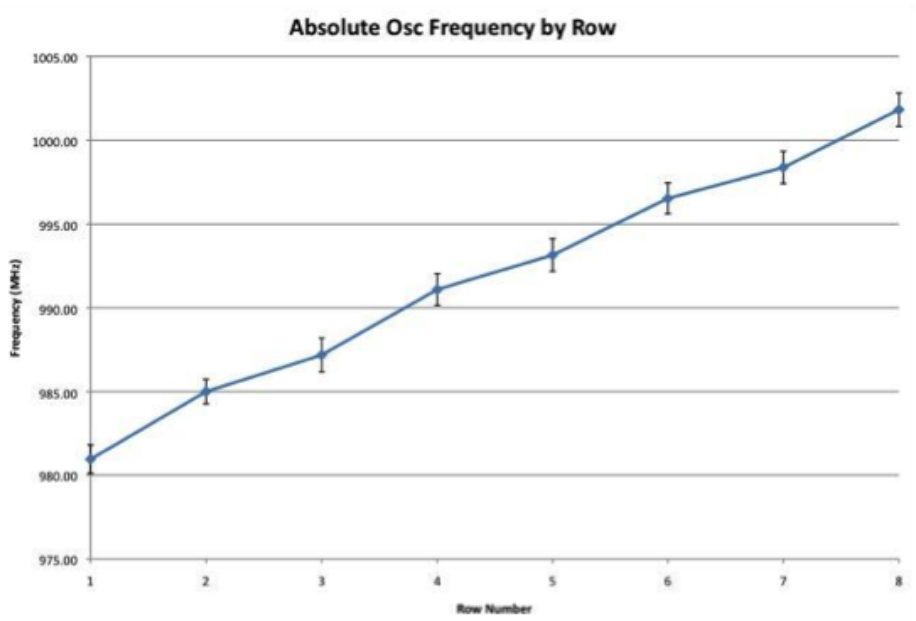

(a)

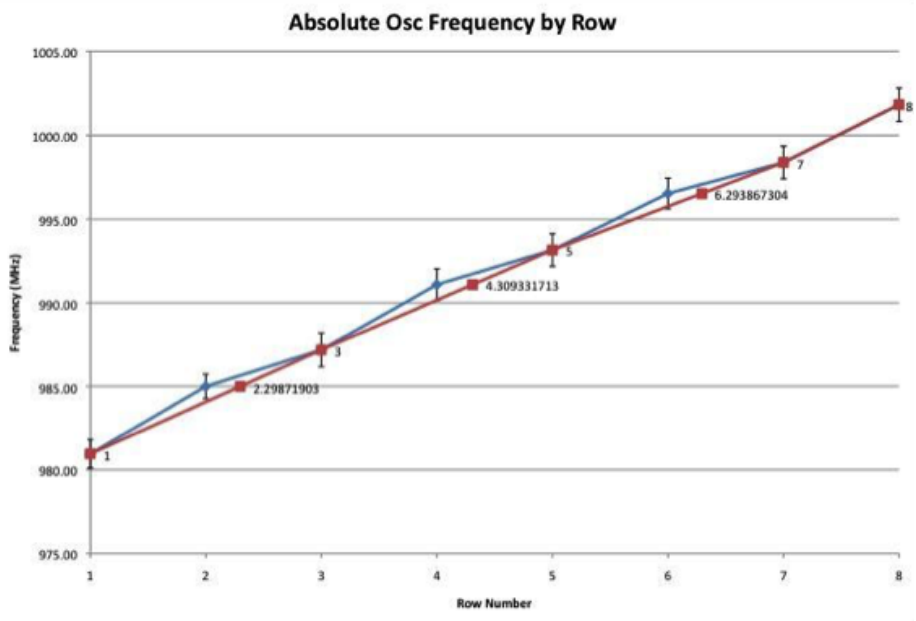

(b)

Figure 2.37: (a) Average row frequency shift and standard deviation. (b) Repositioned row placement for a linear fit between row spacing and linear frequency shift response.

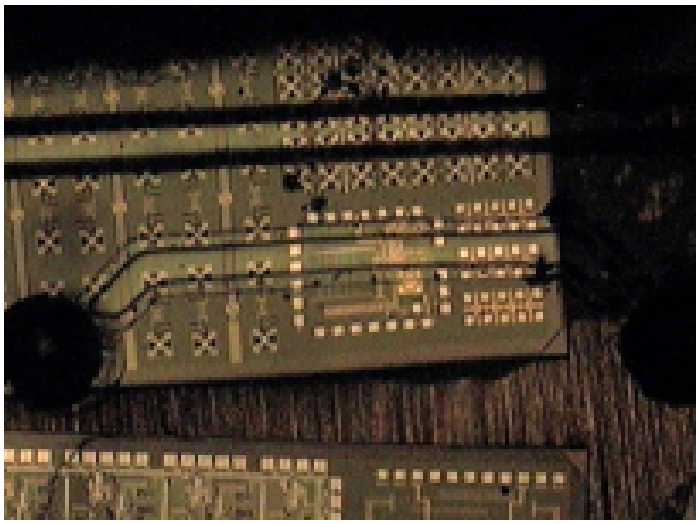

Figure 2.38: The biosensing platform is demonstrated with integrated microfluidic channels.

2.2 DPMF for Trafficking of Activated Macrophages for Brain Tumor Therapy

2.2.1 Introduction

Malignant brain and central nervous system tumors have dismal median survival rates between 1-2 years [3]. Immunotherapy utilizing functionalized nanoparticles has been shown to be a promising treatment for intracranial gliomas, the most common type of malignant brain tumor [85]. However, the retention and delivery of immune cells and nanoparticles to the tumor site remains a hurdle of immunotherapy. We propose a method for magnetically delivering nanoparticles and cells to a target site. The ability to control the location of immune cells during or following activation would represent a powerful new technique for this field. Targeted magnetic delivery is emerging as a technique for controlling cell movement and localization. Here we show that this technique can be extended to microglia, the primary phagocytic immune cells in the central nervous system. The magnetized microglia were generated by loading the cells with super paramagnetic iron oxide nanoparticles (SPION) functionalized with CpG oligonucleotides to form a SPION-CpG construct[1]. This serves as a proof of principle that nanoparticles can be used to both deliver an immunostimulatory cargo to cells and control the movement of the cells. The nanoparticle-oligonucleotide conjugates are efficiently internalized, non-toxic, and immunostimulatory. We demonstrate that the *in vitro* migration of the adherent, loaded microglia can be controlled by an external magnetic field, and that magnetically-induced migration is non-cytotoxic. Analysis of cell movement velocities

[1]This project was the product of a truly amazing collaboration with Behnam Badie, Jacob Berlin, Ethan White, Torkom Pailevanian, Kaushik Dasgupta, Darya Alizadeh, Pengpeng Cao, Yiming Weng, Anil Suresh, Desiree Van Haute, and Jeff Sherman. This contribution of this work was primarily in developing the cell box apparatus, trafficking analysis, magnetic control, and image processing.

clearly demonstrates increased cell velocities toward the magnet. These studies represent the initial step towards our final goal of using nanoparticles to both activate immune cells and to control their trafficking within the diseased brain. In order to capture videos of this magnetically-induced migration of loaded cells, a novel 3D-printed cell box was designed to facilitate our imaging application. We present a scaled-down proof of concept for this manipulation system while easily tracking particle and cell locations. This prototype is a complete cell-culturing system capable of manipulating and imaging cells loaded with magnetic nanoparticles (Fig. 1.10). The system can dynamically actuate over a wide variety of magnetic field profiles and can toggle between them (Fig. 2.39b). Moreover, this system provides a research tool for the magnetic manipulation of cells and particles in a bulk media solution. Magnetic particle manipulation has seen a large growth of applications among basic science measurements using magnetic tweezers [86], cell separation [87], and tissue engineering [88]. However, these systems have small active areas and require complicated setups, and are costly, unscalable, and difficult to image [89]. By manipulating cells contained in a petri dish of cell media, problems related to lack of cell media and nutrients are alleviated. This enables long-term cell experiments of bulk cell populations with identical environmental conditions. The compact system is designed to fit onto a standard 100 mm diameter petri dish. The system is compatible with a wide variety of inverted microscopes for live-cell imaging with bright-field or fluorescence microscopy. We also developed a protocol for the loading of magnetic nanoparticles in human monocytes (THP-1). We use these capabilities to magnetically actuate the monocytes while simultaneously imaging and culturing them (Fig. 2.42b).

2.2.2 Magnetic Trafficking Calculations

2.2.2.1 Review of Magnetics

It is useful to consider the units of quantities involved in magnetics calucations [90].

Magnetostatic equations can be derived from Maxwell's equations,

$$\nabla \cdot \mathbf{D} = \rho \tag{2.1}$$

$$\nabla \cdot \mathbf{B} = 0 \tag{2.2}$$

$$\nabla \times \mathbf{E} = -\frac{\partial \mathbf{B}}{\partial t} \tag{2.3}$$

$$\nabla \times \mathbf{H} = \mathbf{J} + \frac{\partial \mathbf{D}}{\partial t} \tag{2.4}$$

where $\mathbf{D}$ is the displacement field, $\mathbf{E}$ is the electric field, $\mathbf{J}$ is the current density, and ρ is the charge density.

Quantity	Symbol	CGS units	Conv. factor	SI units
Magnetic flux density	B	gauss (G)	10^{-4}	tesla (T) = Wb/m^2
Magnetic flux	ϕ	G $\cdot$ cm^3	10^{-8}	weber (Wb) = volt sec (Vs)
Magnetic field strength	H	oersted (Oe)	$10^3/4\pi$	A/m
Volume susceptibility	χ	dimensionless	4π	dimensionless
Mass susceptibility	ρ	cm^3/g	$4\pi \times 10^{-3}$	m^3/kg
Permeability	μ	dimensionless	$4\pi \times 10^{-7}$	H/m
Relative permeability	μ_r	not defined	-	dimensionless
Demagnetization factor	D	dimensionless	$1/4\pi$	dimensionless

Table 2.3: Magnetic Units

In magnetostatics, these equations reduce to,

$$\nabla \cdot \mathbf{B} = 0 \tag{2.5}$$

$$\nabla \times \mathbf{H} = \mathbf{J} \tag{2.6}$$

2.2.2.2 Field Calculations from a Dynamically Controlled Grid

For steady currents, the magnetic flux density can be explicitly calculated using the differential form of the Biot-Savart (or Biot-Savart-Laplace) law,

$$d\mathbf{B} = \frac{\mu}{4\pi} \frac{Id\ell \times \hat{\mathbf{r}}}{r^2} \tag{2.7}$$

where $d\ell$ is the differential current length element, is the I is the current of the element, $\hat{r}$ is the unit displacement vector, and r is the distance from the current element.

For a long and thin cylindrical wire, we can solve the magnetic flux density as a function of the radial distance from the center of the wire. Utilizing symmetry and Ampere's law, we find that the magnetic flux is given by,

$$\mathbf{B}(r) = \frac{\mu I}{2\pi r}\hat{\mathbf{r}} \tag{2.8}$$

2.2.2.3 Magnetic Force on a Magnetic Particle

The general expression for the magnetic force ($\mathbf{F}$) on a magnetizable object is given by [91, 92],

$$\mathbf{F} = \mu_0 \int_V (\mathbf{M} \cdot \nabla)\mathbf{H} d^3r \tag{2.9}$$

where $\mathbf{M}$ is the magnetization of the particle and $\mathbf{H}$ is the magnetic field in the absence of the magnetizable object.

2.2.2.4 Magnetic Force on a Paramagnetic Particle

For a spherical bead of homogeneous magnetizing field is affected by the demagnetization factor (N) and is given by [91],

$$\mathbf{M} = \chi\mathbf{H} = \frac{\chi_i}{1 + N\chi_i}\mathbf{H} \tag{2.10}$$

where χ_i is the intrinsic magentic susceptibility. For a spherical particle, $N = \frac{1}{3}$.

The force on a paramagentic particle depends on the magnetic field.

$$\mathbf{F} = \frac{V\Delta\chi}{\mu_0}(\mathbf{B} \cdot \nabla)\mathbf{B} \tag{2.11}$$

where V is the volume of the paramagnetic particle, and $\Delta\chi$ is the difference in volume susceptibility between the particle and the environment.

For a cartesisan coordinate system, this expression becomes,

$$\mathbf{F} = (B_x\frac{\partial B_x}{\partial x} + B_y\frac{\partial B_x}{\partial y} + B_z\frac{\partial B_x}{\partial z})\hat{\mathbf{x}} + (B_x\frac{\partial B_y}{\partial x} + B_y\frac{\partial B_y}{\partial y} + B_z\frac{\partial B_y}{\partial z})\hat{\mathbf{y}} + (B_x\frac{\partial B_z}{\partial x} + B_y\frac{\partial B_z}{\partial y} + B_z\frac{\partial B_z}{\partial z})\hat{\mathbf{z}} \tag{2.12}$$

For our earlier example of a long, thin cylindrical wire, we can calculate the magnetic force on a small superparamagnetic particle. We use equations 2.8 and 2.11 to obtain,

$$\mathbf{F}(\mathbf{r}) = \frac{-V\Delta\chi\mu I^2}{4\pi^2 r^3}\hat{\mathbf{r}} \tag{2.13}$$

2.2.2.5 Inter-particle Electrostatic Repulsion

Particle motility is affected by particle surface charge. The surface charge results in an electrostatic repulsion among particles. This is particularly important when achieving endocytosis of nanoparticles because aggregated particles prevent internalization. Ions in the media solution can reduce the effect of this repulsion through electrostatic shielding.

The first layer formed on the surface of the particle is a rigid layer of absorbed counterions called the Stern layer or Hemholtz layer and has a thickness of approximately the diameter of a hydrated

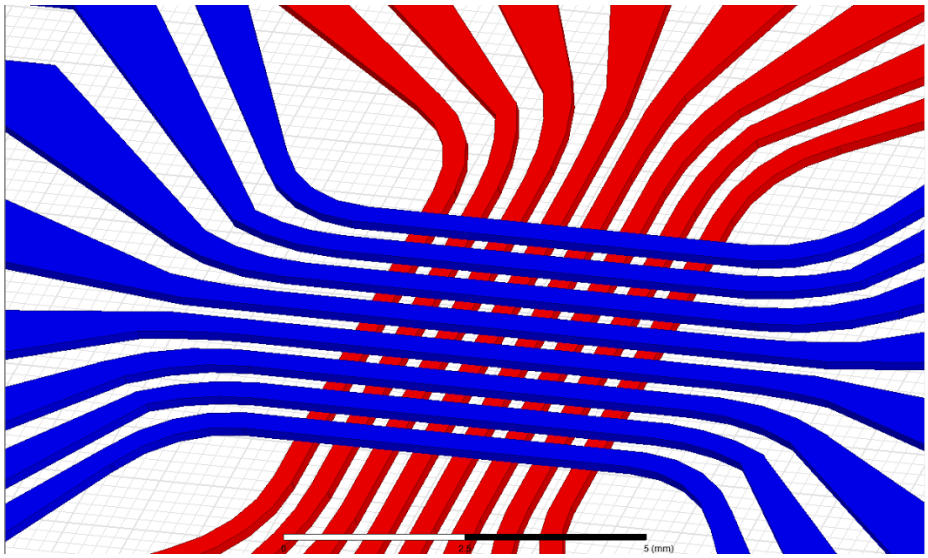

(a)

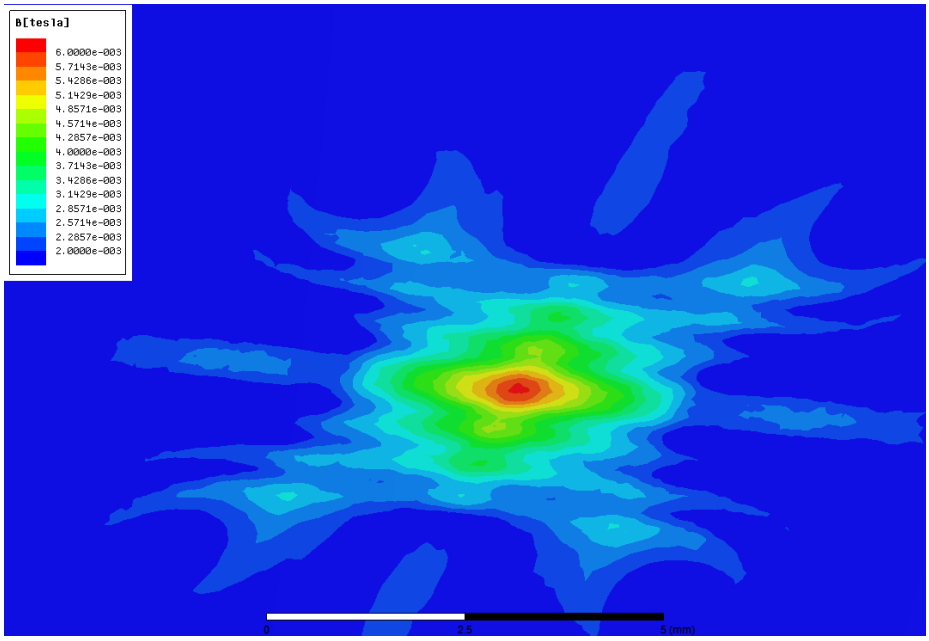

(b)

Figure 2.39: Electromagnetic simulations are used to optimize various magnetic profiles. Profiles can be optimized for various trafficking speeds, focusing size, and aggregation locations. Each array element has a 16-bit bidirectional resolution. Each magnetic profile can be adjusted on a timescale of ms.

ion [93, 94]. Beyond the Stern layer is a diffuse layer called the Gouy-Chapman layer. The plane between the interface of the diffuse layer and Stern layer is called the shear plane [94]. The electric potential between the shear plane and the bulk solution is known as the zeta potential. The thickness of the extension of the diffuse layer into the bulk solution is determined by the Debye legnth (κ^{-1})

and is given by,

$$\kappa^{-1} = \sqrt{\frac{\epsilon_r \epsilon_0 k_B T}{2 N_A e^2 I}} \tag{2.14}$$

where ϵ_r is the dielectric constant, ϵ_0 is the permittivity of free space, k_B is the Boltzmann constant, T is the absolute temperature, N_A is the Avagadro number, e is the elementary charge, and I is the ionic strength of the electrolyte [94, 95].

2.2.2.6 Fluid Dynamics of Nanoparticles and Leukocytes

In order to estimate the velocity of nanoparticles and leukocytes *in vitro*, it is useful to consider the Navier-Stoke's equation for incompressible flow of a homogeneous Newtonian fluid [96],

$$\frac{\partial \mathbf{u}}{\partial t} + (\mathbf{u} \cdot \nabla)\mathbf{u} = -\frac{1}{\rho}\nabla p + \gamma \nabla^2 \mathbf{u} + \frac{1}{\rho}\mathbf{F} \tag{2.15}$$

where $\mathbf{u}$ is the flow velocity, t is time, p is pressure, ρ is density, γ is viscosity, and $\mathbf{F}$ is an external force such as gravity or magnetic force.

The Reynold's number is a dimensionless ratio of inertial and viscous forces, and is useful in predicting flow patterns in fluids. At low Reynolds numbers , viscous forces are dominant and we can treat flow as laminar. At high Reynolds numbers, inertial forces are dominant and flow is turbulent. The Reynolds number (Re) is given by,

$$Re = \frac{\rho u L}{\mu} \tag{2.16}$$

where u is the velocity of the particle, L is the typical length scale of the system, and μ is the dynamic viscosity.

Assuming a low Reynold's number (as is the case with nanoparticles or leukocytes), the frictional force ($\mathbf{F_{fr}}$) is given by,

$$\mathbf{F_{fr}} = 6\pi\mu R v_s \tag{2.17}$$

where μ is the dynamic viscosity, R is the radius of the particle, and v_s is the particle's settling viscosity.

2.2.3 Novel Magnetic Trafficking, Proliferation, and Imaging Box

The system consists of a low-cost magnetic manipulation array, controller, coverslip, and 3D-printed chassis (Fig 1.10). An external magnetic field controller is used to actuate between various magnetic profiles. The controller is interfaced using a computer for accurate timing of profile changes. Our magnetic manipulation array is capable of producing fields up to 10 mT and gradients up to 300 mT/m. The coverslip acts as a waterproof and transparent barrier between the electronics and cell media. An inlet port on the chassis enables the attachment of tubing for providing atmosphere. The

atmosphere travels from the tubing, into the inlet port, through the structure of the chassis, and out through distribution ports inside the petri dish (Fig. 2.41). The assembly of the cell box is shown in Fig. 2.43. As a demonstration of trafficking ability of our cell box, both bead trafficking experiments and cell trafficking are performed. As a control against nonmagnetic fluid flow, we have manipulated both THP-1 cell populations (Fig. 2.42b) and superparamagnetic microparticles (Fig. 2.42a) in the presence of nonmagnetic nanoparticles. The system uses electrical current duty cycling for temperature control. The total active area of the array is approximately 16 mm^2. Electromagnetic simulations were used to investigate various magnetic profiles for maximizing trafficking speed and aggregation profiles. The simulations are shown in Fig. 2.39. The fabricated flexible DPMF array is shown in Fig. 2.40. Each trace has a thickness of approximately140 μm. The pitch and width of each trace is 0.3 mm. The total active area is 7.3 mm^3. The dielectric is composed of a polyimide substrate. The DPMF array is integrated into the cell box.

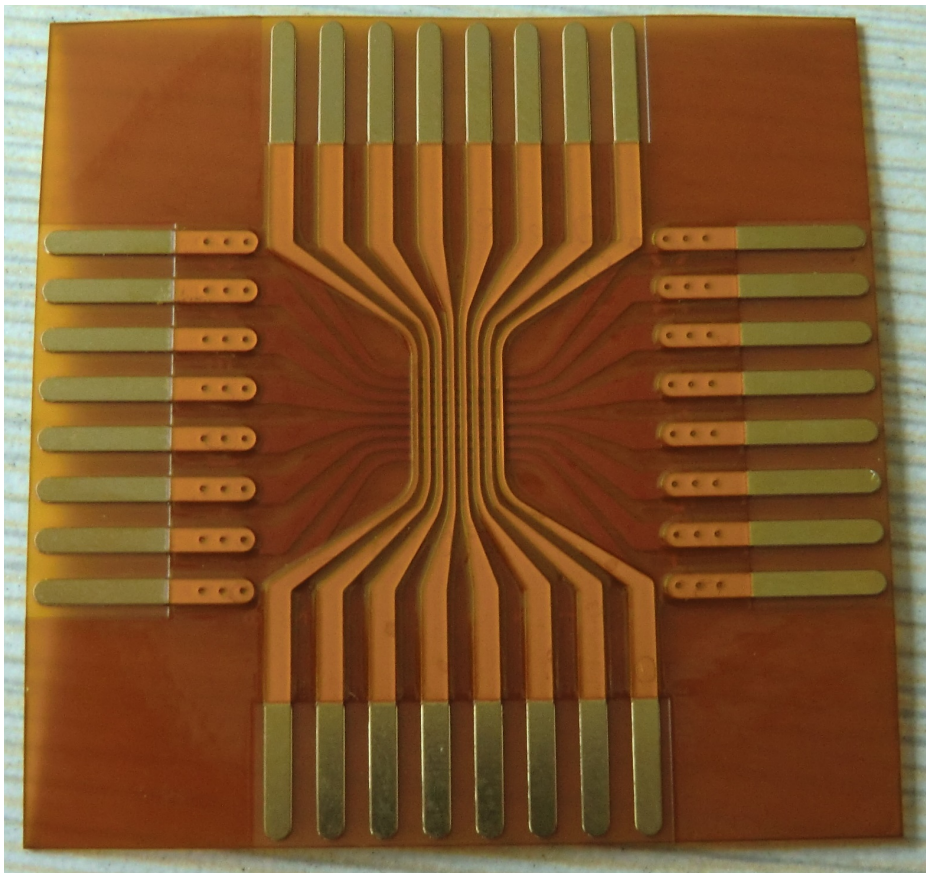

Figure 2.40: Fabricated flexible DPMF array.

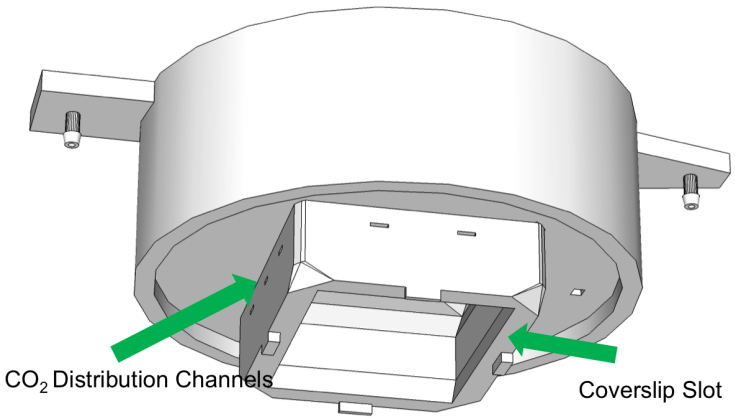

(a)

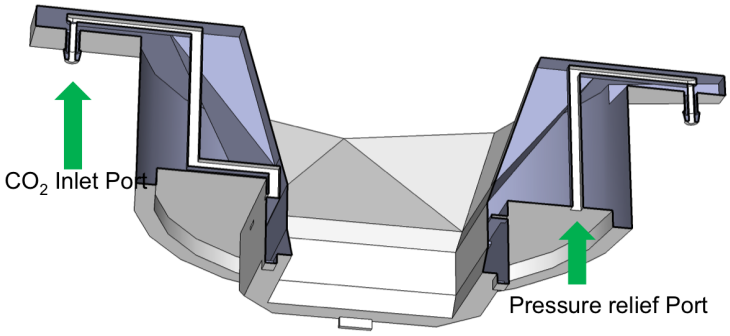

(b)

Figure 2.41: One of the core components of the DPMF device is (a) a 3D printed cell box. The box is printed from PLA plastic and contains life-support features for magnetically trafficked cells. In the split view (b), a CO_2 inlet port and distribution channels ensure optimal pH of cell media. A coverslip slot allows for the waterproof attachment of a large coverslip. The interface ensures the system electronics do not interfere with cell media. The cell box adapts to a standard 100 mm petri dish and fits on typical inverted microscopes.

2.2.4 SPION-CpG Construct

2.2.4.1 SPION-CpG Synthesis

To perform the *in vitro* magnetic field influenced cell movement studies, SPION-CpG conjugates (Fig. 2.44) were prepared from 30 nm SPIONs (Fig. 2.45) [97]. The synthetic protocol was intended to produce CpG conjugated to PEG with a terminal silyl ether for conjugation to the SPIONs, but

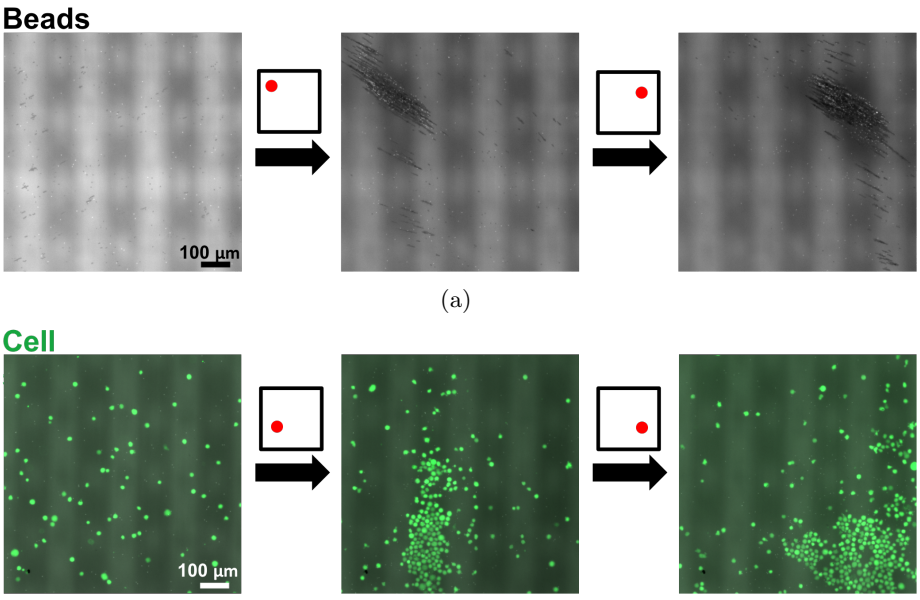

Figure 2.42: Demonstration of magnetic control of magnetic particles and human monocytes (THP-1). Human monocytes endocytosed magnetic particles and were labeled with green fluorescent protein (GFP). The first step of the magnetic control is the aggregation of cells and beads. After aggregation, the cluster is moved to a separate position.

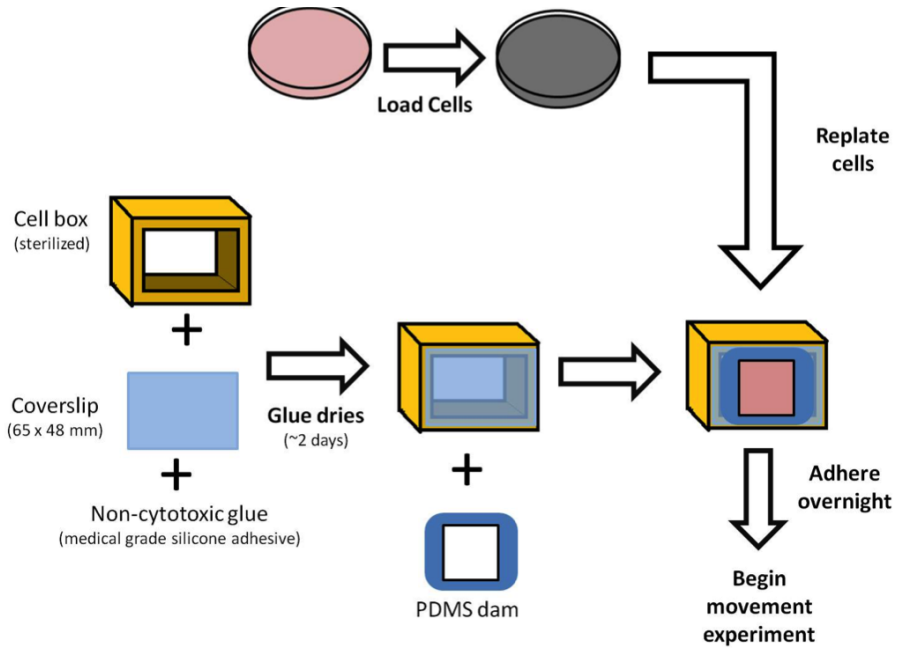

Figure 2.43: Cell box assembly

Mass Spectrometry (MS) analysis (Fig. 2.45) indicated that the reduction of RSSCpG was inefficient and thus the majority of material used to coat the SPIONs was likely RSSCpG. Nonetheless, it was clear that a functional coating was achieved as demonstrated by the change in aqueous stability

of the SPIONs. The as-received SPIONs were coated with oleic acid and thus not miscible with water, but, following sonication with the CpG-containing material, the SPIONs entered the aqueous phase. Furthermore, zeta potential measurements showed the resulting SPION-CpG particles to be negatively charged, consistent with an oligonucleotide coating (Fig. 2.44). Dynamic light scattering measurements indicated that the SPION-CpG conjugates have a hydrodynamic diameter of 94 5 nm, as compared to 46 2 nm for the free SPIONs (Fig. 2.44). This is likely the result of small aggregates forming following the coating, as revealed by transmission electron microscopy (TEM, Fig. 2.44).

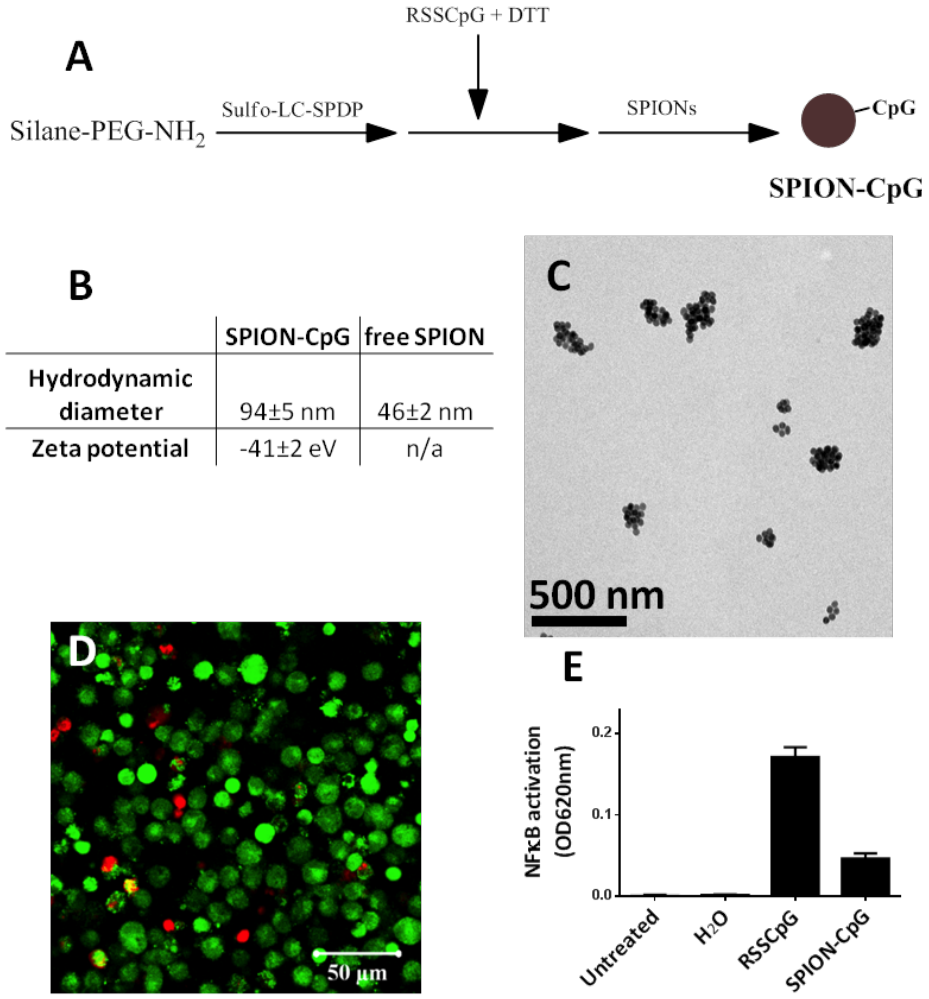

Figure 2.44: Synthesis and characterization of the SPION-CpG conjugates. (a) Schematic illustration of the synthesis of SPION-CpG conjugates. (b) Hydrodynamic diameter and zeta potential of SPION-CpG conjugates. (c) Transmission electron microscopy image of the SPION-CpG conjugates. (d) LIVE/DEAD stain of N9 cells treated with 0.5 mg mL-1 for 12 h. Red = ethidium homodimer (dead), green = calcein AM (live). (e) NFB activation of RAW-Blue mouse macrophage reporter cells treated with 0.1 mg mL-1 SPION-CpG (n = 2, 6 replicates each). The average of the normalized data from two assays is shown.

2.2.4.2 Microglia SPION-CpG Uptake and Viability

Cell assays indicated that SPION-CpG was both non-cytotoxic and immunostimulatory (Fig. 2.44). The LIVE/DEAD assay was used to evaluate cell viability of N9 mouse microglia cells after 12 h of loading at SPION-CpG concentrations up to 0.5 mg mL^{-1}. As shown in Fig. 2.44 and Fig. 2.45 the treated cells exhibited an equivalent level of viability as untreated control cells. In order to evaluate the immunostimulatory potential of SPION-CpG, an NFκB reporter cell line was used. Because NFκB activity is increased in response to TLR9 activation by CpG, immune stimulation by SPION-CpG was expected to cause an increase in NFκB signal within this reporter system. Indeed, SPION-CpG treatment induced an increase in NFκB activity when compared to untreated cells (Fig. 2.44). However, the NFκB activity of SPION-CpG was less than an equivalent amount of free CpG (RSSCpG). This reduction in activity has several possible causes. It is possible that some CpG was lost during the SPION-CpG synthesis process, thus resulting in lower NFκB activity after uptake by reporter cells. It is also possible that the immunostimulatory activity of CpG was partially inhibited by conjugation to SPIONs. Phosphate groups are well-known for their ability to bind the surface of iron oxide [98,99]. Therefore it is likely that the phosphorothioate backbone of the CpG oligonucleotide interacted with the surface of the SPIONs, interfering with CpG release or its binding to TLR9 [100]. Future work will focus on investigating the mechanism of this phenomenon and further enhancing the immunostimulatory activity of SPION-CpG.

Next, inductively coupled plasma mass spectrometry (ICP-MS) was used to quantify the cellular uptake of the SPION-CpG by N9 microglia. Briefly, cells were treated with increasing concentrations (0, 0.01, 0.1, 0.3 and 0.5 mg mL^{-1}) of SPION-CpG conjugates for 12 h, washed thoroughly, digested with nitric acid, and analyzed using ICP-MS. A dose-dependent increase in iron content above the normal background level in control cells was observed (Fig. 2.47). For comparison, cells were also treated with the commercially available Ferumoxytol iron oxide nanoparticles (sold under the name Feraheme), which are approved for human use by the US Food and Drug Administration. Ferumoxytol particles are similar in size to the SPIONs used in this study, with an iron core diameter of 1730 nm [101]. However, even when cells were exposed to a 3x higher concentration of Ferumoxytol as compared to SPION-CpG, very little uptake of the Ferumoxytol particles was observed. While there are a number of differences between our SPION-CpG and Ferumoxytol, we speculate that this increased loading of SPION-CpG was due to the oligonucleotide coating. It has previously been shown that oligonucleotide coatings lead to enhanced cell uptake mediated by scavenger receptors [102, 103]. Independent of the mechanism responsible, the enhanced uptake for our SPION-CpG made this material appealing for use in the magnetic control of microglia.

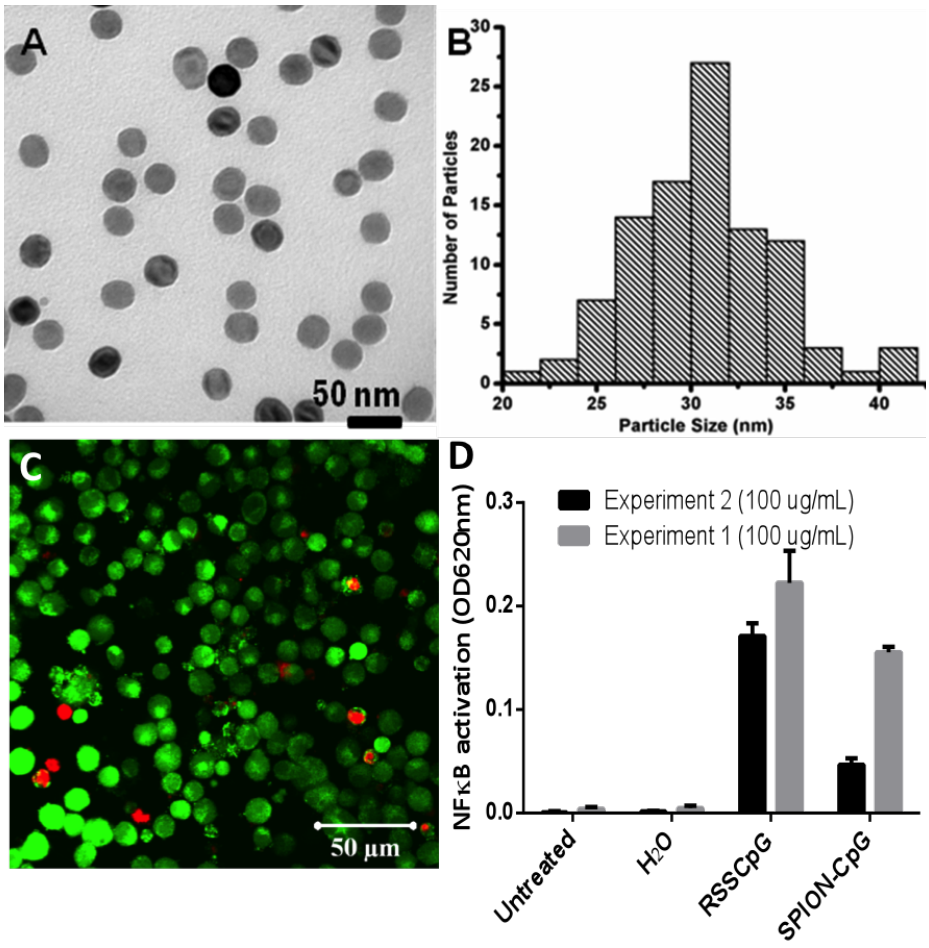

Figure 2.45: (a) Transmission electron microscopy image of the SPION. (b) Histogram size distributions obtained by counting approximately 100 particles. (c) LIVE/DEAD staining of untreated control cells. (d) NFB activity data from two independent assays.

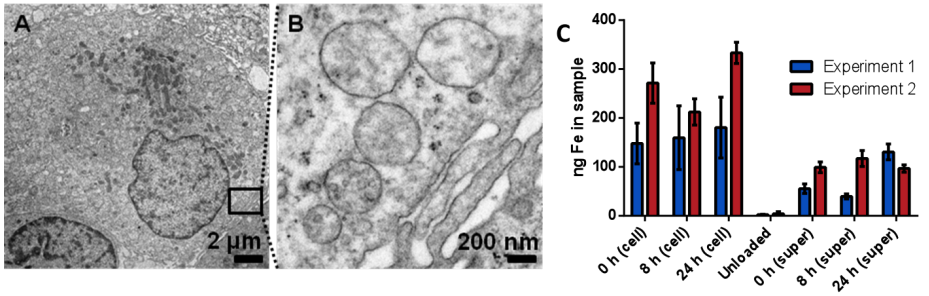

Figure 2.46: SPION-CpG is internalized in N9 cells. Dark-field images of (a) microglia cells alone and (b) cells loaded with SPION-CpG conjugates (0.5 mg/mL). (c-d) TEM images of loaded cells. ICP-MS analysis of (e) cells treated with increasing concentrations of SPION-CpG conjugates and Ferumoxytol. (f) Cell and supernatant fractions at various time points after loading (n=2 with treatments performed in triplicate, data from one experiment is shown). Error bars represent standard deviations of iron content in replicate wells.

2.2.4.3 Large Scale Uptake and Distribution Imaging

Further, dark-field microscopy imaging was performed to show the uptake and distribution of the particles over a relatively large area. N9 cells treated with SPION-CpG conjugates at a concentration of 0.5 mg mL^{-1} were assessed using a dark-field microscope. Untreated control cells showed no uptake (Fig. 2.47), whereas cells treated with SPION-CpG conjugates showed profound uptake of the SPIONs (Fig. 2.47). TEM imaging was also performed to gather information on the intracellular distribution of the SPION-CpG conjugates. At low magnification, TEM imaging performed across various regions of the grid revealed strong uptake of the SPION-CpG conjugates, in agreement with dark-field microscopy. Higher magnification TEM imaging showed dense aggregates of particles that were predominantly located in intracellular vesicles (Fig. 2.47). Some particles were observed in the cytoplasm as well, and no particles were found in the nucleus. Similarly, no uptake was observed in the untreated control cells (Fig. 2.46).

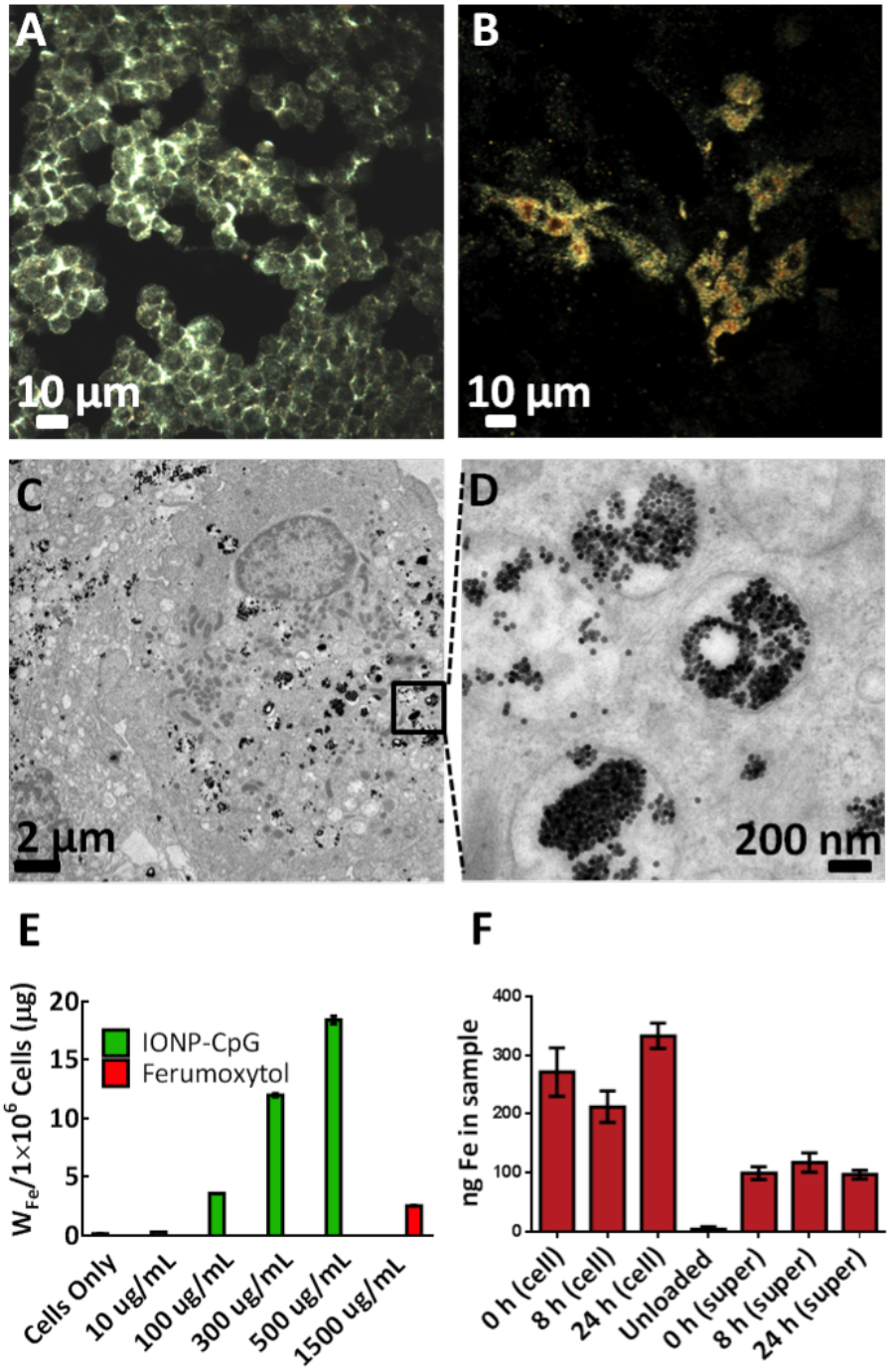

Figure 2.47: SPION-CpG is internalized in N9 cells. Dark-field images of (a) microglia cells alone and (b) cells loaded with SPION-CpG conjugates (0.5 mg/mL). (c-d) TEM images of loaded cells. ICP-MS analysis of (e) cells treated with increasing concentrations of SPION-CpG conjugates and Ferumoxytol. (f) Cell and supernatant fractions at various time points after loading (n=2 with treatments performed in triplicate, data from one experiment is shown). Error bars represent standard deviations of iron content in replicate wells.

2.2.4.4 Microglia SPION-CpG Exocytosis

After verifying that SPION-CpG was internalized by N9 cells, the exocytosis of these particles was then investigated. This has important implications in experiments involving magnetically-induced movement. As a cell exocytoses SPIONs, its responsiveness to magnetic fields will decrease as a function of the amount of residual intracellular iron. Thus the rate of exocytosis affects the time period over which the cells can be moved *in vitro*. In order to track the rate of exocytosis, N9 cells were loaded and the iron content of both the cells and the cell media was measured at 0, 8, and 24 h after loading. Over a 24 h period, there was no detectable increase in the iron content of the cell media nor was there a detectable decrease in the iron content of the cell fraction (Fig. 2.47). Therefore, we concluded that exocytosis of SPION-CpG was negligible in N9 cells over 24 h. The background iron level in the media at 0 h was presumably residual free SPION-CpG which was not removed when the loaded cells were washed with PBS two times. Longer time points were not investigated because 24 h proved sufficient to demonstrate robust *in vitro* movement.

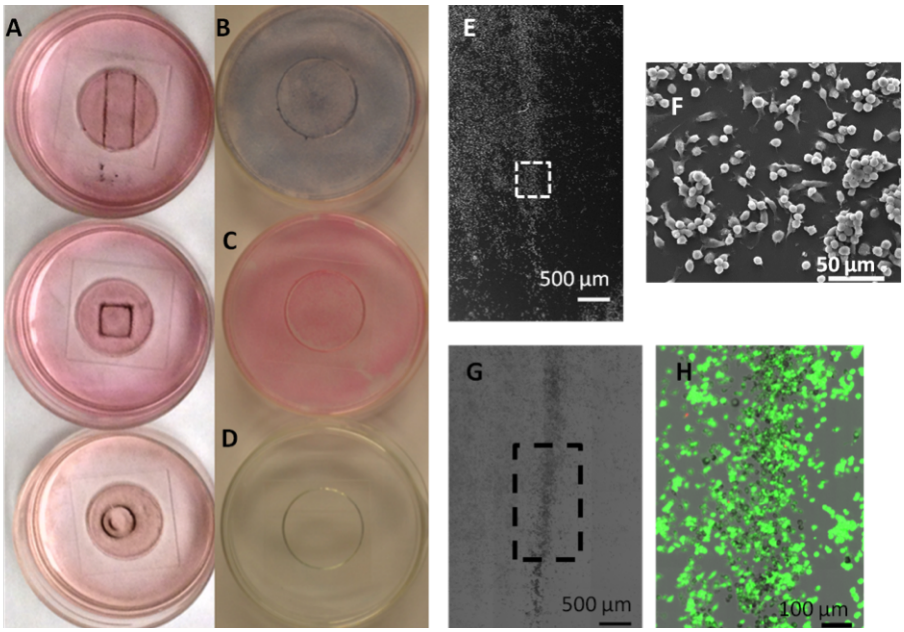

Figure 2.48: Magnetically induced movement of the cells loaded with SPION-CpG conjugates. (a) Color images of loaded cells after exposure to magnets of different shapes for 20 h. The concentration of SPION-CpG used for loading was 0.1 mg/mL. (b-d) are the various controls used for the magnetic movement experiments; unloaded cells with (c) and without (b) exposure to the rectangular shaped magnet, and SPION-CpG only without cells (d). (e-f) SEM images of cells after movement. (g-h) Brightfield and fluorescent images of LIVE/DEAD-stained cells after movement.

2.2.4.5 Demonstration of Magnetic Response using Permanent Magnet

As a simple test to evaluate if SPION-CpG-loaded microglia could be controlled with an external magnetic field, three different shaped magnets were placed underneath glass bottom culture dishes

containing adherent N9 cells loaded with SPION-CpG. After 20 h, the media was aspirated, the plates were stained with Prussian blue, and photographs were taken to demonstrate the shape-dependent localization of the loaded cells (Fig. 2.48). Additionally, this magnetically controlled cell movement was correlated with the dose of SPION-CpG given to the cells, with higher loadings leading to more pronounced accumulation at the magnet (Fig. 2.49). As controls, we also imaged SPION-CpG particles only with magnet exposure, untreated cells with magnetic exposure and cells loaded with SPION-CpG that were not exposed to any magnets. The SPION-CpG only control shows almost no adherence of the particles, such that following staining and washing, very little material remained in the dish (Fig. 2.48). Neither empty cells that were exposed to the magnet nor loaded cells not exposed to the magnet migrated *in vitro*, confirming that the shape-dependent localization of the loaded cells was magnetically controlled (Fig. 2.48). In order to more closely monitor the magnetically induced migration of the cells, higher magnification images were recorded for loaded cells after 0, 2, 4, and 20 h of magnet exposure (Fig. 2.51). Accumulation of the loaded cells at the edge of the magnet where the magnetic field gradient was largest was observed by 4 h and increased until 20 h. Collectively, these controls demonstrate that the accumulation at the edge of the magnet was due to SPION-loaded cells moving in response to the magnetic field.

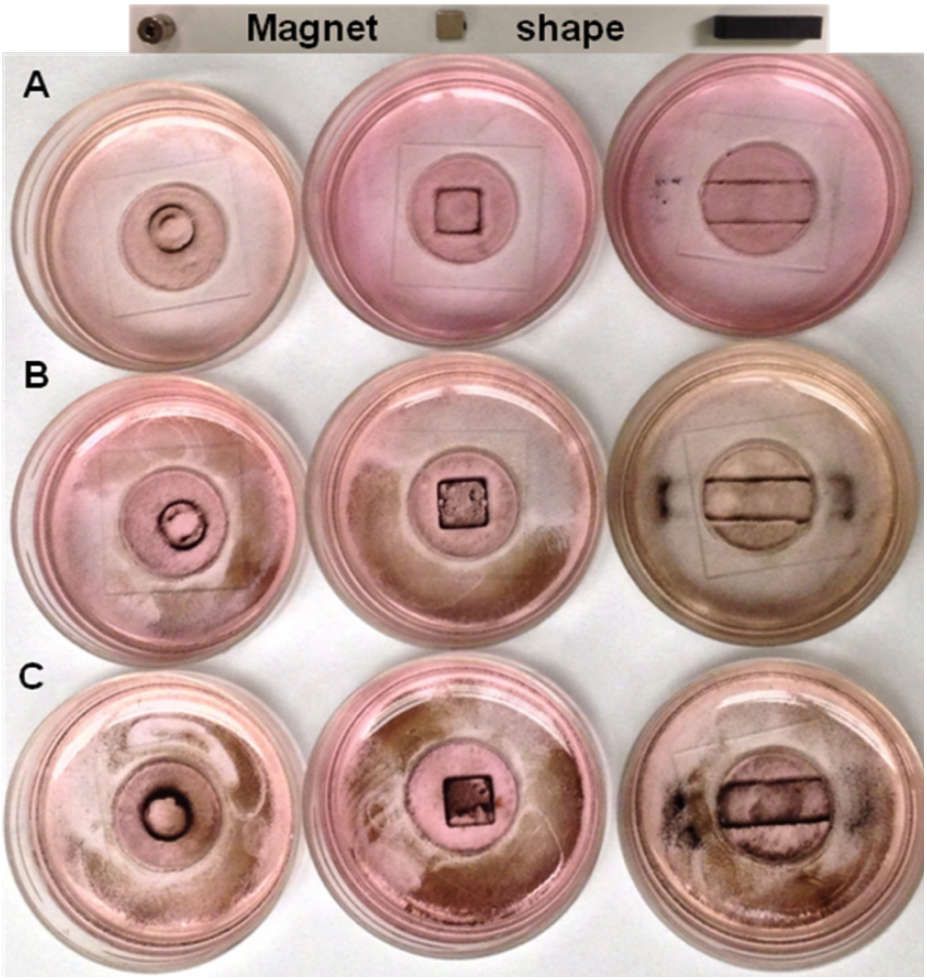

Figure 2.49: Magnetically induced movement of the cells loaded with increasing concentrations of SPION-CpG. Color images of the cells placed underneath the magnet of different shape (shape indicated in the image) for 20 h, taken using an iPhone camera. Increasing concentration of SPION-CpG used were 0.1, 0.3, and 0.5 mg/mL for (a), (b), and (c), respectively.

2.2.4.6 Cell Viability and Morphology After Magnetic Trafficking

In order to verify that magnetically-induced movement was nontoxic, the migrated cells were examined for changes in viability and cell morphology. Because the migrated cells comprise only a small percentage of the total cell population of the dish, assays that analyze the bulk cell population would not be able to detect changes in the migrated cell population due to a high background signal from the non-migrated cells. Furthermore, there is no good way to separate the migrated and non-migrated cell populations prior to analysis. Therefore, analysis of the migrated population was performed using imaging-based techniques. Imaging-based techniques allow the spatial information from the cells to be preserved during the analysis, enabling quick identification of migrated and non-migrated populations.

Viability and cell morphology were examined via the LIVE/DEAD assay and SEM, respectively.

After loaded cells were exposed to the magnet for 20 h and clear migration was observed, the cells in the dish were stained with calcein AM and ethidium homodimer, fixed, and then fluorescently imaged to assess viability. After fluorescence imaging, the same region of cells was imaged by SEM. No decrease in cell viability was detected for migrated cells nor were any gross abnormalities in cell morphology observed (Fig. 2.48, 2.49).

2.2.4.7 Magnetic-field Induced Qualitative Cell movement *in vitro* by bright-field microscopy

The movement of cells loaded with SPION-CpG conjugates is primarily determined by the external magnetic field profile and strength, the hydrodynamic properties of the cell in its environment, and the effectiveness of SPION uptake by the cells. An important evaluation of cell motility is the quantification of movement velocity. Therefore, in order to analyze the movement velocity of cells, an innovative imaging, incubation, and magnetic manipulation apparatus was designed (Fig. 2.43). The apparatus consists of our custom cell box fitted onto a standard sized petri dish. N9 cells were plated onto the coverslip portion of the cell box and then loaded with SPION-CpG. After cell loading, the entire box assembly was then inverted into a petri dish containing culture medium. For time-lapse imaging, the cell box and petri dish were placed onto the stage of an inverted microscope equipped with incubation capabilities. A ceramic permanent magnet was then placed on the opposite side of the coverslip to which the cells were attached.

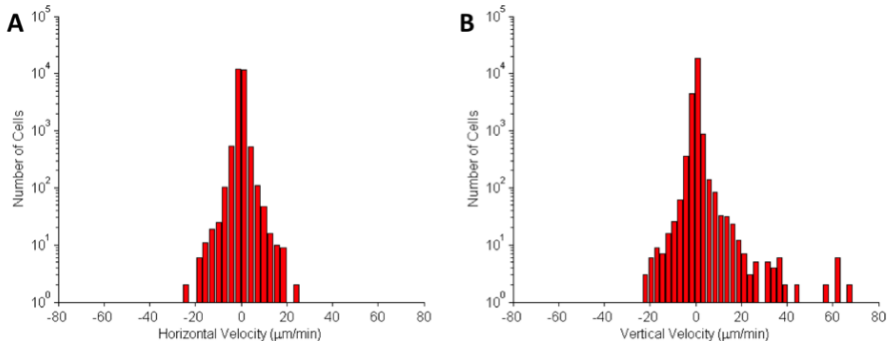

Figure 2.50: Histograms of (a) horizontal and (b) vertical cell velocities in motility experiment. Magnetized cells were imaged over a period of 12 h under the exposure of a magnetic field. The external magnet was placed in the positive vertical position to the cells. Velocities were calculated by extracting the change in cell position from one frame to the next. The average velocity was 0.2±3.72 μm/min and the vertical direction and 0.03±1.69 μm/min in the horizontal direction.

During magnet exposure, the cells were imaged at 2 frames min^{-1} for a period of 20 h. Cell positions were extracted using an image processing algorithm [104]. The distribution of cell velocities in the vertical direction (toward the magnet) and horizontal direction is shown in Fig. 2.50. The histograms in Fig. 2.50 show that the cell movement in the horizontal direction was symmetrical,

while cell movement in the vertical direction was skewed toward the externally-applied magnetic field. In some cases cells migrated toward the magnet at velocities exceeding 30 μm min^{-1}.

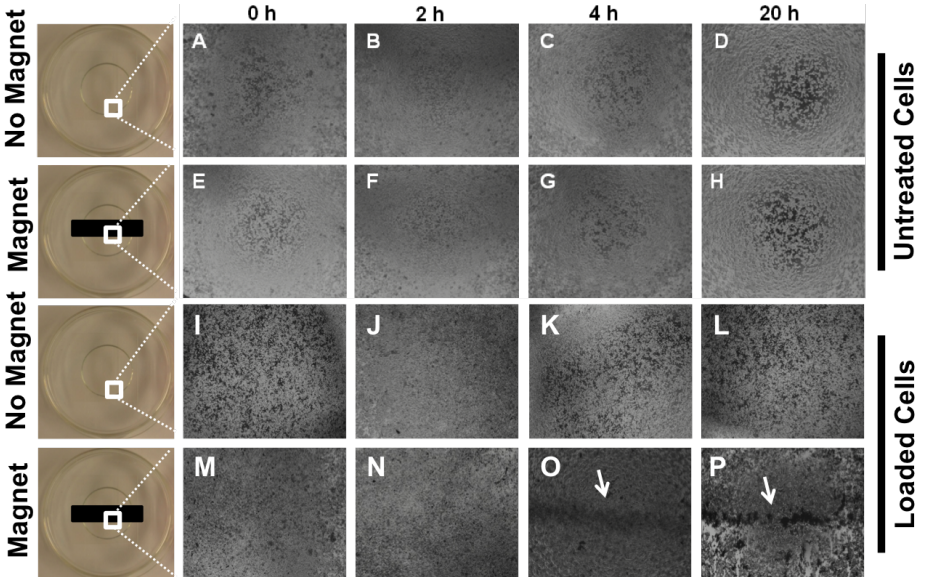

Figure 2.51: Time-lapse of cell movement

2.2.5 Conclusion

Immunotherapy is an attractive treatment strategy for many diseases, including cancer [105]. Generally, this strategy involves stimulating the immune system such that it recognizes the diseased cells as foreign and eliminates them. A wide variety of agents, ranging from antibodies, to engineered immune cells, to potent adjuvants have been used to induce immune system stimulation. Immunotherapy would be greatly enhanced as a treatment strategy if the location of the immune cells both during and after stimulation could be controlled. For the case of cancer immunotherapy, it could be of great benefit to localize the immune cells receiving stimulation to the tumor to promote antigen recognition specifically for cancer cells. Furthermore, the immune response could be enhanced by maintaining a population of activated immune cells at the primary tumor site and/or improving the trafficking of activated immune cells to distant foci of disease.

We have been pursuing the use of oligodeoxynucleotides that contain an unmethylated CpG motif (CpG) as immune stimulants for the treatment of glioblastoma. CpG is known to be immunostimulatory by activating toll like receptor-9 (TLR9) which is expressed by normal and glioma-associated human microglia and macrophages [106–109]. SPION-CpG conjugates were non-toxic to N9 microglia cells and were efficiently internalized into endosomal compartments. This enabled magnetic control over microglia motility *in vitro*. This work establishes the possibility of using a nanoparticle to both stimulate immune cells and to control their trafficking.

To magnetically manipulate in a controlled and dynamically actuated profile, a custom 3D printed cell box is introduced. The cell box also enables the simultaneous live imaging and incubation of magnetic particles or cells. The measurement setup is used to manipulate magnetically loaded THP-1 cell. Future experiments will investigate the optimal coating for the SPIONs to further enhance immune cell activation and developing volumetric magnetic manipulation chamber for *in vivo* cell trafficking.

Chapter 3

Other Works

3.1 Transistor Scaling and Variation

Transistor scaling has enabled the exponential growth of the number of CMOS transistors on single die, as predicted by Moore's law [110]. The ability to scale transistors has ushered huge performance gains in computing. This is the result of favorable scaling in transistor parameters such as gate capacitance, switching speed, and propagation delay. However, this scaling has also increased process and dynamic variations of CMOS transistors. For example, random dopant fluctuations are a result of the decreasing number of dopant atoms in a transistor channel and is the major contributor to device mismatch (Fig. 3.1) [5]. As transistor channel length scales smaller, the variabilty in the placement and presence or absence of a few dopant atoms leads to significant transistor performance variation. These variations, along with environmental variations, can be especially detrimental to RF transmitters and receivers. Various techniques are used to mitigates the effects of process variation.

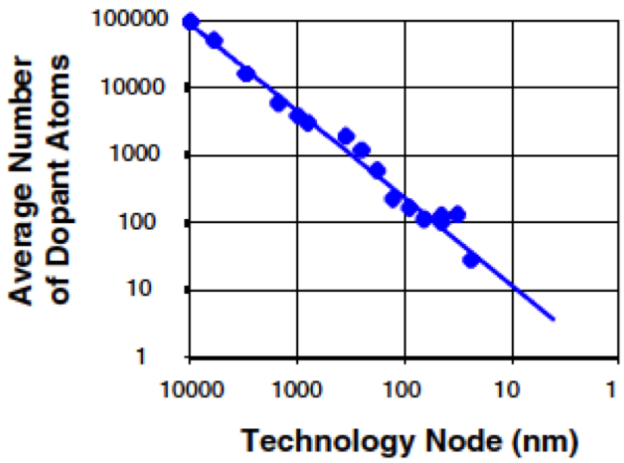

Figure 3.1: Average number of dopant atoms int he channel as a function of technolgoy node [5].

3.1.1 Self-Healing Circuits

A fundamentally different design methodology is required to ensure robust IC performance as transistor scaling and variability increases. Recently, a self-healing design methodology was proposed utilizing a closed loop healing algorithm [111]. We demonstrate a continuation of this work with two representative circuit architectures: a mm-wave transmitter and a high output power PA [112, 113].

3.2 A Self-Healing mm-Wave Power-Mixer in 32 nm CMOS

3.2.1 Introduction

A surge of demand for high-speed communication systems has developed due to the increasing pervasiveness of wireless technology and devices. An important advancement in satisfying the bandwidth requirements of these devices is the development of millimeter-wave (mm-wave) transmitters and receivers able to operate above and beyond 30 GHz. Additionally, non-constant envelope modulation schemes such as quadrature amplitude modulation (QAM) are necessary to fully utilize the available bandwidth in this spectrum. In order to transmit symbols at differing amplitudes, the power amplifiers (PAs) in these communication systems must be operated in significant back-off. Even in constant envelope modulation schemes, the PA may still be operated in back-off to improve linearity. Unfortunately, the backoff efficiency of PAs are usually significantly degraded when operating in backoff. Several class-A PAs have nearly a 25% reduction in efficiency when operating at 6-dB in backoff [114–116]. High energy efficiency is crucial for extending device battery life and improving communication range.

In addition to high energy efficiency, mm-wave PAs require high output power for improving device range and communication reliability. Switching PAs have been developed to achieve high efficiencies and high output power [117, 118], but lack the ability to perform non constant amplitude modulation. Spatial power combining has also been used to achieve high output power by digitally switching a set of power DACs and patch antennas while operating each at high efficiency [117]. However, this scheme requires a large area overhead due to multiple chips and radiating elements. One method of efficient on-chip power combining is the distributed active transformer (DAT) [119]. DAT relies on transformer-based power combining of multiple differential power stages while providing easy supply connections through virtual shorts along the transformer. The transformer also provides an impedance transformation for matching the power elements to the antenna. However, previous architectures have been unable to simultaneously achieve high frequency operation with low area overhead, high backoff efficiency, and high output power, while also being capable of generating complex modulation schemes at high data rates [114, 120–122]. We developed a 19.1 dBm segmented

power-mixer based multi-Gb/s mm-wave transmitter in 32 nm SOI CMOS (Fig. 3.2) [112, 113] [1]. Each power-mixer is operated near saturation to maximize efficiency. To achieve backoff operation, various segments of the power mixer can be turned ON or OFF depending on power requirements. The DAT achieves a 4-to-1 combining while having two easily accessible supply taps. Each power mixer (Fig. 3.3) consists of a Gilbert cell switched-transconductor mixer [123]. A polar modulation scheme is used to supply phase information through the local oscillator (LO) signal and amplitude information is provided by the baseband (BB) signal. A single-ended off-chip LO signal is converted to a differentail signal using an on-chip transformer and routed to each of the lower transistors in the power-mixer. The phase of the LO signal is modulated using an LO drive network based on inverters. BB signals can be operated in either a digital mode (each either ON or OFF), or a fully analog mode. As transistor scaling shrinks the size of transistors, process variations decrease the reliability of transceivers. Moreover, environmental variations can have a detrimental impact on transceivers. For example, the impedance of an antenna in a cellular device can vary due the proximity of a hand. To adapt to these changes, we have designed self-healing capabilities in the system (Fig. 3.4 and 3.5). The transmitter is able to "sense" its performance. If performance is suboptimal, a set of actuators adjusts the operation of the transmitter to recover optimal performance. An on-chip healing microprocessor acts as the "brain" of the self-healing circuitry and automatically "heals" the performance of the chip. Healing sequences can be adjusted for faster coarse optimization, or finer optimization. Sensors consist of couplers with RF power sensing, phase detection, and DC current sensing. Actuators consist of a phase rotator and fine control of transistor biases. The layout of this design is shown in Fig. 3.6.

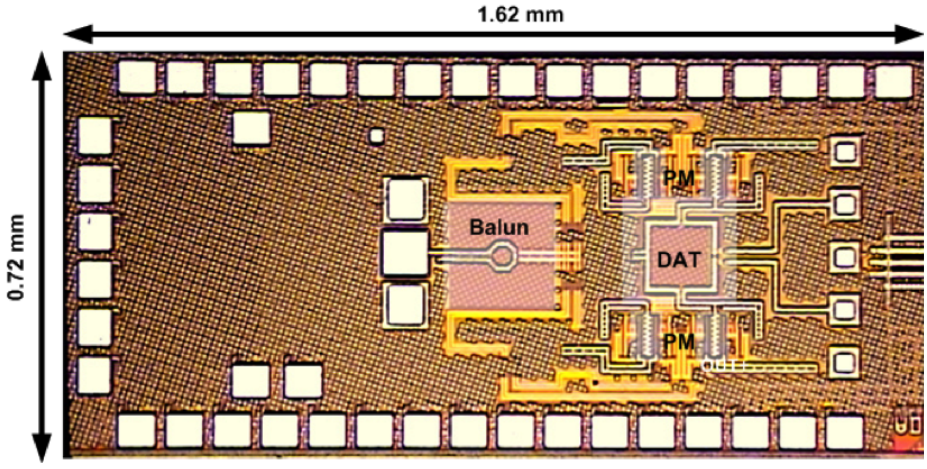

Figure 3.2: Die photograph of a 19.1 dBm segmented power-mixer based multi-Gb/s mm-wave transmitter designed in 32 nm SOI CMOS.

[1]This project would not have been possible without the gracious help of Kaushik Sengupta and Kaushik Dasgupta. The majority of contribution is in sensors, actuators, and self-healing infrastructure.

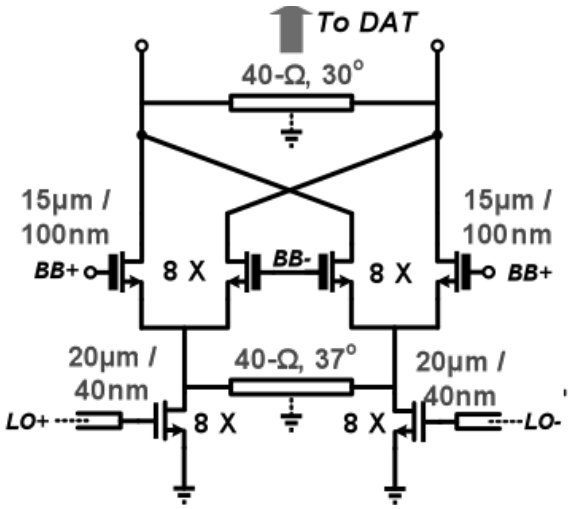

Figure 3.3: Transistor level schematic of power mixer stage.

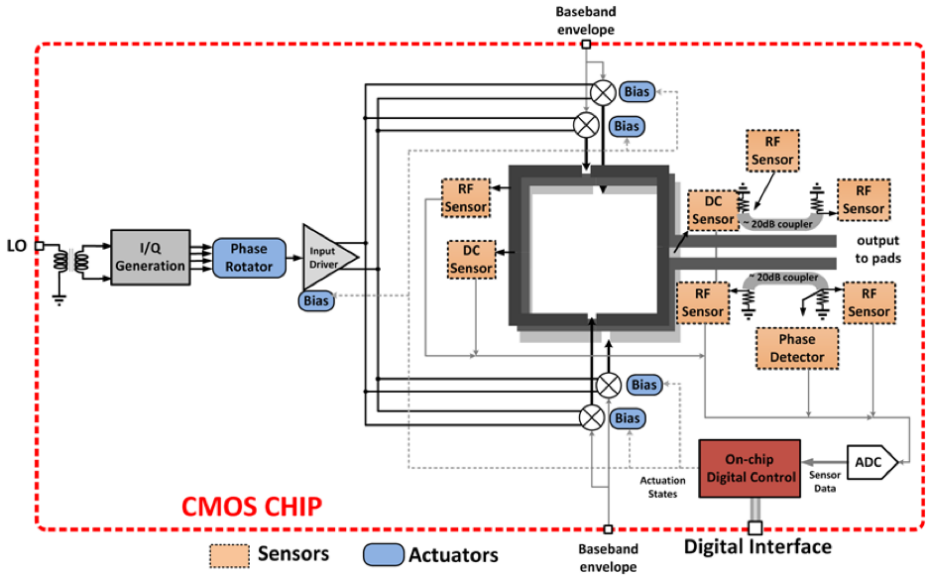

Figure 3.4: Overall architecture of the segmented power mixer-based transmitter with self-healing infrastructure.

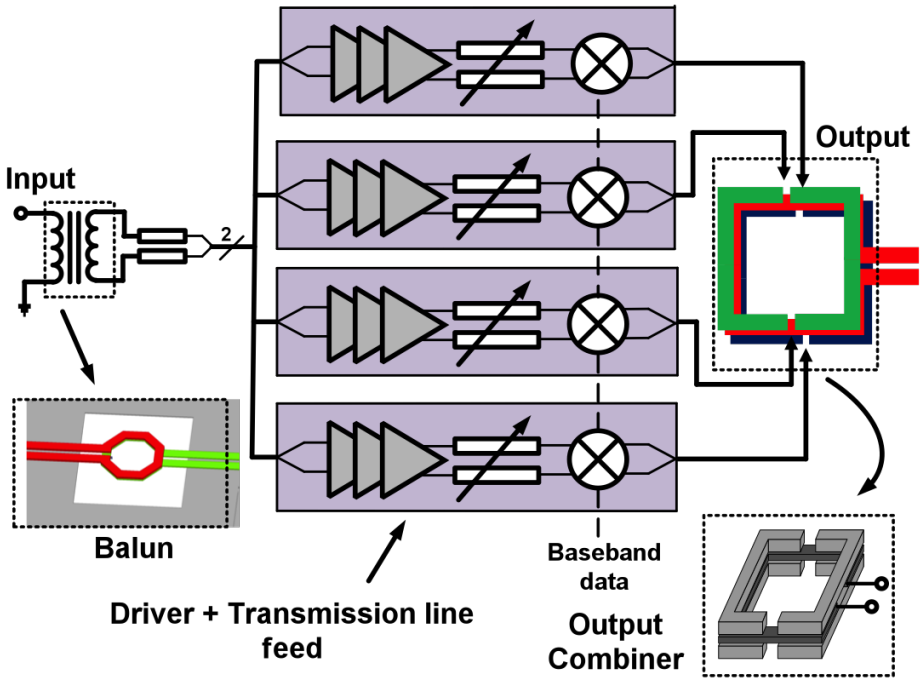

Figure 3.5: Input balun, drivers, DAT, and feeds.

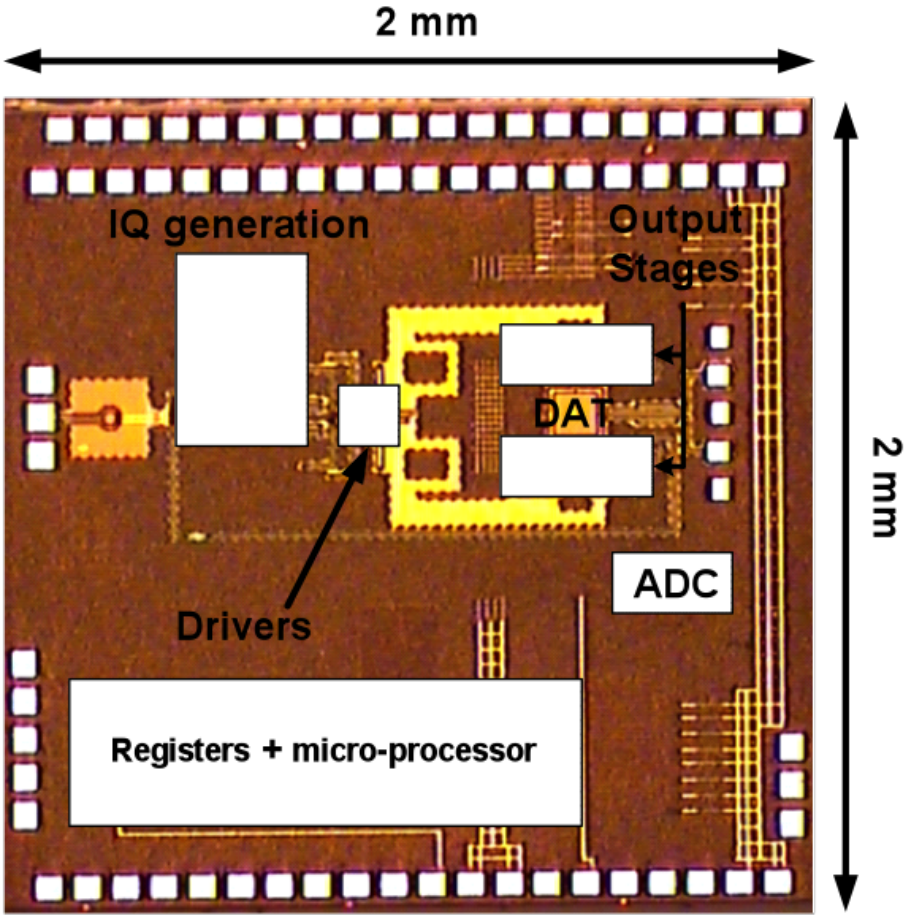

Figure 3.6: Die photo of the segmented power mixer-based transmitter with self-healing infrastructure. The size of the chip is approximately 2 x 2 mm.

3.2.1.1 Digital Backbone

The core of the digital self-healing algorithm is the on-chip controller (Fig. 3.4 and 3.5). The controller is composed of an open source 8086 microprocessor and SRAM module was ported and synthesized by Ben Parker of IBM. The microprocessor interfaces with our custom designed register widget (Fig. 3.8). The microprocessor, SRAM, and register widget contain a high-speed algorithm that can detect the performance or symbol accuracy of the transmitter and compensate for process or environmental variations. A hard-wired optimization algorithm or a custom program can be loaded onto the microprocessor can initiate healing. The register widget inputs sensor information through an ADC. An internal state machine is used to read data from a successive approximation ADC (SARADC) and outputs actuation states through various DACs. The algorithm features an on-chip autonomous mode and an optional off-chip mode (Fig. 3.7).

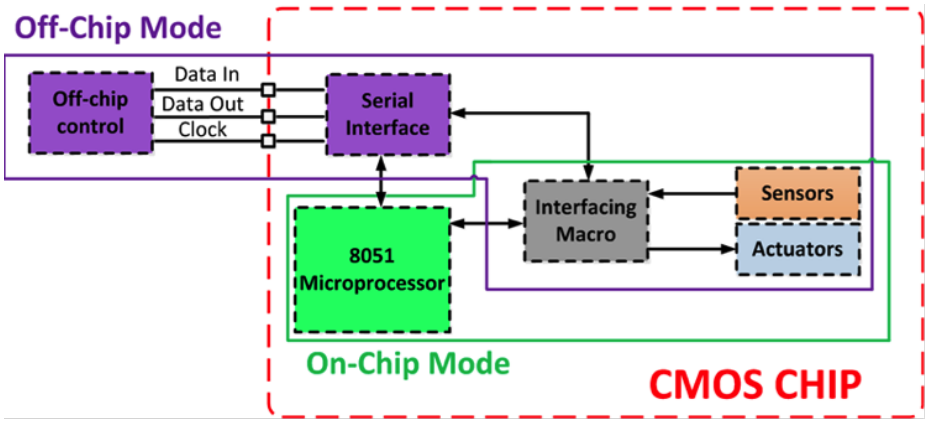

Figure 3.7: Optional off chip self-healing mode.

Measured results for actuation states on the current consumption of the power mixer are shown in Fig. 3.9. To test the microprocessor's functionality, we wanted tune the bias points of transistors in the Gilbert cell of the power mixer and monitor the change in current consumption. In the first test, we programmed DAC settings that interface to each tail transistor in the set of 4 Power Mixers. Each actuator is associated with a separate DAC. We programmed half the range of our DACs in the tail transistor while biasing the middle transistor at 0.6V. The saturated current consumption is consistent with our simulated results. In another test, we varied the bias settings in the middle transistor of each of our 4 Power Mixers.

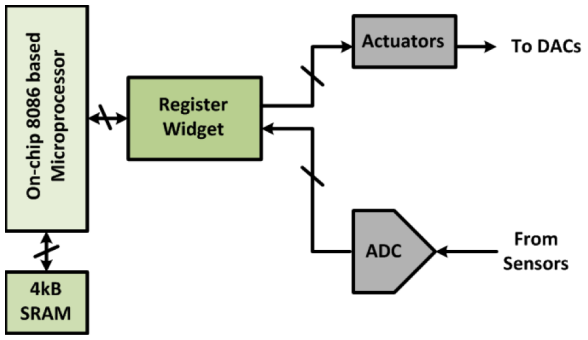

Figure 3.8: Block level diagram of self-healing infrastructure.

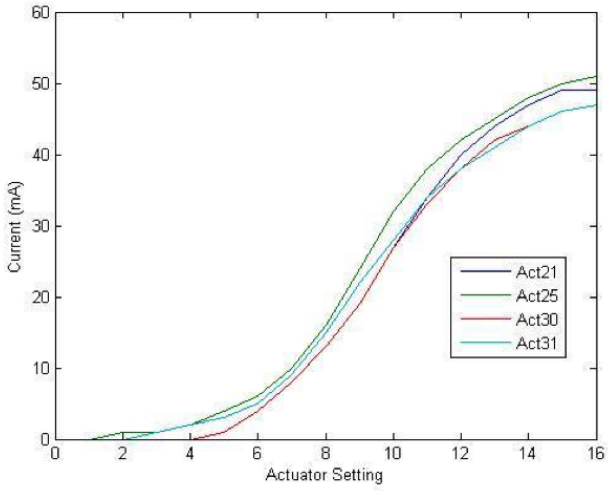

(a)

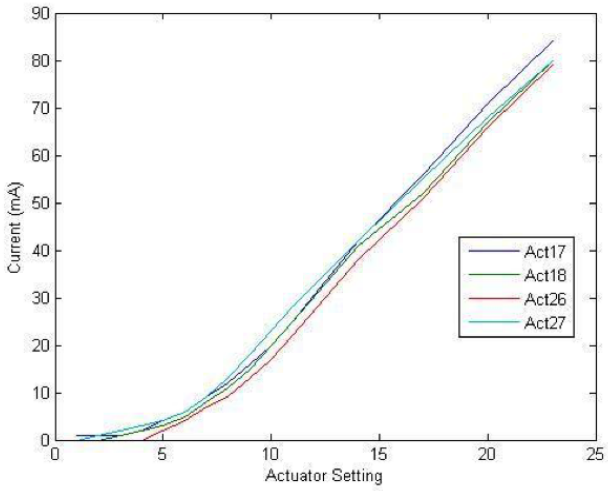

(b)

Figure 3.9: Measured results for DAC control of actuators on the power mixer (a) tail transistors and (b) middle transistors.

3.2.1.2 Symbol Healing

Various sensors and actuators enable symbol healing in the transmitter 3.10. A desired symbol requires accurate phase and amplitude. Phase adjustment is provided to the LO signal through a phase rotator. The amplitude of constellations by biases provided to the power mixers as well as power mixer drivers. The amplitude of the constellation is sensed by the RF power sensor and communicated to the digital core. The phase of the constellation is determined through a phase detector.

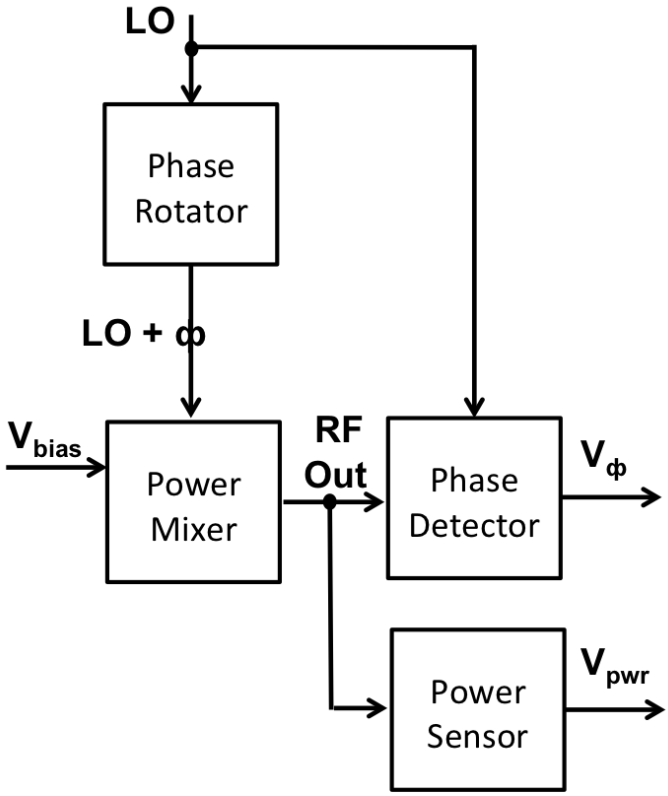

Figure 3.10: A desired constellation requires accurate phase and amplitude. A differential LO signal will pass through a phase rotator as our actuator for phase healing. The amplitude of constellation is adjusted by biases provided to power mixers as well as biases to power mixer drivers. The amplitude of the constellation is sensed by the RF power sensor and communicated to the digital core. The phase of the constellation is determined through a phase detector.

3.2.1.3 20dB Coupler

A pair of 20dB couplers provide information on transmitted and reflected power (Fig. 3.11). Less than 1% of output power is consumed. A total of 4-RF power sensors are placed at differential coupled and isolated ports to detect the amplitude of forward and reflected waves. These provide a bearing on output power and impedance mismatch. The coupling and isolation are shown in Fig. 3.12. The S parameters of the input and output are shown in Fig. 3.13. The couplers have no

discernible effect on signal lines. The layout of the coupler is shown in Fig. 3.14.

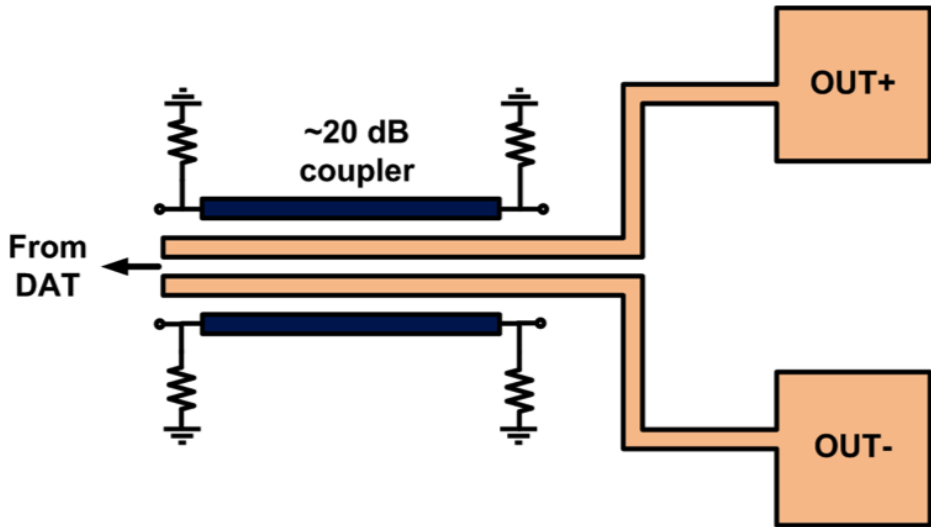

Figure 3.11: RF coupler design for monitoring transmitter ouput and reflected power.

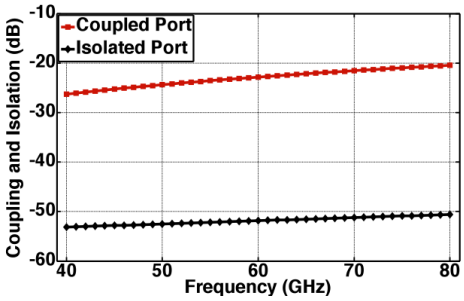

Figure 3.12: Simulated coupling and isolation of RF coupler.

3.2.1.4 RF Power Sensor

The RF voltage sensor (Fig. 3.16) is used to measure the amplitude of a sinusoidal waveform. When combined with the properly terminated 20dB coupled line, the voltage sensor acts as a power sensor. The input transistor is biased near cut-off and acts as a rectifier. Subsequent stages filter and amplify the input amplitude. The input bias (V_{bias}) can be used to trade off sensitivity for dynamic range. To measure the performance of the RF power sensor, test chips are fabricated and measured with a probe output of a calibrated signal generator. The supply biasing is provided using a power supply and the output was measured with a multimeter. The input power was then plotted with respect to the output voltage. The output of two fabricated test chips are shown in Fig. 3.17. In the full transmitter, the output of the RF sensor is provided to the register widget through the SARADC.

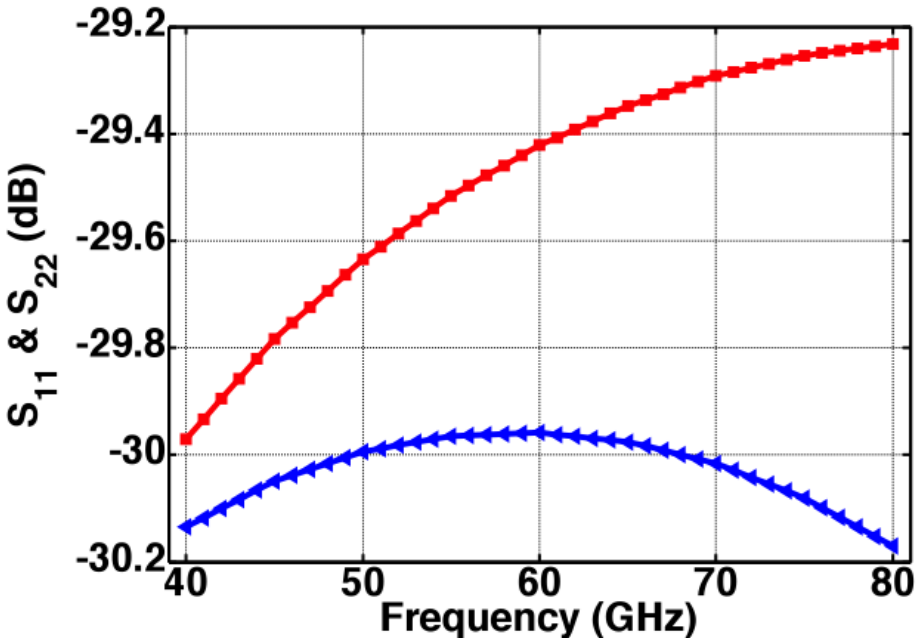

Figure 3.13: S paramters of the couplers show little impact on output traces.

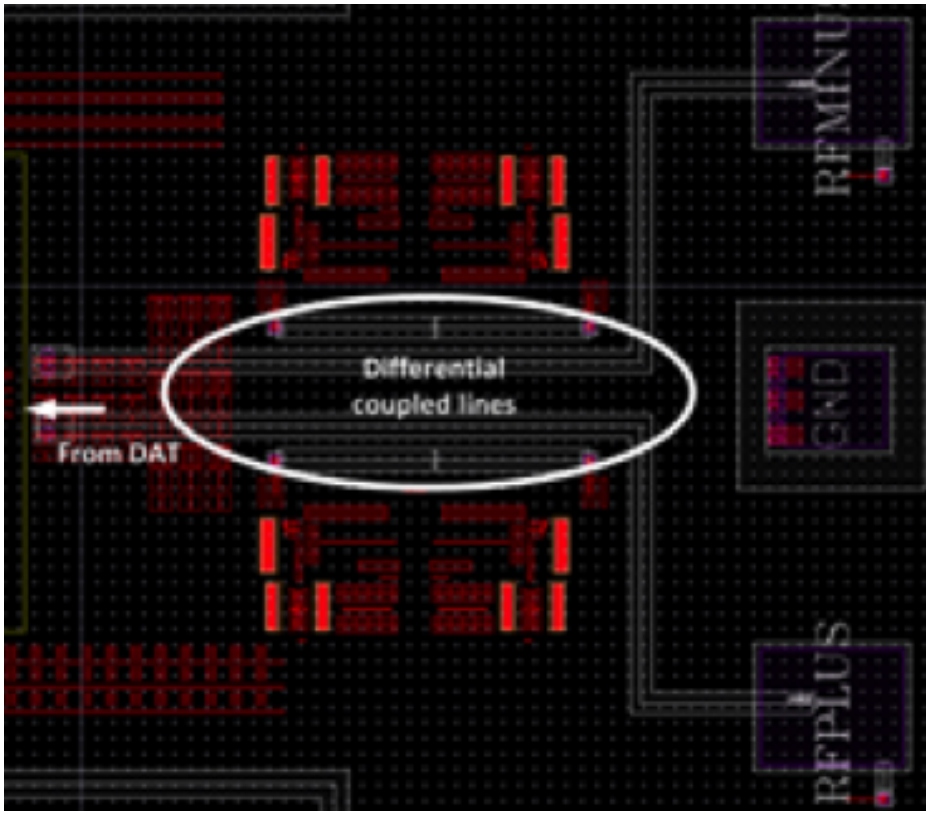

Figure 3.14: RF coupler layout.

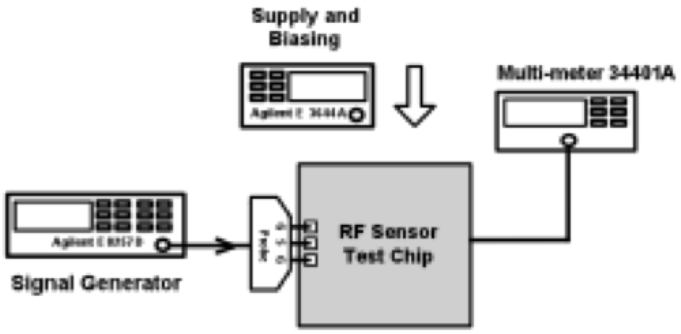

Figure 3.15: RF power sensor test setup. A signal generator provides power at various levels to a test chip through probes. The output of the sensor is measured using a multimeter.

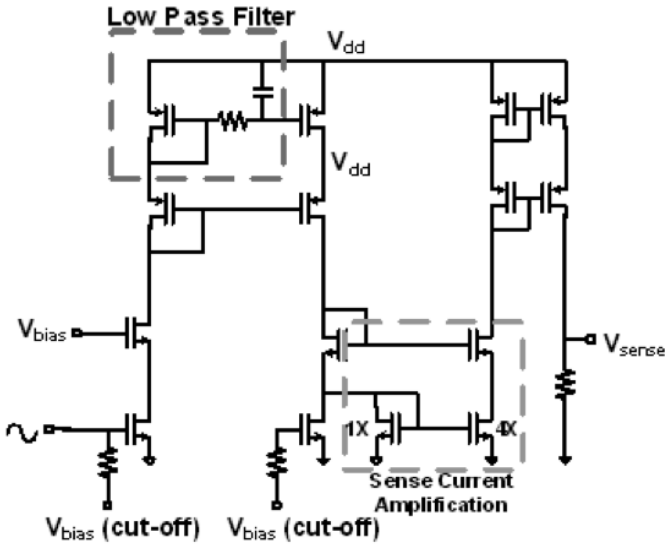

Figure 3.16: The RF power sensor's input consists of a transistor biased at cut-off. The input transistor rectifies the input waveform. After filtering and current mirror amplification, the output is provided to the self-healing controller. The bias of the input transistor can be varied to trade of sensitivity for dynamic range.

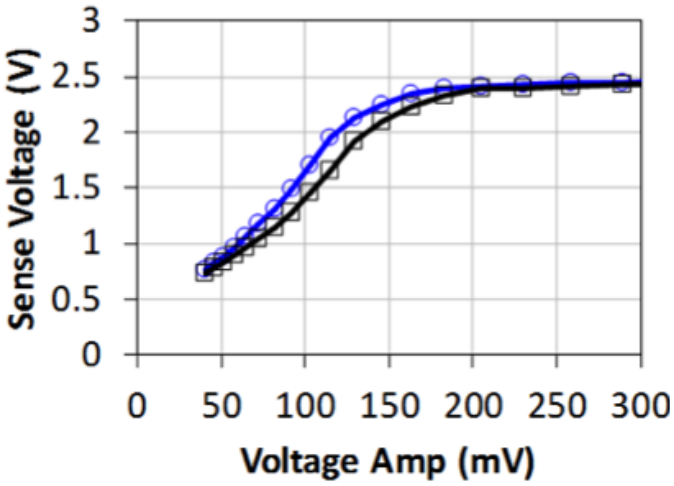

Figure 3.17: The output of two measured chips is shown. The output voltage is correlated with the amplitude of the input signal.

3.2.1.5 DC Current Sensor

An important datum is the DC current consumption of the DAT and power mixers. In particular, the power consumption allows us to determine the efficiency of the transmitter. This is useful in determining which of many states are most optimal in operation. For example, the self-healing infrastructure could toggle between states and choose one which results in minimal DC power consumption. The sensor provides a supply connection for the PA stage (Fig. 3.18). In order to minimize power dissipation, a 1/100X mirroring ratio is used to monitor PA current. In addition, an array of 104 12μm-width transistors are used to minimize voltage drop across the supply transistor. A voltage reference is used to bias the supply transistor gate and ensure only 10 mV of voltage drop across the drain and source. The response from several measured test chips is shown in Fig. 3.20 and 3.19.

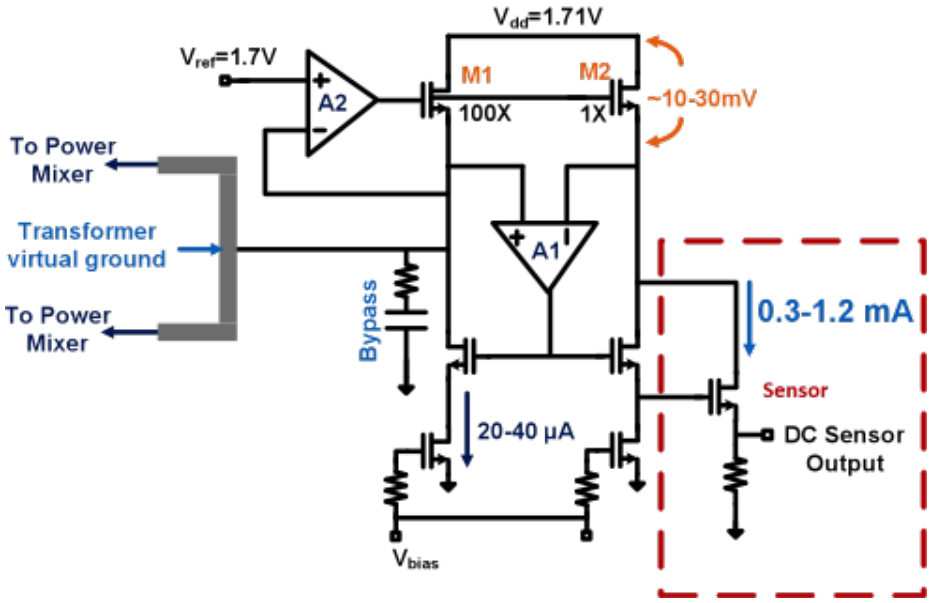

Figure 3.18: Schematic of the DC sensor.

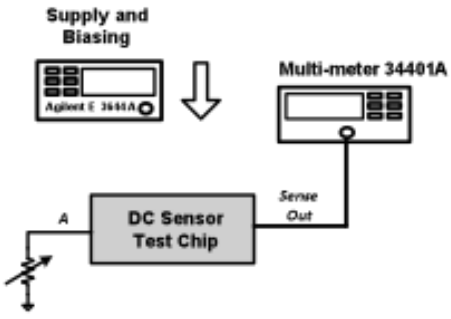

Figure 3.19: Test setup for measuring DC sensor response

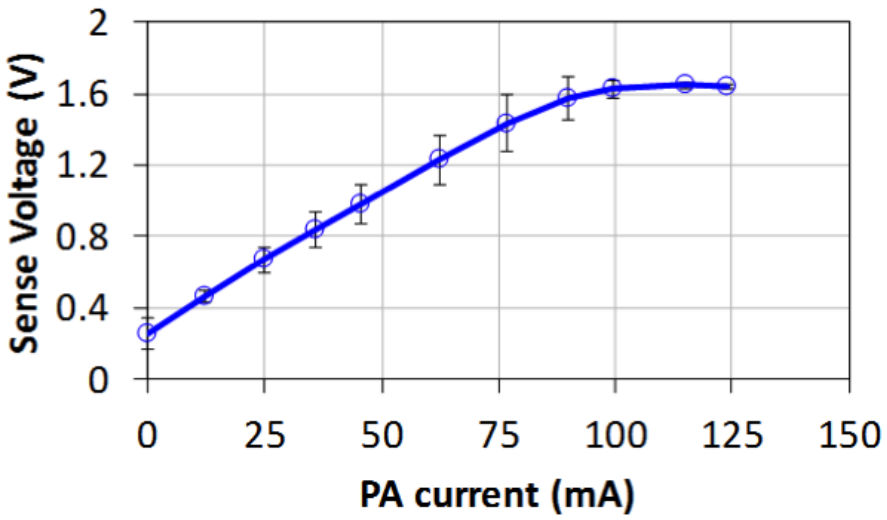

Figure 3.20: Measurement results of DC sensor. The DC sensor was tested under nominal biasing conditions providing a 1.7V V_{dd} to the power mixer. Note that the DC sensor is linear within the operating range of the power mixer (0-100 mA). Standard deviations from multiple chips are also depicted in the figure showing robustness of the sensor.

3.2.1.6 Phase Rotator

In order to properly heal an improperly generated symbol, both phase and amplitude adjustment capabilities must exist. The phase of the output symbol is adjusted by actuating the phase encoding of the LO differential signal. The phase is adjusted using a phase rotator, as seen in Fig. 3.21. This enables high speed phase rotation without the challenges associated with off-chip high-speed modulation. I-Q signals are added with variable levels to generate differing phases. The output of the phase rotator is directly connected to the input of the driver stages. The total size of the layout is 15 x 30 μm (Fig. 3.22).

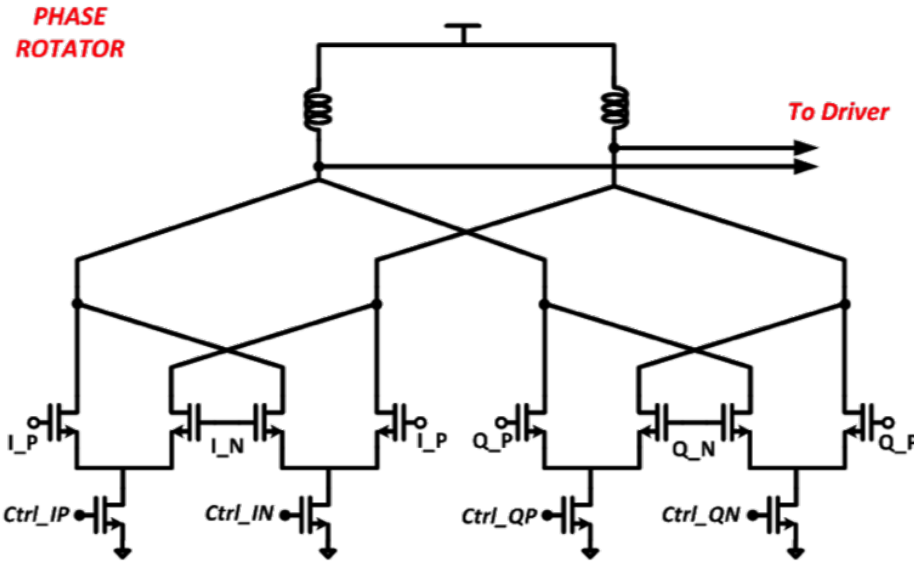

Figure 3.21: Phase rotator to aid in symbol healing. I-Q signals are generated on chip using a transmission line. The weights of I-Q signals are adjusted by adjusting the Ctrl_IP, Ctrl_IN, Ctrl_QP, and Ctrl_QN signals using on-chip power DACs.

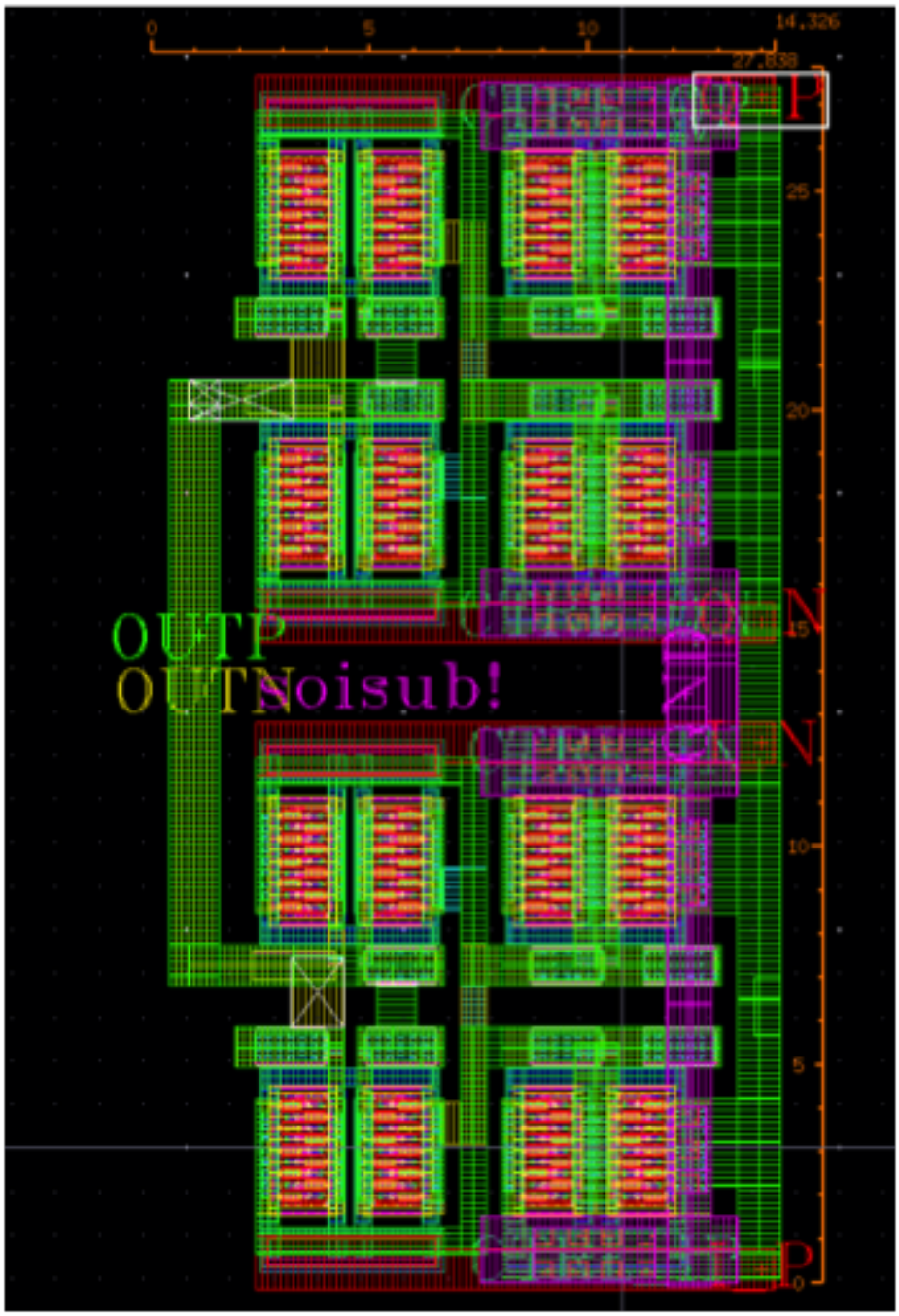

Figure 3.22: The layout of the phase rotator has a total size of 15 x 30 μm.

3.2.1.7 Phase Detection

In order to properly adjust phase, symbol phase mismatch must first be determined (Fig. 3.10). The phase of the power mixer output is sensed using a phase detector (Fig. 3.23. First, the output of the transmitter is mixed with the chip's LO signal. The signal is transmitted through a voltage buffer and low pass filter to generate a DC signal corresponding to the phase offset. The output of the phase detector versus relative phase to the LO is shown in Fig. 3.25). The layout of the phase detector is shown in Fig. 3.24. The phase detector has a minimal power consumption of less than 1 mW.

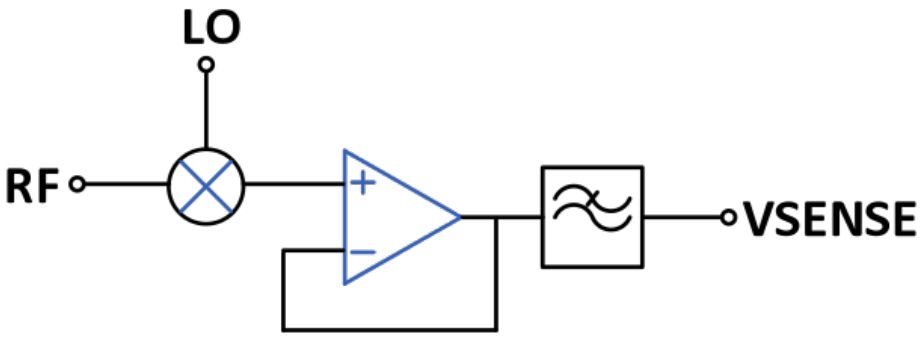

Figure 3.23: The phase detector consists of a transistor mixer of properly terminated, single-ended, 60 GHz LO and RF signals. The DC signal is buffered through a unity feedback op-amp, and filtered through a low-pass filter. The output DC voltage corresponds to the phase offset of the output of the power mixer with the LO. The output is recorded through an ADC and recorded by the self-healing infrastructure.

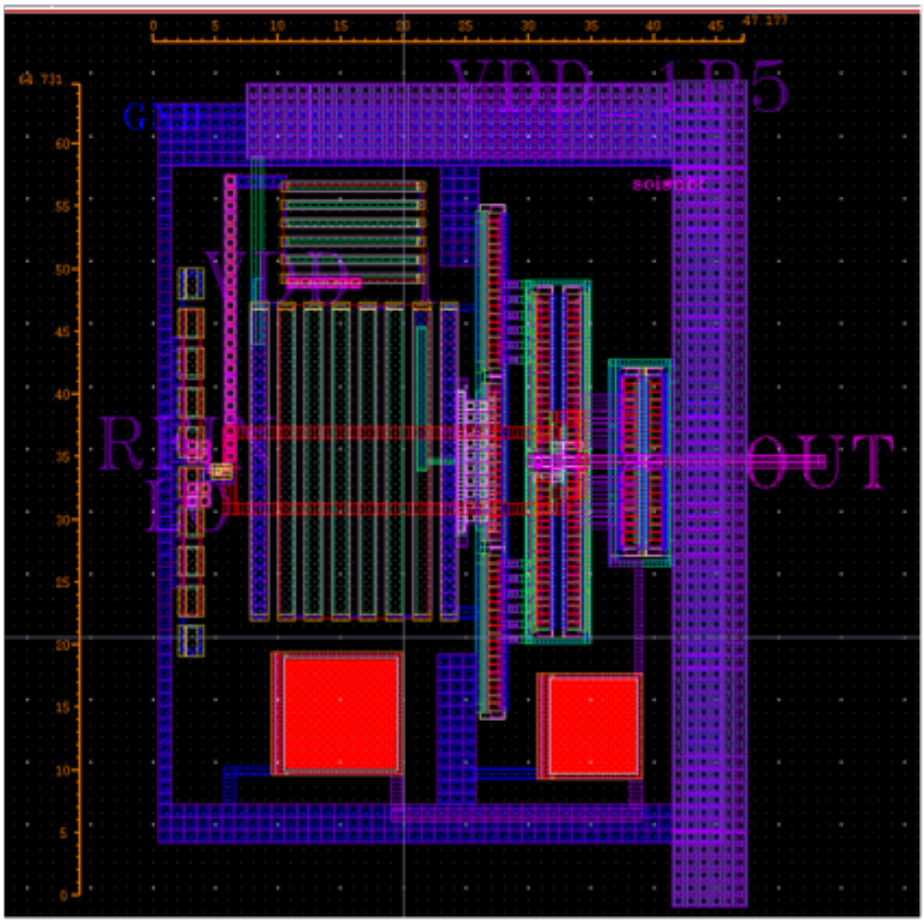

Figure 3.24: Phase detector layout. The total size of the phase detector is approximately 60 x 50 μm.

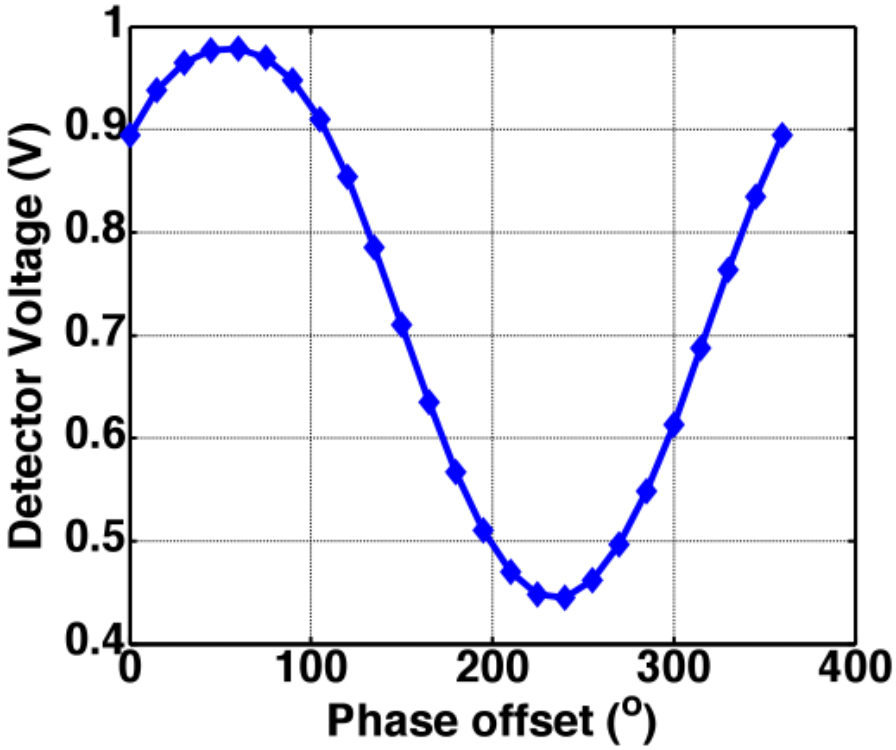

Figure 3.25: Response of phase detector to phase offset. The phase offset is a relative offset between the input of the phase detector and the LO signal.

3.2.2 Variation Resistant Phase Detection Based on Min/Max Algorithm

One important requirement to self-healing infrastructure is that sensors and actuators must themselves be robust enough to handle process variation. The output of the phase detector is simulated in a Monte Carlo simulation across multiple process variation corners (Fig. 3.26). As can be seen, a single output voltage level could correspond to a slew of phase offsets. To mitigate the effect of process variation on the phase detector, a min/max algorithm is used as part of the self-healing procedure. To properly identify the phase response, the phase rotator as actuated over a full 360° rotation. The maximum and minimum output voltages of the phase detector are recorded. This relaxes the requirement of requiring a high number of storage bits, sensing space, and digital processing while adapting for process variation and mismatch. A binary search can be used to decrease heal time. Using the max/min values, a cosine is determined for the phase response of the phase detector. A comparison between predicted phase response and simulated phase response is shown in Fig. 3.27. Using this method, we were able to achieve a standard deviation of approximately 2° in predicted phase variation (Fig. 3.28). An alternative full cosine fit using all values can be used to further improve the predicted accuracy.

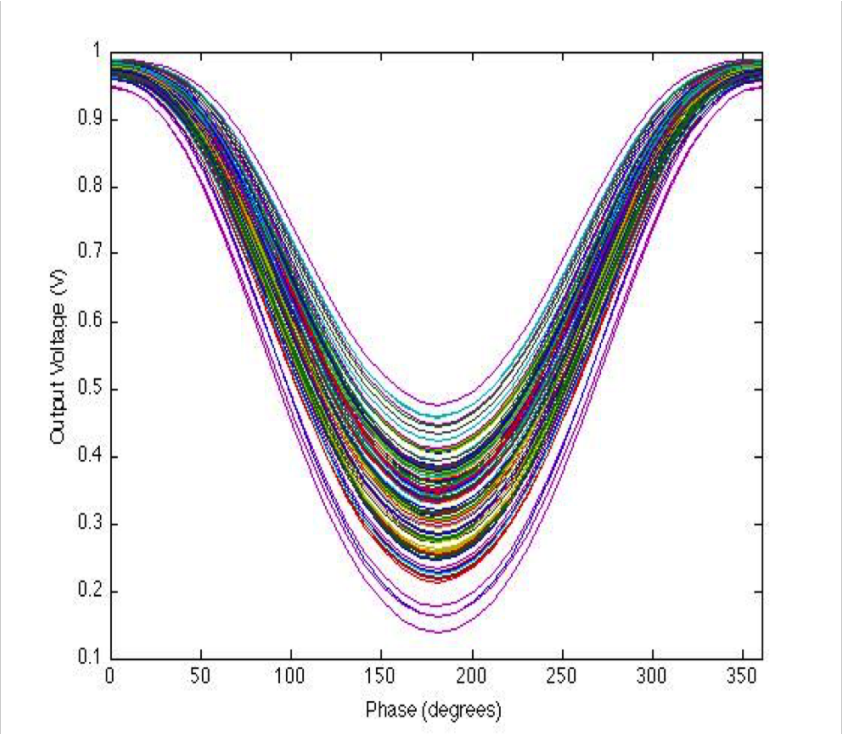

Figure 3.26: Monte Carlo simulation of phase detector output over process corners. This figure shows how process variation could potentially degrade the functionality of the phase detector. The variation is compensated for through a min/max algorithm. A total of 100 iterations were simulated.

3.2.3 Conclusion

We have developed a compact, broad-band, and efficient transmitter based on a dual-primary-based DAT design [112,113]. The transmitter is capable of generating a saturated output power of 19.1 dBm at 51 GHz. The design uses segmented power mixers to enable non-constant envelope modulation at high speeds with high backoff efficiency. We show high speed modulations using ASK, 3-ASK, BPSK, QPSK, and 16-QAM. We have also designed a version of this transmitter with self-healing infrastructure. This enables the transmitter to sense its own performance and tune actuators to optimize performance and reliability.

3.3 A Self-Healing High Power Amplifier in 32nm CMOS

3.3.1 Introduction

A stacked transistor topology can be used to take advantage of an SOI process (Fig. 3.29) [2]. A total of 5 devices can be reliably stacked before buried-oxide (BOX) breakdown. As the number of stacks increases, the maximum supply voltage and output power increases. Additionally, the output

[2]This project would not have been possible without the extremely gracious help of Steve Bowers, Kaushik Dasgupta, and Amir Safaripour. The majority of contribution is in sensors, actuators, and self-healing infrastructure.

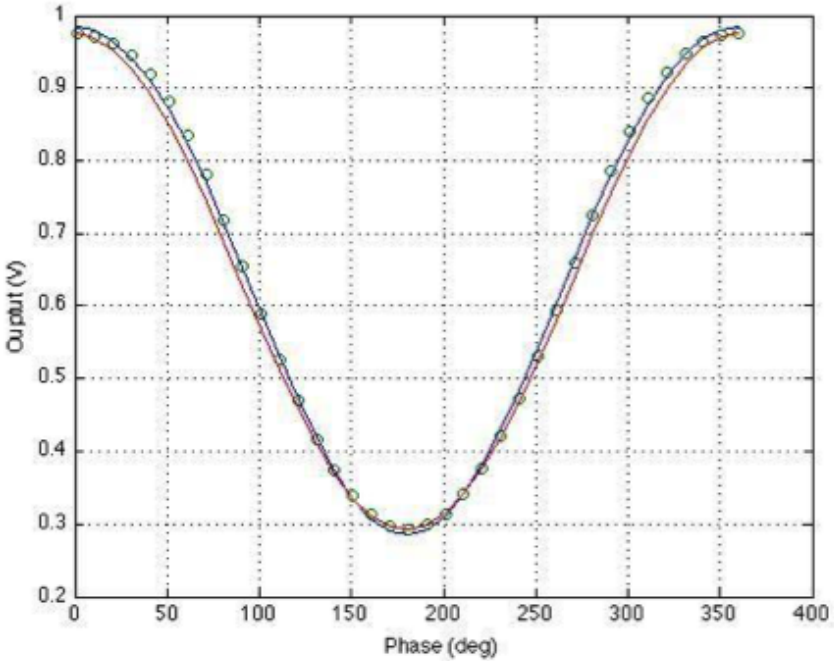

Figure 3.27: Comparison between predicted phase response using the min/max algorithm and simulated response. The min/max algorithm uses only the minimum and maximum output voltages of the phase detector to predict the outputs to other phase offsets. A full cosine fit of several values can be used to further enhance accuracy.

impedance can also be scaled. Plots of output power and impedance scaling are shown in Fig. 3.30. Drain voltage and current scaling are shown in Fig. 3.31. The layout of the architecture is shown in Fig. 3.32.

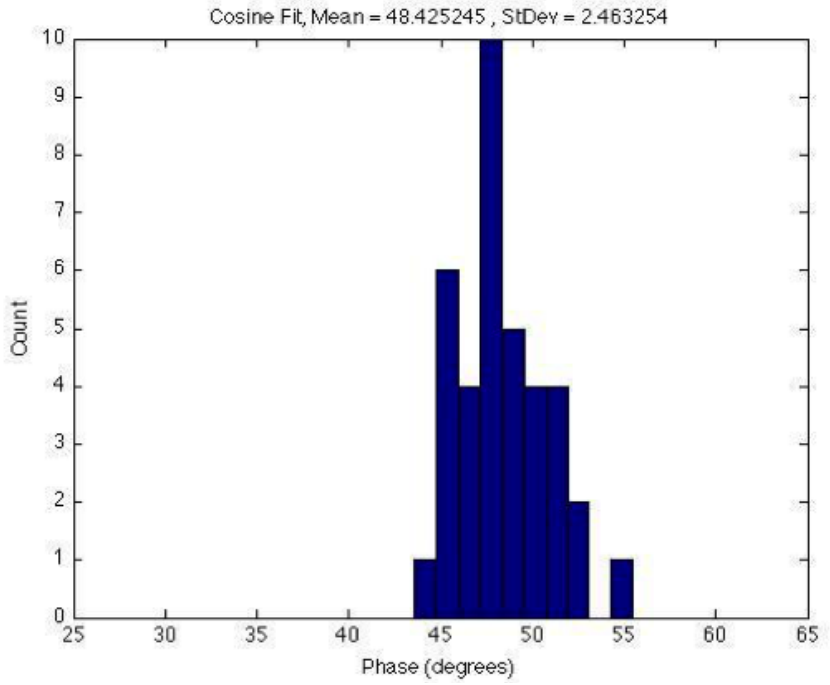

(a)

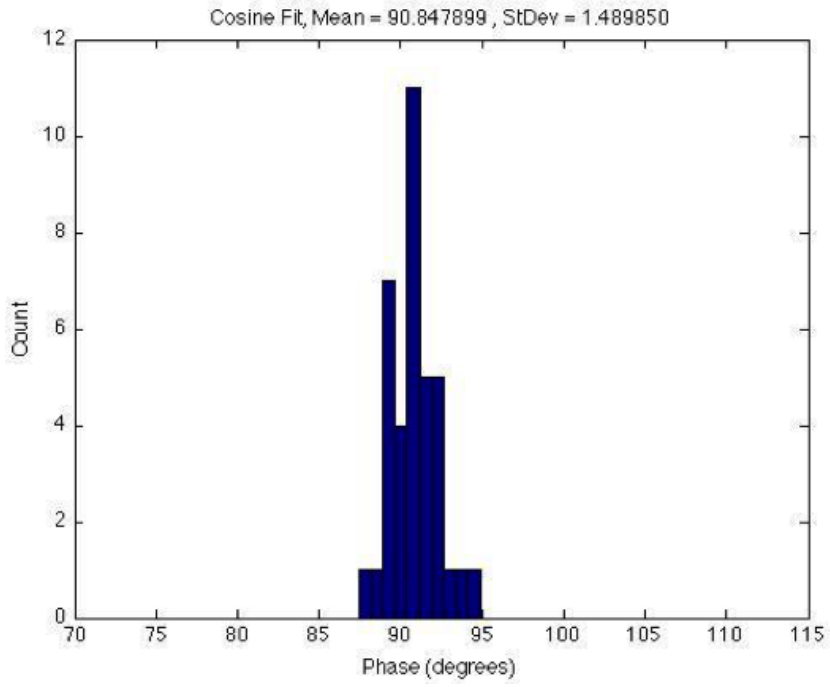

(b)

Figure 3.28: Monte-carlo simulations of phase recovery for (a) 45° and (b) 90°.

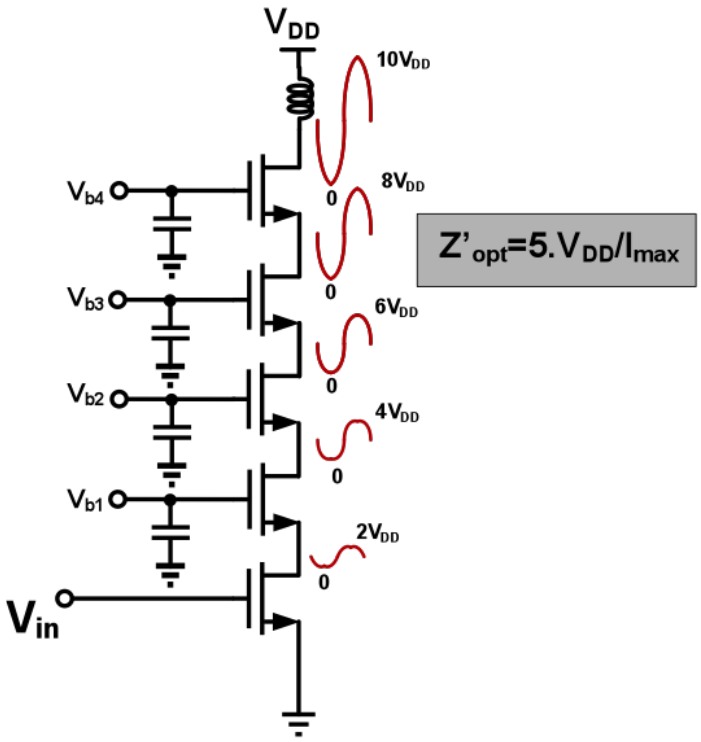

Figure 3.29: Schematic of PA transistor stacking. The drain-source breakdown is 1.4V.

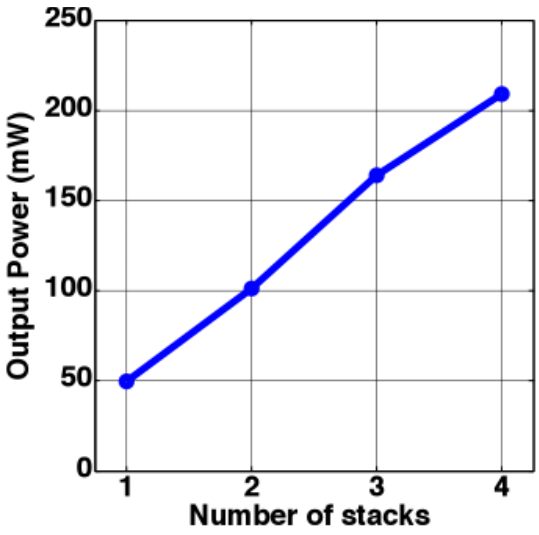

(a)

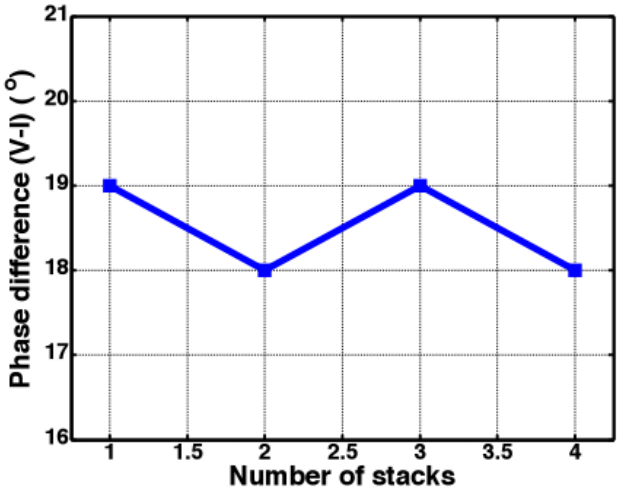

(b)

Figure 3.30: (a) Output power scaling versus transistor stack count. (b) Phase difference between voltage and current at the output.

3.3.2 Self-Healing Infrastructure

The self-healing infrastructure consits of 5 main blocks: scan chain, controller, SARADC Handshaking module, SARADC, a output DACs (Figure 3.33). The infrastructure interfaces with bias actuators and power sensors to adjust for a particular output power/amplitude setting. The on chip algorithm optimizes performance by searching thorugh a bias search space. A flowchart of the output power and optimization algorithm is shown in Fig. 3.34. The on-chip system features an adjustment knob that allows for a trade-off between search space size and healing speed. The infrastructure aso allows for complete external override for fail-safe. Custom actuator DACs are designed to prevent breakdown biasing. An RF sensor with coupler is designed to measure output power. The infrastructure was designed through custom synthesized digital logic from custom designed standard cells (Fig. 3.35). The layout of the digital block is shown in Fig. 3.36.

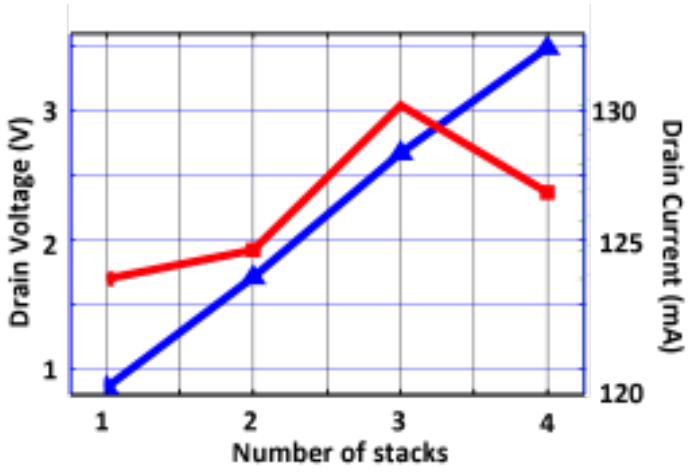

Figure 3.31: Drain voltage scaling and drain current as a funciton of stacking.

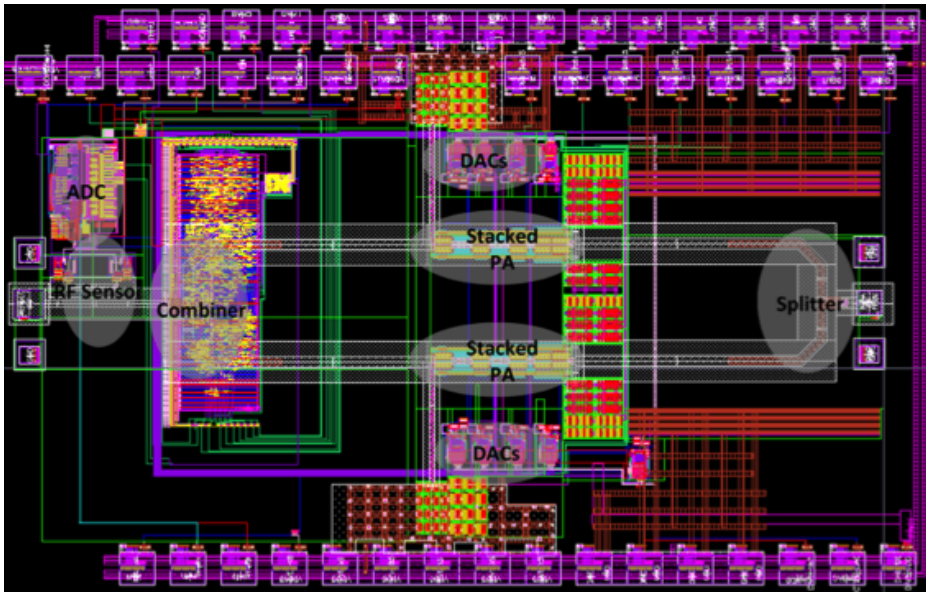

Figure 3.32: Layout of high power PA using transistor stacking.

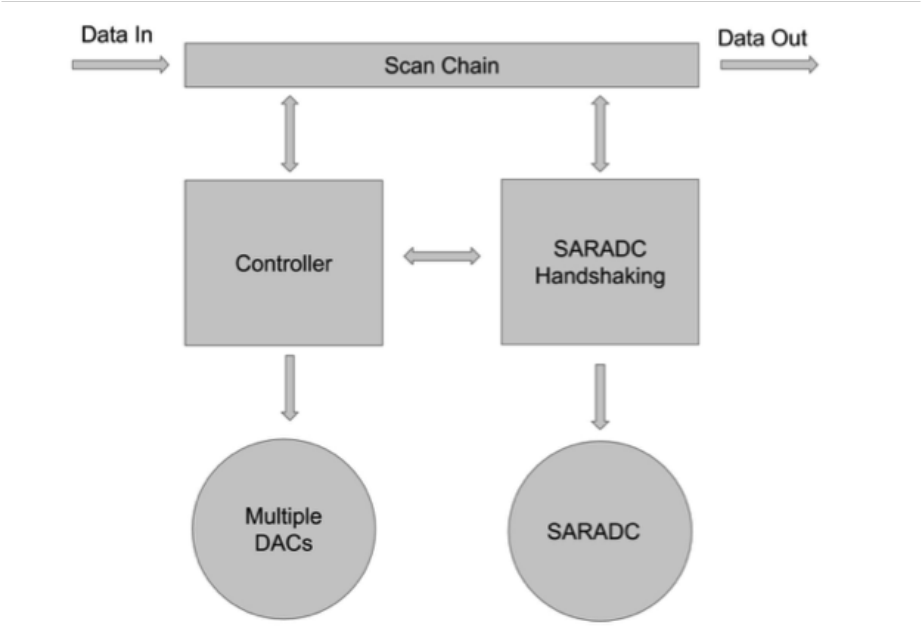

Figure 3.33: Block diagram of self-healing infrastructure.

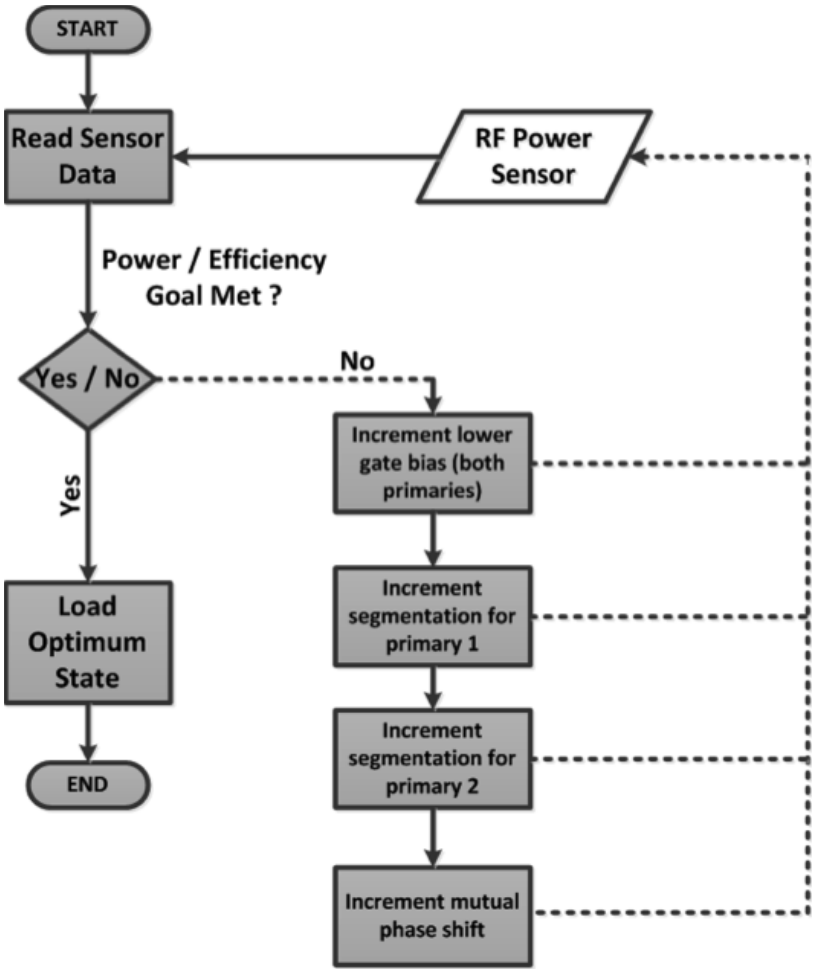

Figure 3.34: Output power and efficiency optimization algorithm.

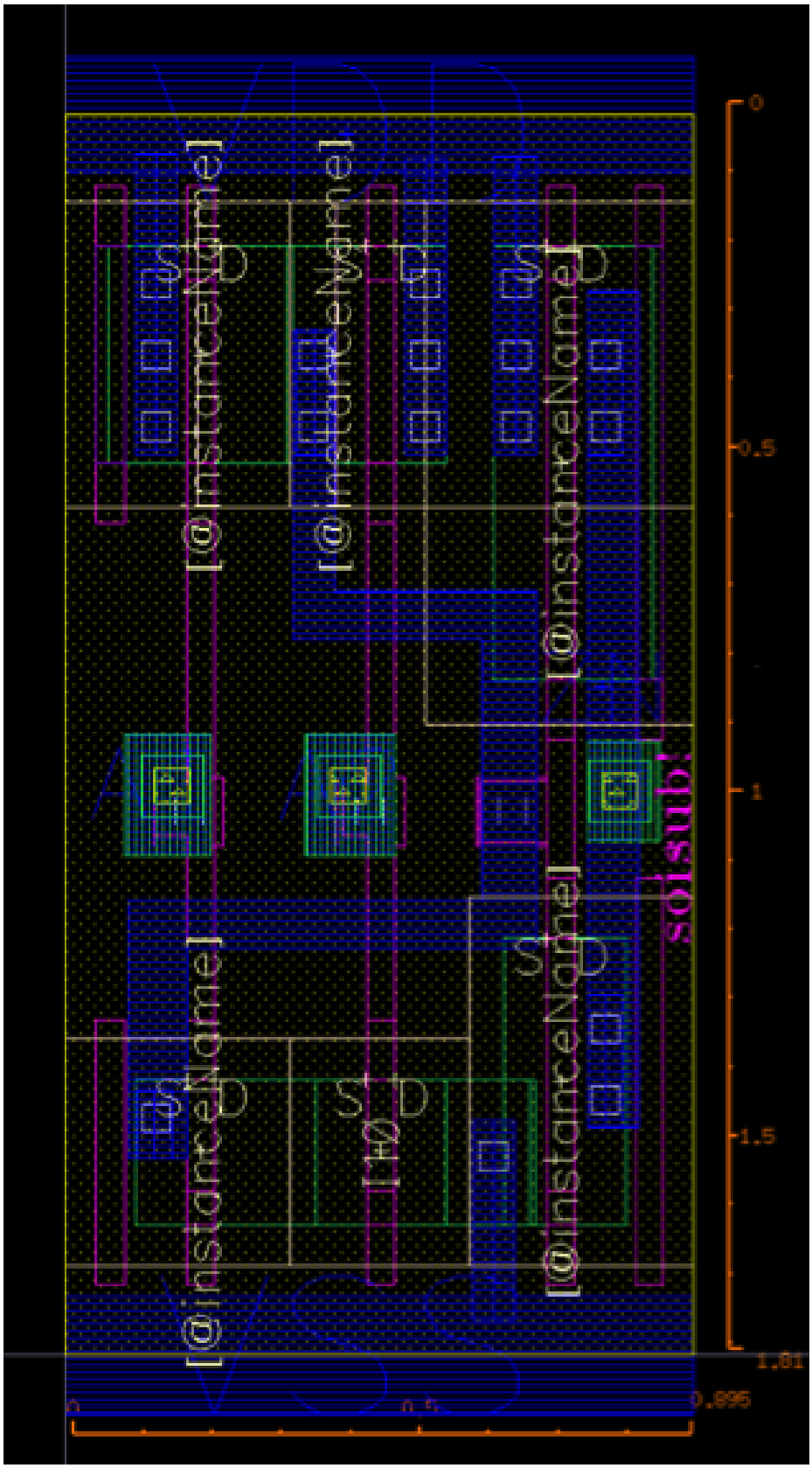

Figure 3.35: An example of a custom designed standard cell. This particular cell is a 2-input AND gate.

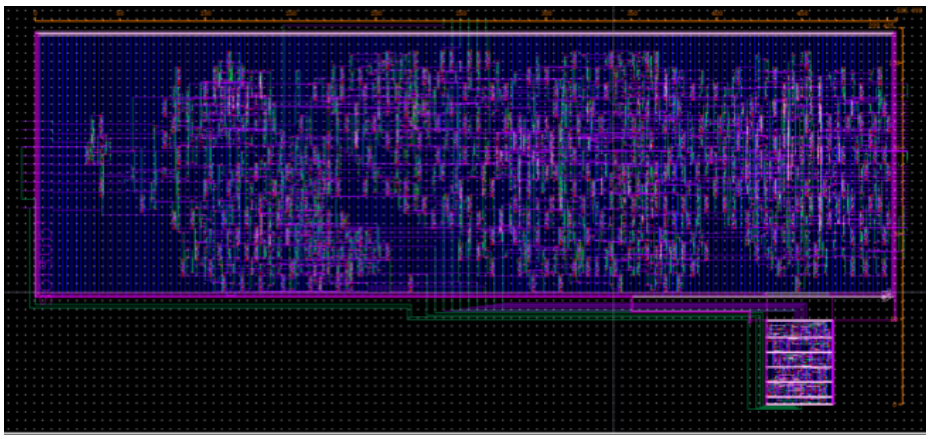

Figure 3.36: Demonstration of custom synthesized digital infrastructure from custom designed digital standard cells.

Chapter 4

Appendix

4.1 Surface Chemistry: Aqueous/Organic Solvent Deposition of TESUD

4.1.1 Motivation

- Establish capability to perform silane surface chemistry on silicon nitride surfaces.
- Perform a functional test of amine-conjugated DNA oligo binding to aldehyde functionalized substrates, including glass and silicon nitride surfaces.

This protocol is taken and modified from the following sources: Hermanson, Greg T., Bioconjugate Techniques (2008), Coupling Agents by Gelest Inc., (2006), and Wu et al., Biosensors and Bioelectronics (2006).

Silicon nitride coated wafers were purchased from University Wafer (150 mm N/Ph (100) 1-20 ohm-cm SSP 650μm with 100nm of nitride). One SiN wafer was scored and cracked into five 3 x 1 sized pieces for this experiment.

4.1.2 Surface Cleaning

1. Rinse the substrates sequentially with acetone, ethanol, and then Millipore DI water. Do not let the surface dry between rinses.
2. Submerge the substrate in the sonicator (filled with water as the medium) for about 1 min.
3. Dry substrate by blowing clean nitrogen gas over the surface.
4. Subject slides to oxygen plasma cleaning for 2.5 min (gas pressure = 0.3 torr, power = 100 W).

4.1.3 Surface Reaction

1. Prepare a solution containing 95% ethanol-5% water solution (v/v) and adjust the pH to 4.5-5.5 with glacial acetic acid.
2. Dissolve triethoxysilyludecanal (TESUD) in the acidic water/ethanol solution with stirring to a final concentration of 2% (v/v). Allow hydrolysis to occur for 5 min at room temperature to form reactive silanols.
3. Dip glass substrates into silane solution and incubate for 2 h.
4. Wash the glass slides three times with ethanol or the water/ethanol mixture to remove excess silane compound.
5. Cure the silane-modified glass slide by incubation at 110°C for 30 min.

4.2 DNA Conjugation: Immobilization of Thiol-functionalized DNA to Amino-coated Glass Substrates

4.2.1 Motivation

- Establish capability to perform surface chemistry on glass slides.
- Demonstrate protocol for immobilizing thiol-modified DNA oligos to an amino-functionalized glass surface

This protocol is modified from Wu et al., Biosensors and Bioelectronics (2006).

4.2.2 Surface Reaction

1. Dissolve sulfo-SMCC at a concentration of 0.2 mg/mL in 50mM sodium borate buffer (pH=7.5). Incubate amino-modified glass slides in solution for 2 h. Room temp.
2. Rinse 1x with fresh sodium borate buffer, then 3x with ddH_2O.
3. Measure contact angle of the SMCC modified surface and compare to a non-modified surface.

4.2.3 DNA Immobilization

1. Treat oligo with 10mM DTT for 15 min.
2. Pass oligo + DTT through a G-25 spin column to remove the DTT.

3. Spot 1mL of 3x SSC containing oligomer (use range of 1000, 500, 250, and 100 ng/mL DNA) on glass slide. Place slides on the rack in an empty pipette tip box, fill bottom of box with 40mL of 3x SSC and incubate for 6 h at room temperature.

4. Immerse slides in a solution of 50mM 2-mercaptoethanol in 50mM sodium phosphate buffer (pH=6.6) for 30 min to block unreacted surface-bound maleimide groups.

5. Rinse slides 3x with 150mM phosphate buffer saline (PBS), then 3x with ddH_2O.

6. Immediately place slides in 4x SSC with 0.1 wt% SDS solution, heat to 50°C for 30 min to remove non-specifically bound DNA probes. Rinse with ddH_2O 3x and dry by centrifugation.

4.2.4 Hybridization

1. Prepare hybridization solution (50mL total volume): 4x SSC, 0.2 mg/mL BSA, 100 mg/mL salmon sperm DNA, 0.1% SDS, and 1.5mg of Cy3-labelled DNA. For negative control, include only 4x SSC. [Or, for 50 mL total volume add the following: 32.5 mL 5x SSC, 7.5mL dH_20, 7.5 mL Cy3-labelled DNA, 1mL of 1% BSA stock (in 3x SSC), 0.5mL salmon DNA, and 1 mL of 10% SDS.]

2. Heat hybridization solution to 100°C for 2 min. Cool in 30°C water bath for 30 s.

3. Place 45 mL hybridization solution onto slide, and cover with coverslip. Incubate overnight (12 h) at 55°C in a pipette tip box (lower part filled with 40mL of 3x SSC and slide placed over perforated surface). Protect from light.

4. Wash in 250 mL of 0.5x SSC with 0.01% SDS on orbital shaker for 2 min.

5. Wash in 250 mL of 0.5x SSC on shaker for 3 min.

6. Wash in 250 mL of 0.1x SSC on shaker for 3 min. Repeat this wash two additional times, but for 1 min.

7. Wash in 250 mL of 0.01x SSC for 5 seconds, and dry immediately (by compressed air).

8. Scan slide with a fluorescence slide scanner.

4.3 DNA Conjugation: Immobilization of Amine-functionalized DNA to Aldehyde-Coated Glass Substrates

4.3.1 Motivation

- Improve the efficiency of amine-conjugated DNA binding to aldehyde slides.

- Include a bake step after printing to help stabilize the Schiff base bond.
- Include a hybridization step to visualize DNA bound to the surface, since $NaBH_4$ treatment destroys the Cy3 fluorophore.

This protocol is modified from ArrayIt's website [124].

4.3.2 DNA Immobilization

1. Dilute 100 mM DNA oligo into 1x printing buffer (ArrayIt).
2. Print DNA onto aldehyde slides (ArrayIt or VWR) with the humidity set at 60%.
3. Bake the slides for 30 min at 80°.
4. Allow the slides to set overnight at room temperature and humidity $< 30\%$.
5. Image slides a fluorescence scanner.
6. Rinse the slides in 0.1% SDS twice (2 min) and once in water (2 min). Finally, rinse in water for 2 min with vigorous agitation.
7. Reduce for 5 min with gentle mixing in 500 mL sodium borohydride reducing solution (dissolve 1.5 g $NaBH_4$ in 350 mL phosphate buffered saline (PBS) and add 150 mL 100% ethanol after the $NaBH_4$ dissolves to improve reducing efficiency).
8. Rinse 2 times for 1 min each in 500 mL dH_2O, rinse 2 times for 1 min each in 500 mL 0.1% SDS 3x with 150 mM phosphate buffer saline (PBS), and then rinse 3x with ddH_2O.
9. Image slides with a fluorescence scanner.

4.3.3 Hybridization

1. Prepare hybridization solution (50mL total volume): 5x SSC, 0.2 mg/mL BSA, 0.1% SDS, and 1.5 mg of Cy3-labelled DNA. (For 500 mL total volume add the following: 100 mL 20x SSC, 384 mL dH_20, 12mL Cy3-labelled DNA, 8 mL of 10 mg/mL BSA stock, and 4 mL of 10% SDS).
2. Heat hybridization solution to 61°C for 2 min.
3. Place 50 mL hybridization solution onto slide, and cover with coverslip.
4. Incubate overnight (12 h) at 55°C in a pipette tip box (lower part filled with 40mL of 3x SSC and slide placed over perforated surface). Protect from light.

5. Wash in 250 mL of 0.5x SSC with 0.01% SDS on orbital shaker for 2 min.
6. Wash in 250 mL of 0.5x SSC on shaker for 3 min.
7. Wash in 250 mL of 0.1x SSC on shaker for 3 min. Repeat this wash two additional times, but for 1 min.
8. Wash in 250 mL of 0.01x SSC for 5 seconds, and dry immediately (by compressed air).
9. Scan slide with a fluorescence scanner.

4.4 Detailed DNA Functionalization of IC

4.4.1 Materials

Hybridization Buffer

Target DNA at desired concentration

1X PBS, 1 mg/mL BSA, 5 nM EDTA

0.1% Tween-20

0.1 mg/mL salmon sperm DNA

Bead Binding and Washing Buffer

5 mM Tris-HCl pH 7.5

0.5 mM EDTA

1M NaCl

Stringent Wash Buffer 1

Stringent Wash Buffer 2

4.4.2 Protocol

1. Rinse 3x with 200 μL of hybridization buffer, do not allow to dry.
2. Let the last rinse incubate for 15 min.
3. While incubation occurs, prepare DNA hybridization buffer
4. Add 200μL of hybridization mix and incubate for 30 min.
5. When incubation occurs, prepare bead solution.
   (a) Vortex Dynal Bead vial for 30 sec.
   (b) 100 μL of bead solution=10 μL of strep mag bangs beads + 90 μL of 1x Binding Washing Buffer

(c) Vortex for 30 sec, then magnetically separate.

(d) Aspirate out solution.

(e) Repeat previous 3 steps two additional times.

6. Add 250 μL of wash buffer 1 to well, wait 2.5 min

   (a) 1mL of wash buffer = 900 μL of water + 100 μL of Arrayit 10x stock.

7. Repeat previous step.

8. Rinse with 200-300μL of Binding and Washing buffer 3-5 times.

9. Add 100μL of bead solution to well and sit for 20 min.

10. Place a piece of saran wrap over the well.

11. Cut off the cap of a micro-centrifuge tube and place it on the well.

12. Flip over the slide. Make sure there are no air bubbles in the well. Wait at least 15 min for the beads to settle to the cap.

13. Without flipping over, remove cap and pour out solution.

4.5 Experimental Details of SPION-CpG Construct Analysis

Ultrasonication was performed using a QSONICA Sonicator Q700 (QSONICA, Newtown, CT, USA) equipped with a cup horn cooled with running water from the sink. Super paramagnetic iron oxide nanoparticles (30 nm, catalogue #SOR-30) were purchased from Ocean Nanotech, Springdale, AR, USA. Silane-PEG-NH_2 (MW = 2000, Catalogue #PG2-AMSL-2k) was purchased from NANOCS. Dithiotheritol (DTT) was purchased from VWR. Fully phosphorothioated CpG oligonucleotides bearing a terminal dithiol (5-HO-C6-SS-C6- T*A*A*A*C*G*T *T*A*T*A*A *C*G*T*T*A*T*G *A*C*G*T*C*A*T* -3) (RSS-CpG) was provided by the DNA/RNA Core Facility at Beckman Research Institute at City of Hope. Sulfosuccinimidyl 6-(3-[2-pyridyldithio]-propionamido)hexanoate (Sulfo-LC-SPDP) was purchased from ProteoChem (catalogue #c1118). Illustra NAP-25 columns (catalogue #17-0852-01) were purchased from GE Healthcare. All other chemicals and reagents were from standard commercial sources. N9 cells were cultured in Dulbecco's Modified Eagle Medium (with high glucose, L-glutamine, sodium pyruvate) supplemented with 10% fetal bovine serum (FBS), HEPES (0.01 M), penicillin (100 U mL^{-1}), and streptomycin (100 μg mL^{-1}) and incubated at 37 °C in a humidified 5% CO2 atmosphere. For movement experiments, cells were cultured in glassbottom dishes (MatTek Corporation, catalogue # P35G-0-14-C). Coverslip removal fluid (catalogue # P DCF OS 30) was obtained from MatTek.

4.5.1 SPION-CpG Synthesis

Silane-PEG-NH_2 (29 eq., 17 mM) and Sulfo-LC-SPDP (17 eq., 10 mM) were dissolved in deionized water and stirred for 2 h at room temperature. Meanwhile, RSS-CpG (1 eq.) was dissolved in deionized water containing at least 2.5 mM DTT and stirred for 2 h at room temperature. DTT-treated RSS-CpG was then passed through a nap-25 column (GE Healthcare) in order to remove excess DTT. The CpG solution was then added to the silane-PEG-NH_2-containing reaction and heated in a 60°C oil bath for at least 2 h. After 2 h, the reaction was isopropanol-precipitated, dialyzed against deionized water using a < 3.5 kD MWCO membrane, and lyophilized.

The lyophilized material was dissolved in deionized water and diluted to an effective CpG concentration of 2 mg mL^{-1} based on UV absorbance at 260 nm (RSSCpG ε_{260nm} = 261,900 L mol^{-1} cm^{-1}). Then SPIONs (25 mg mL^{-1} in chloroform) were combined with the product stock solution in a 1:1 mass ratio (SPION:CpG). The mixture was rotated for 10 min and distributed into 1.5 mL microcentrifuge tubes with < 1 mL in each. To disperse the SPIONs, the sample tubes were ultrasonicated for a process time of 4 h (80 amplitude, 15 s on, 15 s off). The SPION-CpG conjugates were then dialyzed (100 kD MWCO) against deionized water. After dialysis, the samples were diluted to a final concentration of 1 mg mL^{-1} SPIONs and 1 mg mL^{-1} RSSCpG (assuming no loss) using deionized water. During synthesis of SPION-CpG, discoloration of sample tubes and sedimentation upon dialysis membranes was observed, indicating that some of the material was lost. However, it was not feasible to quantify the SPION loss on these surfaces. Similarly, the amount of CpG lost during SPION-CpG synthesis is also difficult to quantify. Therefore as an approximation, the concentrations reported in subsequent experiments assumed no loss of SPIONs and no loss of CpG. At worst, when using this approximation we underestimated the immunostimulatory potential and cell uptake efficiency of SPION-CpG.

4.5.2 Mass Spectroscopy

Using 3kD MWCO centrifugal spin filters (Amicon Ultra 0.5 mL, catalogue # UFC500324, EMD Millipore), crude from the RSSCpG reduction reaction was washed with an ammonium acetateacetic acid buffer (pH = 4.5) and deionized water for desalting. The sample was introduced by nanoelectrospray into a Thermo LTQ-FT operated in negative ion mode under manual control. Ions were detected in the ICR cell at resolution 100,000 (at m/z 400).

4.5.3 NFkB Activity Assay

RAW-Blue mouse macrophage reporter cells (Invivogen) were cultured at 5000 cells per well (using a 96-well plate; 6 repeat per group). Cells were treated with 10 μL of RSSCpG, SPION-CpG, or water for 16 h. Both RSSCpG and SPION-CpG treated wells had the same final CpG concentration

(0.1 mg mL^{-1}). The level of secreted embryonic alkaline phosphatase (SEAP) was quantified by incubating 10 μL of supernatant with 190 μL QuantiBlue substrate (InvivoGen) for 1 h and reading absorption at 620 nm using DTX 880 Multimode Detector (Beckman Coulter). QuantiBlue substrate was prepared by mixing one pouch of QUANTI-Blue in 100 mL of deionized water. The solution was then filtered using a 0.2 μm membrane. QuantiBlue substrate was warmed at 37 °C prior to use.

4.5.4 Physical Characterizations

Cytotoxicity assessment was performed using the LIVE/DEAD staining assay (Invitrogen). N9 microglia cells seeded at 9.6 x 104 cells per well in a glass bottom cell culture dish were grown to 80% confluence. For each viability assay, the cells were washed with PBS, treated with the SPION-CpG conjugates and incubated for 12 h. After exposure to the different SPIONs, the cells were rinsed with PBS and stained with calcein-AM and ethidium homodimer (EthD-1 or EthD-2). The dyes were mixed together and appropriately diluted so that the effective working solution contains 2 μM of calcein-AM and 4 μM of ethidium homodimer which was then directly added to cells following manufacturer's protocol. After incubation with the dye, the cells were treated with fixative (either glutaraldehyde for post-movement SEM samples or paraformaldehyde) and imaged.

Light microscopy images were obtained on several instruments: Nikon Eclipse TS100 microscope equipped with Infinity2 camera (Nikon Instruments Inc., USA), Nikon Eclipse TE2000-U Inverted Fluorescence microscope (Nikon Instruments Inc., USA), Zeiss Axio Observer Z1 Inverted microscope with a Hamamatsu EMCCD C9100-13 Monochrome Camera, and a Zeiss LSM 710 confocal laser-scanning microscope with a Plan-Apochromat 20x/0.8 objective (Carl Zeiss Microimaging, Thornwood, NY). For confocal images, optical sections were collected at 1 μm spacing and shown as a maximum intensity projection using Zen 2009 software (Carl Zeiss). For the Zeiss Axio Observer, Zen 2012 blue software was used.

4.5.5 Inductively Coupled Plasma Mass Spectroscopy (ICP-MS) for Uptake and Exocytosis

To quantify the total uptake of the SPION-CpG by the microglia N9 cells we performed ICP-MS (4500 Series, Hewlett Packard) measurements. The cells were grown as described above and treated with various concentrations of SPION-CpG (0, 0.01, 0.1, 0.3 and 0.5 mg mL^{-1}) or Ferumoxytol (1.5 mg mL^{-1}). After 12 h of exposure, the medium was aspirated, the cells were washed once with PBS and were collected by treating with 0.2% trypsin-EDTA, followed by washing two times with PBS and table-top centrifugation (1000 rpm, 5 min), acid digested overnight using 1 mL of 6770% BDH Aristar Plus Nitric Acid, and analyzed using ICP-MS upon appropriate dilution. A standard curve

was made using serial dilution of a 1 ppm solution of Iron standard solution (Spex CertiPrep). Iron concentration was determined by ICPMS Analysis on a HP 4500 Series using a concentric nebulizer, Scott type spray chamber, and a fixed quartz injector torch. A CX interface was used. Plasma power was 1500 Watt. Helium was used as the collision gas (4 mL min^{-1}). Data was analyzed quantitatively in a spreadsheet program.

To evaluate exocytosis, N9 cells were plated at 6000 cells per well in a 96 well plate (18,000 cells cm^{-2}) and allowed to adhere for 24 h. The cells were then loaded at a 0.1 mg mL^{-1} concentration of SPION-CpG for 2 h. After loading, the cells were washed twice with PBS and 150 μL fresh media was added to each well. At t = 0 h, 8 h, and 24 h, media in the well was completely removed (supernatant fraction) and both the amount of iron in both the supernatant and cell fractions was quantified via ICP-MS. Each group was in triplicate and two independent experiments were performed.

ICP-MS for the exocytosis experiment was performed as follows: 200 μL BDH Aristar Plus Nitric Acid (70%) was added to each sample tube (for the supernatant fraction) or well of a 96 well plate (cell fraction) to dissolve the iron. Each tube or well was washed once with 200 μL of 70% Nitric acid, the sample was then diluted to 3.4 mL with 3 mL of 2% nitric acid solution. Iron concentration was determined by ICPMS Analysis on Agilent 7500 Series using a concentric nebulizer, Scott type spray chamber, and a fixed quartz injector torch. A CX interface was used. Plasma power was 1500 Watt. Helium was used as the collision gas (4 mL min^{-1}). A standard curve was made using serial dilution of a 1 ppm solution of Iron standard solution (Spex CertiPrep). Data was analyzed quantitatively in a spreadsheet program.

4.5.6 Dark-field microscopy imaging

Cells were grown to 80% confluence on a glass bottom cell culture dish for 2448 h. The cells were loaded with 0.5 mg mL^{-1} SPION-CpG for 2 h. After loading, excess media was removed, and the cells were washed extensively with PBS. The cover slips were carefully detached from the bottom of the dishes using a sharp edge forcep and allowed to dry. A drop of non-drying immersion oil (Cargille Laboratories, Cedar Glove, NJ) was put on the cover slip and the cover slip was mounted onto the glass slide and was adhered using nail polish to prevent drying. Dark-field microscopy imaging was performed using a CytoViva dark field microscope system equipped with CytoViva Hyperspectral Imaging System 1.2.

4.5.7 Electron microscopy (SEM and TEM)

TEM imaging was performed on a FEI Tecnai 12 TEM equipped with a Gatan Ultrascan 2 K CCD camera at an accelerating voltage of 120 kV. Cells treated with SPION-CpG conjugates (0.5 mg mL^{-1}) as described earlier, were collected by treating with 0.2% trypsin-EDTA, followed by

washing with PBS and table top centrifugation (2000 rpm, 5 min), fixed with 2% glutaraldehyde in 0.1 M Cacodylate buffer ($Na(CH_3)_2AsO_23H_2O$), pH 7.2, at 4 °C overnight. The following day the cells were washed three times with 0.1 M Cacodylate buffer, post-fixed with 1% OsO_4 in 0.1 M Cacodylate buffer for 30 min and washed three times with 0.1 M Cacodylate buffer. The samples were then dehydrated using 60%, 70%, 80%, and 95% ethanol and 100% absolute ethanol (twice), propylene oxide (twice), and were left in propylene oxideEponate (1:1) overnight at room temperature under sealed environment. The following day the vials were left open until the propylene oxide was evaporated (23 h). The samples were infiltrated with 100% Eponate and polymerized at 64°C for 48 h. Ultra-thin sections (70 nm thick) were cut using a Leica Ultra cut UCT ultra-microtome equipped with a diamond knife, and the sections were picked up on 200 mesh copper EM grids. The grids were stained with 2% uranyl acetate for 10 min followed by Reynold's lead citrate staining for a min prior to imaging.

SEM images of the magnetically-moved cells were obtained on an FEI Quanta 200 scanning electron microscope. Immediately after LIVE/DEAD staining, cells were fixed with 2% glutaraldehyde in 0.1 M Cacodylate buffer ($Na(CH_3)_2AsO_23H_2O$), pH 7.2, at 4 °C. The coverslip was then removed from the glassbottom dish using Coverslip Removal Fluid (MatTek) following the manufacturer's protocol. The coverslip was then washed three times with 0.1 M Cacodylate buffer, pH 7.2, post-fixed with 1% OsO_4 in 0.1 M Cacodylate buffer for 30 min and washed three times with 0.1 M Cacodylate buffer. The samples were then dehydrated through 60%, 70%, 80%, and 95% ethanol, 100% absolute ethanol (twice). The samples were dried in a critical-point dryer and then coated with gold and palladium (Au : Pd 60/40 ratio) in a Cressington 308R coating system.

4.5.8 Magnetic-field Induced Qualitative Cell movement *in vitro* by Bright-field Microscopy

For the magnetically induced cell movement experiments, microglia N9 cells were cultured as described above. Cells were seeded at 9.3 x 10^5 cells per dish (9.7 x 10^4 cells cm^{-2}), grown to 90% confluence and treated with various concentrations (low: 0.1 mg mL^{-1}, medium: 0.3 mg mL^{-1}, and high: 0.5 mg mL^{-1}) of SPION-CpG conjugates. After 2 h of incubation, the loading medium was aspirated, and the cells were washed extensively with PBS (carefully, until most of the free SPION-CpG was gone), supplemented with fresh growth medium, and placed in the incubator with a magnet placed underneath the dish separately. Further to show the controlled movement of cells, three different shapes of magnets were used: square, circular, and rectangular. The movement of cells towards the magnet was assessed at various times (0 h, 2 h, 4 h and 20 h) using microscopy. In order to verify that increased iron concentration at the edge of the magnet was SPION-CpG-loaded cells and not free particles in solution, a cell-free SPION-CpG-only control was included.

These controls were stained for iron using Prussian blue staining as per manufacturer's (Polyscience Inc. Warrington, PA) instructions. Briefly, equal volumes of 4% potassium ferrocyanide and 4% hydrochloric acid were mixed together to prepare the working solution. The standard staining required at least two changes of the working solution treatments for 10 min each, after which the cells were rinsed three times with distilled water and stained using nuclear fast red for 3 min. Finally, the cells were rinsed in running tap water for 1 min and imaged immediately.

4.5.9 Live Cell Imaging

In preparation for live cell imaging, the cell box was assembled and N9 cells plated on it. The box was first sterilized by soaking in 0.6% NaOCl and rinsed thoroughly with autoclaved deionized water in order to remove residual NaOCl (bleach). A large coverslip (48 mm x 65 mm no 1, Ted Pella, catalogue #260365) was autoclaved and attached to the cell box using a non-cytotoxic silicone based adhesive (Silbione Med Adhesive 4100 RTV, Factor II, catalogue #A-4100). The box-coverslip assembly was then left at room temperature in a sterile environment (biosafety hood) for about 2 days in order to allow the adhesive to cure. After 2 days, an autoclaved polydimethylsiloxane (PDMS) dam was placed on the coverslip in order to form a makeshift tissue culture dish. The PDMS dam was created by first synthesizing a 0.5 cm thick rectangular slab of PDMS on a clean glass surface (Sylgard 184 Silicone elastomer kit, Dow Corning, follow manufacturer's protocol) and then cutting an 9 cm^2 rectangular hole in the PDMS. When this PDMS dam is set on the box-coverslip assembly, it forms a water-tight seal with the coverslip. Once the dam is in place, N9 cells (8.72 x 10^5 cells or 9.7 x 10^4 cells cm^{-2}) were plated on the coverslip and allowed to adhere for 8 h in the incubator. The cells were then loaded at 0.1 mg mL^{-1} SPION-CpG for 2 h, following the protocol for the previous cell movement experiment. After loading, the cells were washed with PBS, the PDMS dam was removed and the box-coverslip assembly was inverted into a 100 mm petri dish containing enough media to submerge the coverslip (1020 mL).

Live cell imaging was performed on a Zeiss Axio Observer Z1 Inverted microscope with the Pecon/Zeiss Incubation System. Images were obtained using a 10x/0.3 NA EC-Plan Neofluar objective and a Hamamatsu EMCCD C9100-13 Monochrome Camera. The microscope and camera were controlled using the Zen 2012 Blue Edition software. After connecting the cell box to the microscope, pre-magnet images were taken for reference. A ceramic magnet was then placed on top of the coverslip portion of the cell box above the region of the coverslip where cells are adhered. To prevent the magnet from moving during the experiment, the magnet was secured to the coverslip with tape. Using time-lapse imaging (1 bright-field image every 30 s), the motion of cells within one field of view near the magnet was tracked over 20 h (the same time scale used for the other movement experiment).

Bibliography

[1] Jonathan Witonsky. Ivd market moving rapidly on an upward trajectory. 2012.

[2] Genmark. Innovative esensor technology, 2015.

[3] Therese A. Dolecek, Jennifer M. Propp, Nancy E. Stroup, and Carol Kruchko. Cbtrus statistical report: Primary brain and central nervous system tumors diagnosed in the United States in 2005-2009. *Neuro-Oncology*, 14(suppl 5):v1–v49, 2012.

[4] Howard Hughes Medical Institute. Cells of the immune system, 2015.

[5] Kelin Kuhn, Chris Kenyon, Avner Kornfeld, Mark Liu, Atul Maheshwari, Wei-kai Shih, Sam Sivakumar, Greg Taylor, Peter VanDerVoorn, and Keith Zawadzki. Managing process variation in intel's 45nm cmos technology. *Intel Technology Journal*, 12(2), 2008.

[6] Steven R. Gill, Mihai Pop, Robert T. DeBoy, Paul B. Eckburg, Peter J. Turnbaugh, Buck S. Samuel, Jeffrey I. Gordon, David A. Relman, Claire M. Fraser-Liggett, and Karen E. Nelson. Metagenomic analysis of the human distal gut microbiome. *Science*, 312(5778):1355–1359, 2006.

[7] Peter J Turnbaugh, Ruth E Ley, Michael A Mahowald, Vincent Magrini, Elaine R Mardis, and Jeffrey I Gordon. An obesity-associated gut microbiome with increased capacity for energy harvest. *Nature*, 444(7122):1027–131, 2006.

[8] Andrew L Kau, Philip P Ahern, Nicholas W Griffin, Andrew L Goodman, and Jeffrey I Gordon. Human nutrition, the gut microbiome and the immune system. *Nature*, 474(7351):327–336, 2011.

[9] Pauline D Scanlan, Fergus Shanahan, Yvonne Clune, John K Collins, Gerald C O'Sullivan, Micheal O'Riordan, Elaine Holmes, Yulan Wang, and Julian R Marchesi. Culture-independent analysis of the gut microbiota in colorectal cancer and polyposis. *Environmental microbiology*, 10(3):789–798, 2008.

[10] F Peter Guengerich. Cytochrome p450 and chemical toxicology. *Chemical research in toxicology*, 21(1):70–83, 2007.

[11] Sarah C Sim. Cyp2c9 allele nomenclature, 2015.

[12] Fumihiko Takeuchi, Ralph McGinnis, Stephane Bourgeois, Chris Barnes, Niclas Eriksson, Nicole Soranzo, Pamela Whittaker, Venkatesh Ranganath, Vasudev Kumanduri, William McLaren, et al. A genome-wide association study confirms vkorc1, cyp2c9, and cyp4f2 as principal genetic determinants of warfarin dose. *PLoS genetics*, 5(3):e1000433, 2009.

[13] Nanosphere. Verigene instrumentation, 2015.

[14] World Health Organization. *Screening donated blood for transfusion-transmissible infections: recommendations*. World Health Organization, 2010.

[15] World Health Organization. Testing of donated blood, 2015.

[16] James H. Nichols. Point of care testing. *Clinics in Laboratory Medicine*, 27(4):893 – 908, 2007. Laboratory Management.

[17] A.J. Tudos, G.A.J. Besselink, and R.B.M. Schasfoort. Trends in miniaturized total analysis systems for point-of-care testing in clinical chemistry. *Lab Chip*, 1(2):83–95, 2001.

[18] Carol A. Holland and Frederick L. Kiechle. Point-of-care molecular diagnostic systems: past, present and future. *Current Opinion in Microbiology*, 8(5):504–509, 2005.

[19] Frederick L. Kiechle and Carol A. Holland. Point-of-care testing and molecular diagnostics: Miniaturization required. *Clinics in Laboratory Medicine*, 29(3):555–560, 2009.

[20] Haley D Hill and Chad A Mirkin. The bio-barcode assay for the detection of protein and nucleic acid targets using dtt-induced ligand exchange. *NATURE PROTOCOLS-ELECTRONIC EDITION-*, 1(1):324, 2006.

[21] Cepheid Inc. Genexpert xvi, 2015.

[22] Angelika Niemz, Tanya M. Ferguson, and David S. Boyle. Point-of-care nucleic acid testing for infectious diseases. *Trends in biotechnology*, 29(5):240–250, 2011.

[23] WHO. *Global Tuberculosis Report 2014*. World Health Organization, 2014.

[24] Hua Wang, Yan Chen, A. Hassibi, A. Scherer, and A. Hajimiri. A frequency-shift CMOS magnetic biosensor array with single-bead sensitivity and no external magnet. In *Solid-State Circuits Conference - Digest of Technical Papers, 2009. ISSCC 2009. IEEE International*, pages 438–439,439a, 2009.

[25] H. Wang, S. Kosai, C. Sideris, and A. Hajimiri. An ultrasensitive cmos magnetic biosensor array with correlated double counting noise suppression. In *Microwave Symposium Digest (MTT), 2010 IEEE MTT-S International*, pages 1–1, 2010.

[26] Hua Wang, C. Sideris, and A. Hajimiri. A frequency-shift based cmos magnetic biosensor with spatially uniform sensor transducer gain. In *Custom Integrated Circuits Conference (CICC), 2010 IEEE*, pages 1–4, 2010.

[27] McKinsey L Goodenberger and Robert B Jenkins. Genetics of adult glioma. *Cancer genetics*, 205(12):613–621, 2012.

[28] German G Gomez and Carol A Kruse. Mechanisms of malignant glioma immune resistance and sources of immunosuppression. *Gene therapy & molecular biology*, 10(A):133, 2006.

[29] Dongchang Zhao, Darya Alizadeh, Leying Zhang, Wei Liu, Omar Farrukh, Edwin Manuel, Don J Diamond, and Behnam Badie. Carbon nanotubes enhance cpg uptake and potentiate antiglioma immunity. *Clinical Cancer Research*, 17(4):771–782, 2011.

[30] Leslie L Muldoon, Carole Soussain, Kristoph Jahnke, Conrad Johanson, Tali Siegal, Quentin R Smith, Walter A Hall, Kullervo Hynynen, Peter D Senter, David M Peereboom, et al. Chemotherapy delivery issues in central nervous system malignancy: a reality check. *Journal of clinical oncology*, 25(16):2295–2305, 2007.

[31] Steven A Rosenberg, James C Yang, and Nicholas P Restifo. Cancer immunotherapy: moving beyond current vaccines. *Nature medicine*, 10(9):909–915, 2004.

[32] Eicke Latz, Annett Schoenemeyer, Alberto Visintin, Katherine A Fitzgerald, Brian G Monks, Cathrine F Knetter, Egil Lien, Nadra J Nilsen, Terje Espevik, and Douglas T Golenbock. Tlr9 signals after translocating from the er to cpg dna in the lysosome. *Nature immunology*, 5(2):190–198, 2004.

[33] Behnam Badie and Jacob M Berlin. The future of cpg immunotherapy in cancer. *Immunotherapy*, 5(1):1, 2013.

[34] Darya Alizadeh, Leying Zhang, Thomas Schluep, Behnam Badie, et al. Tumor-associated macrophages are predominant carriers of cyclodextrin-based nanoparticles into gliomas. *Nanomedicine: Nanotechnology, Biology and Medicine*, 6(2):382–390, 2010.

[35] Yoshinori Suzuki, Daiko Wakita, Kenji Chamoto, Yoshinori Narita, Takemasa Tsuji, Tsuguhide Takeshima, Hiroshi Gyobu, You Kawarada, Satoshi Kondo, Shizuo Akira, et al. Liposome-encapsulated cpg oligodeoxynucleotides as a potent adjuvant for inducing type 1 innate immunity. *Cancer research*, 64(23):8754–8760, 2004.

[36] Sakulrat Rattanakiat, Makiya Nishikawa, and Yoshinobu Takakura. Self-assembling cpg dna nanoparticles for efficient antigen delivery and immunostimulation. *European Journal of Pharmaceutical Sciences*, 47(2):352–358, 2012.

[37] Stacey L Demento, Nathalie Bonafé, Weiguo Cui, Susan M Kaech, Michael J Caplan, Erol Fikrig, Michel Ledizet, and Tarek M Fahmy. Tlr9-targeted biodegradable nanoparticles as immunization vectors protect against west nile encephalitis. *The Journal of Immunology*, 185(5):2989–2997, 2010.

[38] Min Wei, Nan Chen, Jiang Li, Min Yin, Le Liang, Yao He, Haiyun Song, Chunhai Fan, and Qing Huang. Polyvalent immunostimulatory nanoagents with self-assembled cpg oligonucleotide-conjugated gold nanoparticles. *Angewandte Chemie International Edition*, 51(5):1202–1206, 2012.

[39] Stuart C McBain, Humphrey HP Yiu, and Jon Dobson. Magnetic nanoparticles for gene and drug delivery. *International journal of nanomedicine*, 3(2):169, 2008.

[40] Benjamin Shapiro. Towards dynamic control of magnetic fields to focus magnetic carriers to targets deep inside the body. *Journal of magnetism and magnetic materials*, 321(10):1594–1599, 2009.

[41] Alek Nacev, Skye H Kim, Jaime Rodriguez-Canales, Michael A Tangrea, Benjamin Shapiro, and Michael R Emmert-Buck. A dynamic magnetic shift method to increase nanoparticle concentration in cancer metastases: a feasibility study using simulations on autopsy specimens. *International journal of nanomedicine*, 6:2907, 2011.

[42] Beata Chertok, Bradford A Moffat, Allan E David, Faquan Yu, Christian Bergemann, Brian D Ross, and Victor C Yang. Iron oxide nanoparticles as a drug delivery vehicle for mri monitored magnetic targeting of brain tumors. *Biomaterials*, 29(4):487–496, 2008.

[43] Sorin V Pislaru, Adriana Harbuzariu, Rajiv Gulati, Tyra Witt, Nicole P Sandhu, Robert D Simari, and Gurpreet S Sandhu. Magnetically targeted endothelial cell localization in stented vessels. *Journal of the American College of Cardiology*, 48(9):1839–1845, 2006.

[44] Boris Polyak, Ilia Fishbein, Michael Chorny, Ivan Alferiev, Darryl Williams, Ben Yellen, Gary Friedman, and Robert J Levy. High field gradient targeting of magnetic nanoparticle-loaded endothelial cells to the surfaces of steel stents. *Proceedings of the National Academy of Sciences*, 105(2):698–703, 2008.

[45] Panagiotis G Kyrtatos, Pauliina Lehtolainen, Manfred Junemann-Ramirez, Ana Garcia-Prieto, Anthony N Price, John F Martin, David G Gadian, Quentin A Pankhurst, and Mark F Lythgoe. Magnetic tagging increases delivery of circulating progenitors in vascular injury. *JACC: Cardiovascular Interventions*, 2(8):794–802, 2009.

[46] Ali S Arbab, Elaine K Jordan, Lindsey B Wilson, Gene T Yocum, Bobbi K Lewis, and Joseph A Frank. In vivo trafficking and targeted delivery of magnetically labeled stem cells. *Human gene therapy*, 15(4):351–360, 2004.

[47] V Vanecek, V Zablotskii, S Forostyak, J Ruricka, V Herynek, M Babic, P Jendelova, S Kubinova, A Dejneka, and E Sykova. Highly efficient magnetic targeting of mesenchymal stem cells in spinal cord injury. *International journal of nanomedicine*, 7:3719, 2012.

[48] Anat Yanai, Urs O Häfeli, Andrew L Metcalfe, Peter Soema, Lois Addo, Cheryl Y Gregory-Evans, Kelvin Po, Xianghong Shan, Orson L Moritz, and Kevin Gregory-Evans. Focused magnetic stem cell targeting to the retina using superparamagnetic iron oxide nanoparticles. *Cell transplantation*, 21(6):1137–1148, 2012.

[49] Eue-Soon Jang, June-Ho Shin, Gang Ren, Mi-Jin Park, Kai Cheng, Xiaoyuan Chen, Joseph C Wu, John B Sunwoo, and Zhen Cheng. The manipulation of natural killer cells to target tumor sites using magnetic nanoparticles. *Biomaterials*, 33(22):5584–5592, 2012.

[50] A. Schweinsberg, S. Hocd, N.N. Lepeshkin, R.W. Boyd, C. Chase, and J.E. Fajardo. An environmental sensor based on an integrated optical whispering gallery mode disk resonator. *Sensors and Actuators B: Chemical*, 123(2):727–732, 2007.

[51] Robert J. Laffin, Daniel W. Chan, Milenko J. Tanasijevic, George A. Fischer, Wayne Markus, Joan Miller, Pat Matarrese, Lori J. Sokoll, Debra J. Bruzek, Julie Eneman, Janice Nelson, Kurtis R. Bray, Jay Huang, and Kathleen G. Loveland. Hybritech total and free prostate-specific antigen assays developed for the beckman coulter access automated chemiluminescent immunoassay system: A multicenter evaluation of analytical performance. *Clinical Chemistry*, 47(1):129–132, 2001.

[52] J.M. Ruano-Lopez, M. Agirregabiria, G. Olabarria, D. Verdoy, D.D. Bang, M. Bu, A. Wolff, A. Voigt, J.A. Dziuban, and R. Walczak. The smartbiophone: a point of care vision under development through two European projects: Optolabcard and labonfoil. *Lab on a Chip*, 9(11):1495–1499, 2009.

[53] T. Gregory Drummond, Michael G. Hill, and Jacqueline K. Barton. Electrochemical DNA sensors. *Nat Biotech*, 21(10):1192–1199, 2003.

[54] Joseph Wang. Carbon-nanotube based electrochemical biosensors: A review. *Electroanalysis*, 17(1):7–14, 2005.

[55] Xiliang Luo, Aoife Morrin, Anthony J Killard, and Malcolm R Smyth. Application of nanoparticles in electrochemical sensors and biosensors. *Electroanalysis*, 18(4):319–326, 2006.

[56] Long Yin Zhou, Xi Yuan Zhang, Gang Lin Wang, Xiao Xia Jiao, Hong Qun Luo, and Nianbing Li. A simple and label-free electrochemical biosensor for DNA detection based on the super-sandwich assay. *Analyst*, 2012.

[57] Dongdong Zhang, Yage Peng, Honglan Qi, Qiang Gao, and Chengxiao Zhang. Label-free electrochemical DNA biosensor array for simultaneous detection of the hiv-1 and hiv-2 oligonucleotides incorporating different hairpin-DNA probes and redox indicator. *Biosensors and Bioelectronics*, 25(5):1088–1094, 2010.

[58] X. Yu, B. Munge, V. Patel, G. Jensen, A. Bhirde, J.D. Gong, S.N. Kim, J. Gillespie, J.S. Gutkind, and F. Papadimitrakopoulos. Carbon nanotube amplification strategies for highly sensitive immunodetection of cancer biomarkers. *Journal of the American Chemical Society*, 128(34):11199–11205, 2006.

[59] D. Hoegger, P. Morier, C. Vollet, D. Heini, F. Reymond, and J.S. Rossier. Disposable microfluidic elisa for the rapid determination of folic acid content in food products. *Analytical and bioanalytical chemistry*, 387(1):267–275, 2007.

[60] P. Kassanos, R.K. Iles, R.H. Bayford, and A. Demosthenous. Towards the development of an electrochemical biosensor for hcgbeta detection. *Physiological measurement*, 29(6):S241, 2008.

[61] J. L. Arlett, E. B. Myers, and M. L. Roukes. Comparative advantages of mechanical biosensors. *Nat Nano*, 6(4):203–215, 2011.

[62] Xu Liang, Yu Heng, Han Shu-Jen, S. Osterfeld, R. L. White, N. Pourmand, and S. X. Wang. Giant magnetoresistive sensors for DNA microarray. *Magnetics, IEEE Transactions on*, 44(11):3989–3991, 2008.

[63] E. Rapoport, D. Montana, and G. S. D. Beach. Integrated capture, transport, and magneto-mechanical resonant sensing of superparamagnetic microbeads using magnetic domain walls. *Lab on a Chip*, 2012.

[64] R.S. Gaster, D.A. Hall, and S.X. Wang. nanolab: An ultraportable, handheld diagnostic laboratory for global health. *Lab on a Chip*, 11(5):950–956, 2011.

[65] D. M. Bruls, T. H. Evers, J. A. H. Kahlman, P. J. W. van Lankvelt, M. Ovsyanko, E. G. M. Pelssers, J. J. H. B. Schleipen, F. K. de Theije, C. A. Verschuren, T. van der Wijk, J. B. A. van Zon, W. U. Dittmer, A. H. J. Immink, J. H. Nieuwenhuis, and M. W. J. Prins. Rapid integrated biosensor for multiplexed immunoassays based on actuated magnetic nanoparticles. *Lab on a Chip*, 9(24):3504–3510, 2009.

[66] Jos Germano, Veronica Martins, Filipe Cardoso, Teresa Almeida, Leonel Sousa, Paulo Freitas, and Moiss Piedade. A portable and autonomous magnetic detection platform for biosensing. *Sensors*, 9(6):4119–4137, 2009.

[67] A. Deggerdal and F. Larsen. Rapid isolation of PCr-ready DNA from blood, bone marrow and cultured cells, based on paramagnetic beads. *BioTechniques*, 22(3):554–7, 1997.

[68] R. Derks, A. Dietzel, R. Wimberger-Friedl, and M. Prins. Magnetic bead manipulation in a sub-microliter fluid volume applicable for biosensing. *Microfluidics and Nanofluidics*, 3(2):141–149, 2007.

[69] Martin A. M. Gijs. Magnetic bead handling on-chip: new opportunities for analytical applications. *Microfluidics and Nanofluidics*, 1(1):22–40, 2004.

[70] Alex Pai, Aroutin Khachaturian, Stephen Chapman, Alexander Hu, Hua Wang, and Ali Hajimiri. A handheld magnetic sensing platform for antigen and nucleic acid detection. *Analyst*, 139(6):1403–1411, 2014.

[71] Peigen Cao, Ke Xu, Joseph O. Varghese, and James R. Heath. The microscopic structure of adsorbed water on hydrophobic surfaces under ambient conditions. *Nano Letters*, 2011.

[72] M.J. Hessner, L. Meyer, J. Tackes, S. Muheisen, and X. Wang. Immobilized probe and glass surface chemistry as variables in microarray fabrication. *BMC genomics*, 5(1):53, 2004.

[73] A.W. Peterson, R.J. Heaton, and R.M. Georgiadis. The effect of surface probe density on DNA hybridization. *Nucleic acids research*, 29(24):5163–5168, 2001.

[74] E.P. Ivanova, D.K. Pham, N. Brack, P. Pigram, and D.V. Nicolau. Poly (l-lysine)-mediated immobilisation of oligonucleotides on carboxy-rich polymer surfaces. *Biosensors and Bioelectronics*, 19(11):1363–1370, 2004.

[75] M.B. Eisen and P.O. Brown. Dna arrays for analysis of gene expression. *Methods in enzymology*, pages 179–204, 1999.

[76] D.R. Call and P. Darrell. Research report fabrication of dna microarrays using unmodified oligonucleotide probes. *BioTechniques*, 30(2):368–379, 2001.

[77] S.K. Chiu, M. Hsu, W.C. Ku, C.Y. Tu, Y.T. Tseng, W.K. Lau, R.Y. Yan, J.T. Ma, and C.M. Tzeng. Synergistic effects of epoxy-and amine-silanes on microarray DNA immobilization and hybridization. *Biochemical Journal*, 374(Pt 3):625, 2003.

[78] AB Steel, RL Levicky, TM Herne, and MJ Tarlov. Immobilization of nucleic acids at solid surfaces: effect of oligonucleotide length on layer assembly. *Biophysical Journal*, 79(2):975–981, 2000.

[79] R. Gonzalez, S. Varnum, and R. Zangar. Sandwich elisa microarrays. generating reliable and reproducible assays for high-throughput screens. *Biomarker methods in drug discovery and development*, pages 273–90, 2008.

[80] Arrayit. Light pin cleaning protocol, 2012.

[81] Invitrogen. Genecatcher: Magnetic beads, 2012.

[82] Affymetrix. Affymetrix, 2009.

[83] Joseph N Zadeh, Conrad D Steenberg, Justin S Bois, Brian R Wolfe, Marshall B Pierce, Asif R Khan, Robert M Dirks, and Niles A Pierce. Nupack: analysis and design of nucleic acid systems. *Journal of computational chemistry*, 32(1):170–173, 2011.

[84] Alex H Pai, Stephen A Chapman, and Seyed Ali Hajimiri. Low cost, portable sensor for molecular assays, November 17 2011. US Patent App. 13/299,087.

[85] Darya Alizadeh, Leying Zhang, Jungyeon Hwang, Thomas Schluep, and Behnam Badie. Tumor-associated macrophages are predominant carriers of cyclodextrin-based nanoparticles into gliomas. *Nanomedicine: Nanotechnology, Biology and Medicine*, 6(2):382–390, 2010.

[86] Steven B Smith, Laura Finzi, and Carlos Bustamante. Direct mechanical measurements of the elasticity of single DNA molecules by using magnetic beads. *Science*, 258(5085):1122–1126, 1992.

[87] Robert S. Molday and Donald Mackenzie. Immunospecific ferromagnetic iron-dextran reagents for the labeling and magnetic separation of cells. *Journal of Immunological Methods*, 52(3):353–367, 1982.

[88] Akira Ito, Yohei Takizawa, Hiroyuki Honda, Ken-ichiro Hata, Hideaki Kagami, Minoru Ueda, and Takeshi Kobayashi. Tissue engineering using magnetite nanoparticles and magnetic force: heterotypic layers of cocultured hepatocytes and endothelial cells. *Tissue engineering*, 10(5-6):833–840, 2004.

[89] Masayori Suwa and Hitoshi Watarai. Magnetoanalysis of micro/nanoparticles: A review. *Analytica Chimica Acta*, 690(2):137–147, 2011.

[90] IEEE Magnetics. Magnetic units, 2015.

[91] Kristian Smistrup, Ole Hansen, Henrik Bruus, and Mikkel F Hansen. Magnetic separation in microfluidic systems using microfabricated electromagnetsexperiments and simulations. *Journal of Magnetism and Magnetic Materials*, 293(1):597–604, 2005.

[92] A Engel and R Friedrichs. On the electromagnetic force on a polarizable body. *American Journal of Physics*, 70(4):428–432, 2002.

[93] Eric Dickinson, George Stainsby, et al. *Colloids in food.* Applied Science Publishers, 1982.

[94] Mark D. Tarn. *Continuous Flow Processes on Single Magnetic and Diamagnetic Particles in Microfluidic Devices.* PhD thesis, University of Hull, april 2011.

[95] Rafael Tadmor, Ernesto Hernandez-Zapata, Nianhuan Chen, Philip Pincus, and Jacob N Israelachvili. Debye length and double-layer forces in polyelectrolyte solutions. *Macromolecules*, 35(6):2380–2388, 2002.

[96] Cedric Taylor and P Hood. A numerical solution of the navier-stokes equations using the finite element technique. *Computers & Fluids*, 1(1):73–100, 1973.

[97] Ethan E White, Alex Pai, Yiming Weng, Anil K Suresh, Desiree Van Haute, Torkom Pailevanian, Darya Alizadeh, Ali Hajimiri, Behnam Badie, and Jacob M Berlin. Functionalized iron oxide nanoparticles for controlling the movement of immune cells. *Nanoscale*, 7(17):7780–7789, 2015.

[98] Sophie Laurent, Delphine Forge, Marc Port, Alain Roch, Caroline Robic, Luce Vander Elst, and Robert N Muller. Magnetic iron oxide nanoparticles: synthesis, stabilization, vectorization, physicochemical characterizations, and biological applications. *Chemical reviews*, 108(6):2064–2110, 2008.

[99] Yudhisthira Sahoo, Hillel Pizem, Tcipi Fried, Dina Golodnitsky, Larisa Burstein, Chaim N Sukenik, and Gil Markovich. Alkyl phosphonate/phosphate coating on magnetite nanoparticles: a comparison with fatty acids. *Langmuir*, 17(25):7907–7911, 2001.

[100] Tobias Haas, Jochen Metzger, Frank Schmitz, Antje Heit, Thomas Müller, Eicke Latz, and Hermann Wagner. The dna sugar backbone 2 deoxyribose determines toll-like receptor 9 activation. *Immunity*, 28(3):315–323, 2008.

[101] Castaneda Rosalinda T, Khurana Aman, Khan Ramsha, Daldrup-Link Heike E, et al. Labeling stem cells with ferumoxytol, an fda-approved iron oxide nanoparticle. *Journal of Visualized Experiments*, (57), 2011.

[102] Nathaniel L Rosi, David A Giljohann, C Shad Thaxton, Abigail KR Lytton-Jean, Min Su Han, and Chad A Mirkin. Oligonucleotide-modified gold nanoparticles for intracellular gene regulation. *Science*, 312(5776):1027–1030, 2006.

[103] Pinal C Patel, David A Giljohann, Weston L Daniel, Dan Zheng, Andrew E Prigodich, and Chad A Mirkin. Scavenger receptors mediate cellular uptake of polyvalent oligonucleotide-functionalized gold nanoparticles. *Bioconjugate chemistry*, 21(12):2250–2256, 2010.

[104] Tyson L Hedrick. Software techniques for two-and three-dimensional kinematic measurements of biological and biomimetic systems. *Bioinspiration & biomimetics*, 3(3):034001, 2008.

[105] Ira Mellman, George Coukos, and Glenn Dranoff. Cancer immunotherapy comes of age. *Nature*, 480(7378):480–489, 2011.

[106] Yuxia Meng, Michèle Kujas, Yannick Marie, Sophie Paris, Joëlle Thillet, Jean-Yves Delattre, and Antoine F Carpentier. Expression of tlr9 within human glioblastoma. *Journal of neuro-oncology*, 88(1):19–25, 2008.

[107] S Farzana Hussain, David Yang, Dima Suki, Elizabeth Grimm, and Amy B Heimberger. Innate immune functions of microglia isolated from human glioma patients. *Journal of Translational Medicine*, 4(1):15, 2006.

[108] S Farzana Hussain, David Yang, Dima Suki, Kenneth Aldape, Elizabeth Grimm, and Amy B Heimberger. The role of human glioma-infiltrating microglia/macrophages in mediating anti-tumor immune responses. *Neuro-oncology*, 8(3):261–279, 2006.

[109] Malika Bsibsi, Rivka Ravid, Djordje Gveric, and Johannes M van Noort. Broad expression of toll-like receptors in the human central nervous system. *Journal of Neuropathology & Experimental Neurology*, 61(11):1013–1021, 2002.

[110] Gordon E Moore et al. Cramming more components onto integrated circuits, 1965. *Electronics Magazine*, page 4, 1965.

[111] Steven M Bowers, Kaushik Sengupta, Kaushik Dasgupta, and Ali Hajimiri. A fully-integrated self-healing power amplifier. In *Radio Frequency Integrated Circuits Symposium (RFIC), 2012 IEEE*, pages 221–224. IEEE, 2012.

[112] Kaushik Dasgupta, Kaushik Sengupta, Alex Pai, and Ali Hajimiri. A 19.1 dbm segmented power-mixer based multi-gbps mm-wave transmitter in 32nm soi cmos. In *Radio Frequency Integrated Circuits Symposium, 2014 IEEE*, pages 343–346. IEEE, 2014.

[113] Kaushik Dasgupta, Kaushik Sengupta, Alex Pai, and Ali Hajimiri. A mm-wave segmented power mixer. *Microwave Theory and Techniques, IEEE Transactions on*, 63(4):1118–1129, 2015.

[114] Debopriyo Chowdhury, Patrick Reynaert, and Ali M Niknejad. Design considerations for 60 ghz transformer-coupled cmos power amplifiers. *Solid-State Circuits, IEEE Journal of*, 44(10):2733–2744, 2009.

[115] Debopriyo Chowdhury, Christopher D Hull, Ofir B Degani, Pankaj Goyal, Yanjie Wang, and Ali M Niknejad. A single-chip highly linear 2.4 ghz 30dbm power amplifier in 90nm cmos. In *Solid-State Circuits Conference-Digest of Technical Papers, 2009. ISSCC 2009. IEEE International*, pages 378–379. IEEE, 2009.

[116] Jongchan Kang, Ali Hajimiri, and Bumman Kim. Isscc 2006/session 11/rf building blocks and plls/11.9. 2006.

[117] Andreea Balteanu, Ioannis Sarkas, Eric Dacquay, Alexander Tomkins, Gabriel M Rebeiz, Peter M Asbeck, and Sorin P Voinigescu. A 2-bit, 24 dbm, millimeter-wave soi cmos power-dac cell for watt-level high-efficiency, fully digital m-ary qam transmitters. *Solid-State Circuits, IEEE Journal of*, 48(5):1126–1137, 2013.

[118] Anandaroop Chakrabarti and Harish Krishnaswamy. High-power high-efficiency class-e-like stacked mmwave pas in soi and bulk cmos: Theory and implementation. 2014.

[119] Ichiro Aoki, Scott D Kee, David B Rutledge, and Ali Hajimiri. Distributed active transformer-a new power-combining and impedance-transformation technique. *Microwave Theory and Techniques, IEEE Transactions on*, 50(1):316–331, 2002.

[120] Ullrich R Pfeiffer and David Goren. A 23-dbm 60-ghz distributed active transformer in a silicon process technology. *Microwave Theory and Techniques, IEEE Transactions on*, 55(5):857–865, 2007.

[121] Jiashu Chen, Lu Ye, Diane Titz, Fred Gianesello, Romain Pilard, Andreia Cathelin, Fabien Ferrero, Cyril Luxey, and Ali M Niknejad. A digitally modulated mm-wave cartesian beamforming transmitter with quadrature spatial combining. In *Solid-State Circuits Conference Digest of Technical Papers (ISSCC), 2013 IEEE International*, pages 232–233. IEEE, 2013.

[122] Dixian Zhao and Patrick Reynaert. 14.1 a 0.9 v 20.9 dbm 22.3%-pae e-band power amplifier with broadband parallel-series power combiner in 40nm cmos. In *Solid-State Circuits Conference Digest of Technical Papers (ISSCC), 2014 IEEE International*, pages 248–249. IEEE, 2014.

[123] Shouhei Kousai and Ali Hajimiri. An octave-range, watt-level, fully-integrated cmos switching power mixer array for linearization and back-off-efficiency improvement. *Solid-State Circuits, IEEE Journal of*, 44(12):3376–3392, 2009.

[124] Arrayit. Superaldehyde and superaldehyde 2, 2015.